DISCLAIMER

This report was prepared as an account of work sponsored by an agency of the United States Government. Neither the United States Government nor any agency thereof, nor any of their employees, makes any warranty, express or implied, or assumes any legal liability or responsibility for the accuracy, completeness, or usefulness of any information, apparatus, product, or process disclosed, or represents that its use would not infringe privately owned rights. Reference herein to any specific commercial product, process, or service by trade name, trademark, manufacturer, or otherwise does not necessarily constitute or imply its endorsement, recommendation, or favoring by the United States Government or any agency thereof. The views and opinions of authors expressed herein do not necessarily state or reflect those of the United States Government or any agency thereof. Reference herein to any social initiative (including but not limited to Diversity, Equity, and Inclusion (DEI); Community Benefits Plans (CBP); Justice 40; etc.) is made by the Author independent of any current requirement by the United States Government and does not constitute or imply endorsement, recommendation, or support by the United States Government or any agency thereof.

LA-UR-25-29410

Title: Detonation Waves in High Explosives

Author(s): Menikoff, Ralph
Kober, Edward Martin

Intended for: Distribution to colleagues at LANL, LLNL, SNL and DoD laboratories. Will consider general publication (book, review chapters) if approved for general release to public.
Report

Issued: 2025-09-19

Los Alamos
NATIONAL LABORATORY

Detonation Waves in High Explosives

Ralph Menikoff
Los Alamos National Laboratory, retired

Edward M. Kober, editor
Los Alamos National Laboratory

July 2, 2025

Preface

It has been known since the 1960s that detonation phenomena in solid explosives can be qualitatively different from that in gaseous explosives. In particular, for solid explosives, initiation due to shear or frictional heating [Bowden and Yuffee, 1952] and shock initiation [Campbell et al., 1961b,a] occurs for much weaker stimuli than expected based on the chemical reaction rate at the bulk solid temperature. This is due to heterogeneities in the solid which when compressed leads to hotspots or localized regions of high temperature. It is the basis of the ignition and growth concept for hotspot burning [Lee and Tarver, 1980].

Reactive burn rates of solid explosives can be viewed as a homogenization or sub-grid model that accounts for the effect of heterogeneities that are not practical to resolve. Moreover, the statistic of the heterogeneities and the dynamics of hotspots occur on scales too small to measure with currently available diagnostic techniques. Consequently, empirical burn rates are used for modeling detonation phenomena in solid explosives.

Empirical models must be calibrated. The intend of this book is to describe experiments that characterize detonation phenomena and provide data that can be used to calibrate burn rates. Clearly, the accuracy of a model is no better than the uncertainty in the data. In addition to measurement inaccuracies some of the uncertainties with the experimental data are due to sample to sample variations in the explosive heterogeneities. The effect of the heterogeneities are expected to be largest near an ignition threshold.

The author would like to thank colleagues who have contributed to his understanding of detonation waves. In particular, Tommy Sewell, Tariq Aslam, Ed Kober, Dana Dattelbaum, Rick Gustavsen, Larry Hill and Christina Scovel.

Los Alamos, NM, *Ralph Menikoff*
July, 2025

It was a pleasure and an education to review this manuscript, and I appreciate Ralph's patience in addressing my questions. The careful reader should find a solid framework from which to develop further inquiries and analysis.

Ed Kober

Contents

I Introduction 2

II Mathematical Description 18

III Detonation Phenomena and Experiments 70

List of Symbols & Acronyms

e	specific internal energy
P	pressure
T	temperature
S	specific entropy
V	specific volume
u	particle velocity
D	detonation speed
Q	specific energy source term
G	Gibbs free energy $= e + P\,V - T\,S$
H	enthalpy $= e + P\,V$
H_f	heat of formation

c	sound speed
C_V	specific heat at constant volume
C_P	specific heat at constant pressure
ρ	density, $1/V$
λ	reaction progress variable
$\mathcal{R}$	reaction rate
γ	adiabatic index $= c^2/(P\,V)$
Γ	Grüneisen coefficient $= V(\partial_e P)_{V,\lambda}$
σ	thermicity $= (\partial_\lambda P)_{V,e}/(\rho\,c^2)$
	or speed of a shock wave
m	mass flux for shock wave

κ	detonation front curvature
$D_n(\kappa)$	normal detonation speed (curvature effect)

HE	high explosive
PBX	plastic-bonded explosive
EOS	equation of state
TMD	theoretical maximum density
CJ	Chapman-Jouguet
VN	von Neumann
DSD	detonation shock dynamics
SDT	shock-to-detonation transition
PDV	photonic Doppler velocimeter
VISAR	velocity interferometry system for any reflector
ODE	ordinary differential equation
PDE	partial differential equation
MD	molecular dynamics

Part I

Introduction

CHAPTER 1

Overview

A material at high temperature can react or decompose. For an energetic material, the reaction is exothermic and releases chemical energy that would further increase the temperature. Under some circumstances, when a reaction is triggered, such a reaction can propagate and the material rapidly releases a large amount of energy giving rise to an explosion. Examples of such materials are aerosols, suspensions of solid particles or liquid droplets in a gas; such as coal dust, grain dust and fuel-air explosions.

Frequently, explosions are due to accidents. A spectacularly destructive example is the recent explosion of a large quantity of ammonium nitrate (thousands of tons) in Beirut, Lebanon (August 2020); see for example Beirut explosion. Ammonium nitrate is used as a fertilizer. It and the aerosols are not considered to be explosives due to the limited conditions for which an explosion can occur.

An aerosol gets the oxidizer from the surrounding air. Burning requires diffusion of the oxidizer to the particle surface where the reaction occurs. A large density of small particles is required for a fast enough reaction to support an explosion.

In contrast, an explosive is an energetic material with both fuel and oxidizer mixed on a molecular scale (either premixed gases or within molecules of a solid). This allows fast enough reactions over a wide range of conditions to support a self-propagating reactive wave known as a detonation wave.

A detonation wave can be controlled and an explosive used for useful purposes such as in mining, construction, demolition, explosive welding, argon flash lamp, pulsed power using a magnetic flux generator [see also Goforth et al., 2015], jet cutter with shaped charge, explosive art, and generating conditions to study the response of materials at high strain rates and high pressures [see for example, Marsh, 1980]. Explosives are also used in conventional munitions and nuclear weapons.

The focus of this book is on the theory and phenomenology of solid high explosives (HEs); in particular, plastic-bonded explosives (PBXs). Some aspects of detonation wave theory are needed to interpret explosive data. Hence, the theory is presented before the detonation wave phenomenology. A familiarity with fluid flow, specifically the notion of shock waves and the shock loci are assumed. In the remainder of this chapter we give a brief overview on the basic properties of detonation waves and PBXs.

1.1 What is a detonation wave

For simplicity we assume an explosive can be modeled with a one step exothermic reaction:

Explosive: Reactants → Products

Furthermore, the reactants are meta-stable and hence the reaction is irreversible.

A propagating detonation wave results from 3 steps:

1. A lead shock in the reactants raises its temperature and triggers the reaction.
2. The reaction releases chemical energy further increasing the temperature and the pressure by generating several product molecules for each HE molecule.
3. The energy release and pressure increase from that reaction then continues to drive the lead shock.

Once initiated, a detonation wave is self-sustaining; *i.e.*, does not require support from behind. Since the reaction is irreversible, it runs until completion when the reactants are all burned.

The region behind the lead shock to the end of the reaction is called the reaction zone. The reaction zone is a region of partially burned explosive; *i.e.*, a mixed region of reactants and products. Ahead of the reaction zone are all reactants and behind it are all products. However, slow reactions near the end of the reaction zone may not contribute to driving a detonation wave. This will be discussed later.

The utility of a detonation wave in an HE is that a large amount of energy can be released on a short time scale. Moreover, the energy release scales with the size of the HE charge. In addition, the detonation pressure and sound speed are large and can be used to drive a flyer plate at high velocity. Rough values for an HE are an initial density of about $2\,\mathrm{g/cm^3}$, energy release upwards of 4 to 5 MJ/kg, and time scale on the order of $10\,\mu$s. For comparison, the kinetic energy of a car with a mass of 2 ton moving at 100 mph is 1.8 MJ. This is equivalent to the energy released by a 6 cm (2.4 in) cube of HE weighing about 0.5 kg (1.1 lb). The detonation pressure can be as high as 35 GPa, with a local sound speed of 6.5 km/s (14,500 mph). This can drive a metal flyer plate at a velocity up to a few km/s.

Most HE molecules are composed mainly of carbon, hydrogen, nitrogen and oxygen atoms. We note that a sugar molecule also is composed of these same atoms, and when burned in air releases a large amount of energy; sucrose $C_{12}H_{22}O_{11} + 12\,O_2 \rightarrow 12\,CO_2 + 11\,H_2O$ plus 3.94 kcal/g = 16.5 MJ/kg. Though the specific energy density can be larger than an HE, sugar is not an explosive because a significant amount of the energy release utilizes the oxidizer (O_2) from the air, and the reaction rate (surface burn rather than volume burn) is too low. However, sugar dust, even with a much smaller energy per volume (due to the low density of air and the N_2 in the air diluting the specific energy release), can have a sufficiently large burn rate for small particles (due to large surface area of the dust particles) to sustain a violent explosion; see sugar dust explosion.

1.1.1 Detonation wave vs Shock wave

In a later chapter, the form of the reaction zone for a steady detonation wave is derived. It is qualitatively as shown in figure 1.1. The labeled points are the initial quiescent state (0), the von Neumann (VN) "spike" or VN state, and the Chapman-Jouguet (CJ) state. The reaction zone is the region between the VN and CJ points. For most HE, the reaction zone is fairly narrow; less than 0.1 mm. In some respects, a detonation can be treated as a shock to the CJ state with no VN spike and zero reaction zone thickness. Both shock waves and detonation waves are compressive waves and their wave speeds are supersonic with respect to the material ahead of the flow.

For a planar detonation wave, the possible states behind the detonation front are analogous to the shock locus. They are determined by the shock jump relations, the initial reactants state ahead of the wave, and the equation of state of the products behind the wave. In contrast

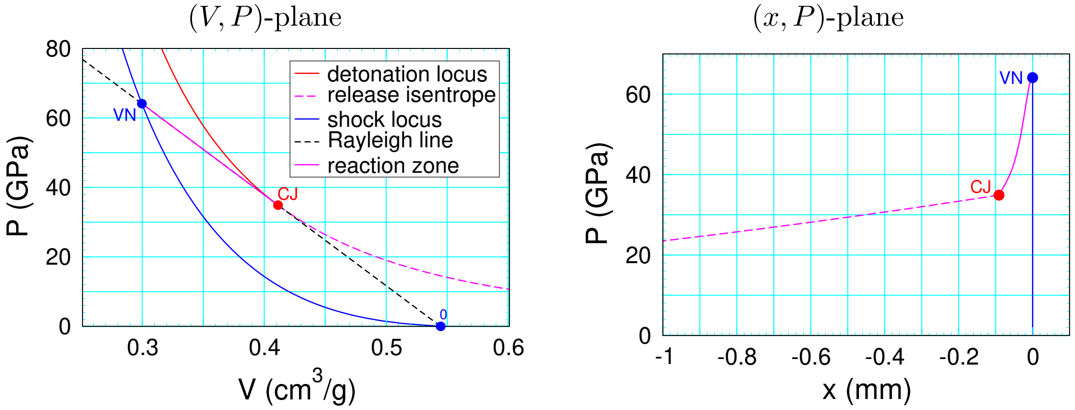

Figure 1.1: Detonation wave reaction-zone is from the von Neumann spike (VN) state to the Chapman-Jouguet (CJ) state in the (x,P)-plane and the (V,P)-plane.

to the shock locus, the detonation products locus (red line) lies above the initial reactants locus (blue curve) in the (V, P)–plane. Consequently, there is a point on detonation locus that is tangent to a line in the (V, P)–plane that originates at the initial state of the reactants material (0). This is a Rayleigh line, whose slope defines the velocity of that reactive wave. The point of tangency with the products locus can be shown to have the minimum detonation speed (see § 3.1 and figure 3.1), and to be sonic with respect to the flow behind the front. It corresponds to the self-supporting or underdriven detonation wave. The underdriven wave is often referred to as a CJ detonation, and the point of tangency is the CJ state. In contrast to a shock wave, a CJ detonation is not affected by acoustic waves behind the front. This Rayleigh line will intersect the reactants locus a second time, and that defines the VN state. This is a short-lived high-pressure state, with a pressure greater than that of the CJ state (P_{CJ}).

Points on the detonation locus with a higher pressure than P_{cj} arise from overdriven detonation waves. They are more like shock waves in that the flow behind the front is subsonic. If not supported, these waves decay; an overdriven detonation wave will decay into the underdriven detonation propagating with the minimum detonation speed, similar to a shock wave decaying into an acoustic wave propagating with the sound speed.

The reaction-zone width gives rise to affects for detonation waves that do not occur for discontinuous shock waves. These are discussed, in later chapters on the curvature effect and the failure diameter. Briefly, the shock jump relations need to be modified for a detonation wave with a curved front. One effect of the reaction zone thickness is that an underdriven diverging detonation has a smaller wave speed than the minimum detonation speed for a planar detonation wave. A second effect is that there is a minimum diameter for an unsupported detonation wave to propagate in a cylindrical charge. This is known as the failure diameter. A third effect is that there can be an unburned region (called a dead zone) left behind when a detonation wave turns a corner.

1.1.2 Detonation wave vs Deflagration wave

In general, an energetic material can support both a fast mode and a slow mode of burning. The fast mode gives rise to detonation waves and the slow mode to deflagration waves. An energetic material can be used as either an explosive (fast mode) or a propellant (slow burn).

The two types of waves have significantly different properties:

1. A detonation wave is pressure increasing and compressive, while a deflagration wave is pressure decreasing and expansive.
2. The reaction of a detonation wave is triggered by shock heating. In contrast, the reaction of a deflagration wave requires heat conduction.

3. a) Both the detonation and deflagration loci, see figure 1.2, have unique sonic points which are referred to as CJ points. The CJ point divides the loci into weak and strong branches. The weak branches are the one closer to the initial state; *i.e.*, $P_0 < P < P_{CJ}$ for weak detonation branch and $P_0 > P > P_{CJ}$ for weak deflagration branch.

   b) Ahead of the front, all points on the detonation locus are supersonic while all points on the deflagration locus are subsonic.

   c) For the detonation locus, the flow behind the strong branch $(P > P_{cj})$ is subsonic and behind the weak branch $(P_{cj} > P > P_0)$ is supersonic. For the deflagration locus, the flow behind the weak branch $(P_0 > P > P_{cj})$ is subsonic and behind the strong branch $(P_{cj} > P > 0)$ is supersonic.

   d) Points on the weak branch of the detonation locus and strong branch of the deflagration locus are unphysical (entropy decreasing) and do not correspond to detonation/deflagration waves.

   e) For the detonation locus, all points on the strong branch have a reaction-zone profile and are physically obtainable; see for example [Menikoff, 2022a]. In contrast, for the deflagration locus, a wave profile exists for only one point on the weak branch; see for example [Menikoff, 2012]. Consequently, for a given ahead state, there is a unique deflagration wave that depends on the coefficient of heat conduction.

4. Due to the different heating mechanism, the wave speeds can be orders of magnitude different. For HEs, the minimum detonation speed is typically a few km/s, while the deflagration speed is typically in the range of mm/s to a few cm/s. In addition the wave widths are also orders of magnitude different; typically ∼ 100 μm for a detonation wave compared to ∼ 0.1 μm for a deflagration wave.

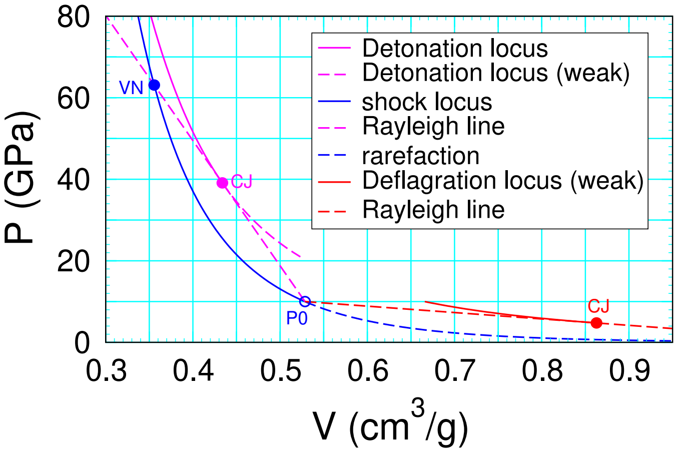

Figure 1.2: Detonation and deflagration loci in (V, P)-plane.

We note that for the ignition and growth concept of detonation waves, the reaction in the growth phase is assumed to be due to deflagration waves propagating outward from burn centers triggered by hotspots. This is discussed later in more detail.

1.2 HE molecules

Most HE molecules form small grains or crystallites. If the melting temperature is below the critical reaction temperature, such as TNT, the solid can be melted and cast into an explosive charge. For molecules that form an amorphous solid, explosive grains can be pressed into an explosive charge. As discussed in the next subsection, for other HEs, the crystallites need to be held together by a binder; such as the HMX based PBX 9501 and the TATB based PBX 9502.

Common HE molecules are listed in [Cooper, 1996, chpt 3] and [Akhavan, 2004, chpt 2 & 5]. Three illustrative examples are shown in figure 1.3: TNT is a well known explosive to which other HEs are compared, HMX is used in the high performance conventional HE (*e.g.*, PBX 9501), and TATB is used in the high performance insensitive HE (*e.g.*, PBX 9502).

Performance refers to having a high CJ pressure and detonation speed. A detonation wave in a conventional HE (CHE) has a very narrow reaction zone. It can be approximated as a discontinuity to the CJ state with front curvature having a small effect on wave propagation. An insensitive HE (IHE) requires a stronger detonator (higher pressure for longer duration) to

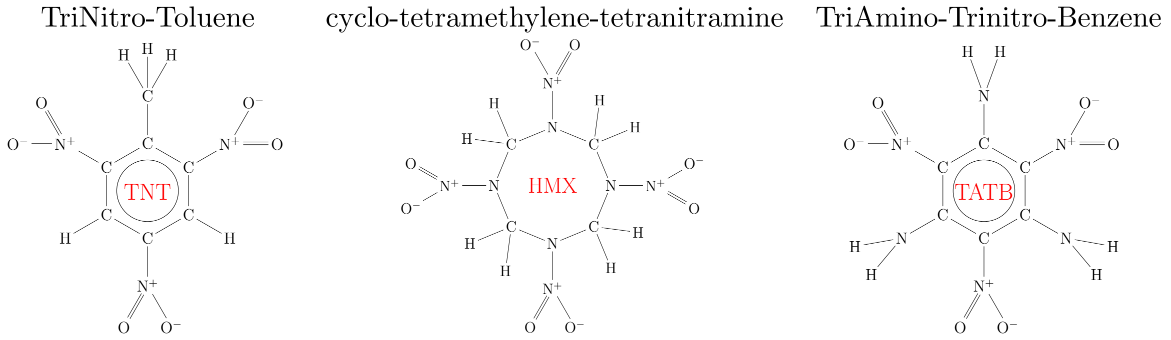
TriNitro-Toluene cyclo-tetramethylene-tetranitramine TriAmino-Trinitro-Benzene

$$
\begin{aligned}
\text{TNT:}\quad & C_7H_5N_3O_6 \rightarrow 2.5\,H_2O + 1.5\,N_2 + 3.5\,CO + 3.5\,C \\
\text{HMX:}\quad & C_4H_8N_8O_8 \rightarrow 4\,H_2O + 4\,N_2 + 4\,CO \\
\text{TATB:}\quad & C_6H_6N_6O_6 \rightarrow 3\,H_2O + 3\,N_2 + 3\,CO + 3\,C
\end{aligned}
$$

Figure 1.3: Examples of explosive molecules and their reactions viewed as a single step.

initiate a detonation wave than a CHE. This is advantageous for safety, especially in accident scenarios.

HE molecules tend to be large with 20 to 30 atoms, and the reaction products are composed of several species of smaller molecules, as seen from in the simple reactions illustrated in figure 1.3. The exception is the production of solid carbon or soot. Nevertheless, the reaction generates many product molecules from one molecule of the HE. This, along with the chemical energy released, results in a large detonation pressure.

The products species for the reactions listed in figure 1.3 give a reasonable estimate for the heat of detonation based on the formula (Hess' law)

$$\Delta H_{det} = \sum_{species} H_f(product\ species) - H_f(reactants) \tag{1.1}$$

where H is the enthalpy (e+P V) and H_f is the heat of formation at temperature and pressure of 25 C and 1 bar. By convention ΔH_{det} is negative for an exothermic reaction; *i.e.*, the energy released by the reaction is $Q = -\Delta H_{det} > 0$.

Due to the many possible reactions among the products molecules, the equilibrium composition of the products from minimizing the Gibbs free energy ($G = e + PV - TS$) varies with its density and temperature; *i.e.*, there is a trade-off between maximizing the entropy and minimizing the internal energy of the products. Thermochemical codes compute the species concentrations in order to determine the products equation of state needed for simulations. In general, the composition of products species in the neighborhood of the CJ state (high pressure and high temperature) are different then those for low pressure and low density of the expanded state, which are needed to determine the heat of detonation.

The detonation pressure and wave speed for the illustrative explosives is given in table 1.1. Also listed is the initial density. Largely due to the solid density, the detonation pressure of high explosives are orders of magnitude larger than those of premixed gaseous explosives, which are only as high as a few tens of MPa.

Table 1.1: Pressure and detonation speed for selected explosives at initial density ρ_0 and ambient pressure and temperature [Gibbs and Popolato, 1980], and heat of detonation calculated from heats of formation of assumed products species. [Akhavan, 2004, table 5.12].

	TNT	HMX based PBX 9501	TATB based PBX 9502	
ρ_0	1.64	1.84	1.89	g/cc
P_{cj}	19.	35.	28.	GPa
D_{cj}	6.9	8.8	7.8	km/s
$-\Delta H_{det}$	4.2	5.0	3.5	MJ/kg

Several important properties of HE molecules can be inferred from the illustrated reactions in figure 1.3:

1. An HE molecule contains both fuel and oxidizer. This is the analog of premixed combustion rather than laminar combustion; *i.e.*, reactions are local and do not require diffusion for fuel and oxidizer to come together. As a result the reaction rate of an HE can be very large; up to several $100/\mu$s. Consequently, the reaction zone of a detonation wave can be very narrow.
2. The component products molecules are much smaller than the reactants molecules. Hence the reaction results in a large increase (up to a factor of about 10) in the number density of molecules. Both the energy release and the increase of the number density of molecules contribute to the detonation pressure and detonation speed.
3. The oxygen balance of the reaction stoichiometry has an important effect. TNT and TATB are oxygen deficient, leading to an excess of carbon atoms in the products. The carbon atoms then form clusters, which are accounted for in the heat of detonation by a term for the heat of formation of graphite. The formation of clusters results from a diffusion process; see [Shaw and Johnson, 1987]. Hence the energy released by the carbon bonding occurs on a slower time scale than that of the main reaction. As a result, the reaction zone has a long tail with a small amount of energy release. This can affect the propagation speed of a curved detonation wave.
4. Used as propellant the HE molecules would react with the oxygen in air and release more energy. Products would have CO_2 rather than CO or carbon clusters. Consequently, the heat of combustion is larger in magnitude than the heat of detonation. Both the heat of combustion (with excess O_2 present) and the heat of detonation can be measured in calorimetry experiments, depending whether the calorimetry vessel is filled with air or an inert like argon.

The heat release or change in enthalpy has a graphical interpretation in the (V, P)–plane as shown in figure 1.4. It is the area under the CJ release isentrope and to the right of the Rayleigh line. To get the full energy, the products have to expand out to very large V such that the pressure is near zero.

In most applications, the expansion of the products is limited. The cylinder test serves as an illustrative example, which is discussed further in section 9.2.1. It consists of cylinder of HE inside a thin walled copper tube. When the HE is initiated, a detonation wave propagates along the axis and the wall expands outward transferring HE chemical energy to the kinetic energy of the wall. As shown in the velocity plot, the wall is still accelerating outward after $15\,\mu$s. This corresponds to a wall expansion by a factor of 3 in radius, and expansion of the products by $V/V_0 \approx 7$ and a pressure of $P \approx 0.1\,\text{GPa}$. At this point about $80\,\%$ of chemical energy has been transferred to the kinetic energy the wall.

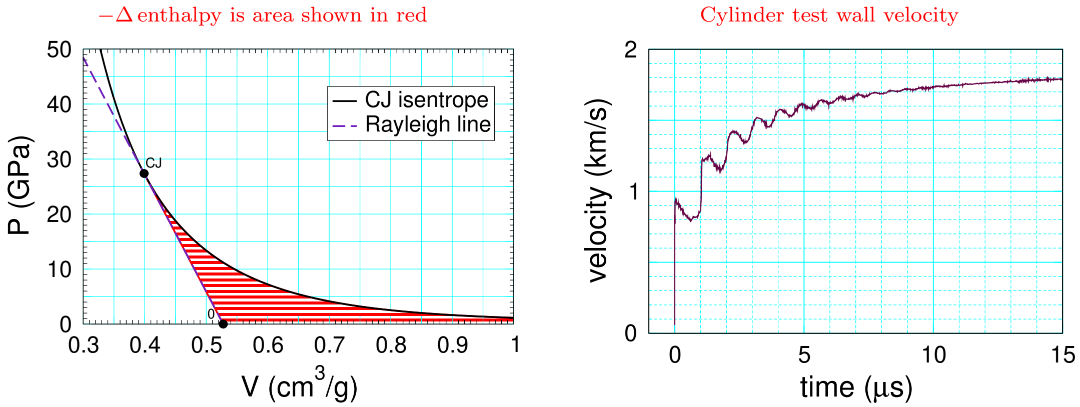

Figure 1.4: Graphical interpretation of chemical energy release (left plot). Cylinder test wall velocity (right plot) illustrates conversion of HE energy to kinetic energy of wall.

1.3 Plastic-bonded explosives

Plastic-bonded explosives (PBXs) are an important class of solid explosives. They are heterogeneous materials consisting of explosive grains or crystallites held together by a polymeric binder. Typically, they have a few percent porosity. The grains have a size distribution ranging from a few tenths of μm to a couple of mm.

After describing how a PBX is made, the heterogeneities are described for the illustrative PBXs in the previous section.

1.3.1 PBX manufacture

The manufacturing process for a PBX is designed to control the spatial variation of the heterogeneities. It consists of the following steps:

1. A batch of molding powder is made by combining a distribution of HE grain sizes. The grains are coated with a binder using a slurry process. This results in prills or conglomerates of grains and binder.
2. Batches are blended into a lot in order to achieve a specified statistical variation for the prills; *i.e.*, mass fraction of HE and size distribution of grains.
3. The molding powder is heated and pressed to reduce the porosity until a billet of the specified density is reached.
4. A billet can then be machined to the desired shape for an experiment or application.

The spatial variations of the heterogeneities within a billet are related to the statistical variations of the molding powder prills. Non-uniformities of the stress in the pressing process can lead to small cm scale variations in the density [Olinger, 2005] and partial alignment of the HE crystallites (analog of texture for cold rolling metal) [Schwarz et al., 2013]. The alignment is important since HE crystals typically have low symmetry and can be very anisotropic. This can affects properties such as the initial density of a PBX due to thermal expansion. In addition, pressing can break the HE crystallites and decrease their average size.

Typically, samples of a PBX for a series of experiments are taken from the same lot. This reduces the scatter in the data from variations in heterogeneities among samples.

1.3.2 Meso-scale structure

The composition of the PBX example HEs from the previous section are PBX 9501, composed of 95 wt percent HMX plus a binder of 2.5 wt percent estane and 2.5 wt percent elasto-plasticizer with about 1.7 percent porosity [Gibbs and Popolato, 1980, pp 109–119], and PBX 9502, composed of 95 wt percent TATB plus a binder of 5 wt percent Kel-F with about 2.5 percent porosity [Gibbs and Popolato, 1980, pp 120–129]. The high performance of these PBXs is due to the performance of the HE grains (HMX and TATB), the low mass fraction of the binder and the small porosity. In general, the binder and porosity dilute the energy per volume and lowers the performance of the PBX relative to its HE component.

The structure of the heterogeneities (HE grains, binder and pores) can be seen in the X-ray micro-computer tomography (micro–CT) images shown in figure 1.5 of slices through samples of PBX 9501 and PBX 9502. A feature of tomography is that slices in the interior can be viewed without destroying the sample. Examples of this are sequences of image slices that can be downloaded and viewed from the supplement to the article cited in the figure; files `PBX9501-8_xyslicethrough.gif` and `PBX9502-3_xyslicethrough.gif`.

As seen in the images, small grains, rather than binder, fill in most of the space between the larger grains. The binder is present as a thin layer ($\lesssim 1\mu$m) over the different grains and is often difficult to resolve directly. In general, a distribution of grain sizes is needed for a PBX to have a high HE content. For PBX 9501, the coarse grains are similar in size to table sugar and the fine grains to powdered sugar. The pores are often referred to as voids since any gas (air or vapor from either HE or binder) inside them would have a negligible mass.

The micro–CT images have a pixel size of $0.8\,\mu$m. The resolution is not sufficient to see small pores less than a μm in size. Alternate measurement techniques, ultra-small angle neutron scattering (USANS) and ultra-small angle Xray scattering (USAXS), have been used to determine the size distributions of pores and binder, down to a size of a few nm and $0.1\,\mu$m, respectively. For neutron scattering, the contrast between the HE grains and the binder can

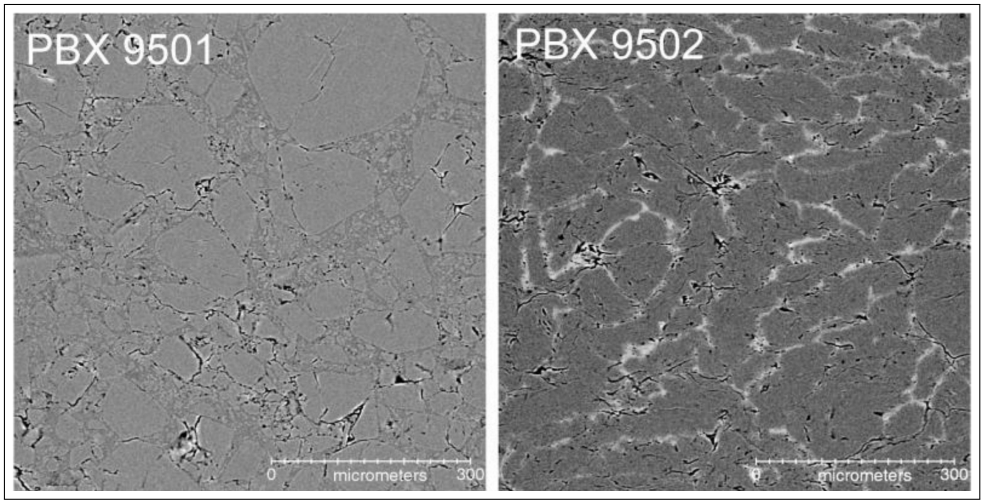

Figure 1.5: Computer X-ray tomography image of a slice through samples of PBX 9501 and 9502 from Yeager et al. [2020, fig 3a,b]. The grey regions are HE grains and the small black regions are pores. For the 9502 image, the white regions are binder. For 9501, the scattering contrast is not sufficient to distinguish binder from from HMX grains.

be enhanced by making the PBX with deuterated binder, *i.e.*, substituting deuterium atoms for hydrogen atoms.

The analysis of the scattering data require assumptions on scattering form factors for the binder and pores and the particle probability density; see [Mang et al., 2010, eqs 2–4]. For PBX experiments, spherical and cylindrical form factors and the sum of log-normal distributions for the particle probability density have been used. Comparing the calculated size distributions from different form factors gives an indication of the uncertainty in the size distribution from the assumption on the shape of the binder and pores.

We note that the shape of the pores down to $0.1\,\mu$m does matter for the 'Ignition and Growth' concept of hotspot burning discussed later. Also of interest is whether small pores are inclusions within a grain or gaps in the binder on the surface of the grains. Computer tomography has been extended to the nano-scale; see for example study of TATB crystal morphology by Patterson et al. [2022]. The trade-off of finer resolution is a smaller field of view. For a small number of HE grains it should be possible to determine the pore shape, the thickness of the binder coating the grains and the location of the pores, provided that the sample is still representative of the bulk material.

For PBX 9501, the size distributions of pores and binder have been determined using USANS. The volume weighted pore distribution for the spherical and cylindrical void model are shown in [Mang et al., 2010, figs 3 and 5] and for the volume weighted binder distributions in [ibid, figs 4 and 6]. (It should be noted that these samples were pressed as thin disks, 1 mm × 9.5 mm, which might introduce anisotropy.) For the spherical model, the volume weighted pore distribution as a function of diameter covers the range from 0.1 to 10 μm. The peak of the volume distribution is at a diameter of 0.7 μm and the mean diameter is 2.2 μm [ibid, table 3]. The peak indicates that there are a large number of sub-micron size pores to compensate for the smaller pore volume, while the disparity with the mean pore size is due to the log-normal distribution being skewed to micron sized pores when the pore diameter is plotted on a linear scale rather than a log scale.

The spherical model for the volume weighted binder distribution covers a narrower range than the pore distribution; from 0.09 to 2 μm. The peak of the volume weighted distribution is at a diameter of 0.3 μm and the mean diameter is 0.6 μm [ibid, table 3]. Very likely the binder coats the grains with a small thickness, and the spherical binder model is crude approximation for the binder shape.

The cylindrical model has 2 parameters for a particle; length and diameter. The analysis of [Mang et al., 2010] finds that for the binder L/D is between 12 and 14, and for the pores L/D is between 5 and 6. Hence, the cylinders correspond to disks. For the volume weighted pore distribution as a function of L, the peak is at $L = 0.25\,\mu$m (corresponding to $D = 1.4\,\mu$m) and the mean is $L = 0.4\,\mu$m and $D = 6\,\mu$m [ibid, table 4]. In contrast to the spherical model, the large cylinder diameter would likely exclude sub-micron pores. For the binder distribution, the peak is at $L = 0.14\,\mu$m (corresponding to $D = 0.8\,\mu$m) and the mean is $L = 0.16\,\mu$m and $D = 0.9\,\mu$m [ibid, table 4]. The small value of L can be attributed to the thickness of the binder coating the grains due to the surface to volume ratio of the grains and the volume fraction of the binder being much less than that of the grains.

Both the spherical and cylindrical models indicate that the binder thickness is on average less than 1 micron. This would imply that, in addition to scattering contrast, part of the difficulty for the micro–CT distinguishing the binder from the HE is due to the limited resolution of the images.

For PBX 9502, the pore size distribution has been measured with USANS. The volume weighted distribution for the spherical model is shown in [Thompson et al., 2010, fig 8]. Compared to PBX 9501, the pore diameter is in a similar range, roughly 0.1 to a few microns. The PBX 9502 distribution function has more structure (oscillation in the range from 0.4 to 1.1 μm). This is likely due to imperfections in the TATB crystallites; see [Patterson et al., 2022]. The cited figure also shows that the integrated pore volume is dominated by pores with a diameter less than 1 micron. In addition the figure shows the distribution for 3 samples whose density varies by about 1 percent, corresponding to porosity change of 28 and 48 percent compared to the standard pressing density with 2.5 percent porosity. There is a significant increase in the first peak (about 0.25 μm) of the size distribution at the lower densities. Experiments have shown that lower initial densities of a PBX increase shock sensitivity. In other words, measurable quantities on the meso-scale (such as porosity) are correlated with detonation properties on the hydro-scale.

1.4 Heterogeneous burn rate

Shock initiation experiments, described in a later chapter, shows that the chemical reaction rate of an HE from the shock temperature is orders of magnitude too small for the observed time to detonation. The needed burn rate can be explained by temperature variations behind the lead shock resulting from the meso-scale structure. In particular, localized regions of high temperature (referred to as hotspots) generated by pore collapse dominate the burn rate. Hence the number density and size distribution of pores are important for the burn rate. This is discussed in chapter 6 on the 'Ignition and Growth' concept of hotspot burning. For now we note that if the initial porosity is small then small changes in the pressing density of a PBX results in much larger changes in the relative porosity than the relative density (*i.e.*, $\Delta\,\text{porosity}/\text{porosity} \gg \Delta\rho/\rho$), and hence can have a substantial effect on the burn rate.

The pore sizes important for the reaction rate range from about $0.1\,\mu$m to $10\,\mu$m. It is not feasible to do reactive-burn simulations that resolve these very small pores. Instead homogenized reactive-burn models are used in which the meso-scale structure of a PBX is replaced by a few (typically, 1 or 2) reaction progress variables (λ_i) and possibly auxiliary state variables to account for past history of the flow, such as the lead shock pressure. Effectively this averages out short-wavelength high-frequency variations in the state variables (density, temperature, pressure and λ_i).

Chemical reaction rates, especially for condensed phase materials, are primarily sensitive to temperature. Due to the tail of the temperature distribution, the volume averaged rate can be much greater than the rate at the volume averaged temperature. Consequently, a homogenized reaction rate can not be based on the chemical rate for the homogenized state variables. Instead, a sub-grid model is needed to account for the underlying physics on the meso-scale not resolved by the homogenized state variables. For a PBX, the sub-grid burn model can be thought of as representing the volume averaged chemical reaction rate, where the volume average is over the length scale of the meso-scale heterogeneities. Since the PBX grain size specification is on the prills, it would be natural to use the compressed prill volume to average the chemical rate. We refer to the average as the burn rate to distinguish it from the chemical reaction rate.

The dynamics of hotspot generation and the subsequent interaction of the hotspots are not well understood. Nor are there experimental techniques to measure simultaneously the short temporal and spatial scales; sub ns and sub μm, respectively. Consequently, an empirical burn rate is used for the sub-grid model. At best an empirical burn rate has a heuristic motivation.

Typically, the functional form for an empirical burn rate is chosen to be a function of pressure. This choice is due to the limited temperature data available at high pressure to calibrate model EOS. Also, the homogenized pressure, and hence the pressure dependent burn rate, is better behaved and evaluated numerically.

In contrast to a chemical reaction rate, which can be measured, the parameters of an empirical burn rate needs to be calibrated on some detonation phenomena data and then validated on other experimental data to determine the range of applicability. Generally, calibration utilizes simple experiments which are easier to analyze than the experiments used to determine the range of applicability.

There are several other notable points for reactive-burn models related to the length scale of the heterogeneities, and to the homogenization.

1. The reaction-zone width of a detonation wave is a physical length scale. It needs to be resolved in order for model simulations in 2- or 3-D to converge under mesh refinement; see for example figure 1.6.

2. For PBX 9501, the reaction-zone width is estimated to be between 50 and 100 μm (based on curvature effect data). As seen in figure 1.5, this is larger than the size of some grains and smaller than others. In this case, the impedance match of the lead shock from the grains to the binder and then back from the binder to the grains, leads to hydrodynamic fluctuations; see [Menikoff, 2020] and references therein. Hence, the reaction zone is not steady. The fluctuations generate acoustic noise in the products behind the detonation front. This can affect the local detonation speed and the local position of the sonic point relative to the end of the reaction zone. We conjecture that these affects can lead to an uncertainties in experimental data for HE phenomena that are not captured by the homogenized reactive burn models. For example, there is a few per cent scatter in Pop plot data from shock-to-detonation transition experiments that are larger than estimates of the measurement uncertainty. Reaction zone fluctuations from heterogeneities are discussed further in sections 3.3 and 4.3.2 .

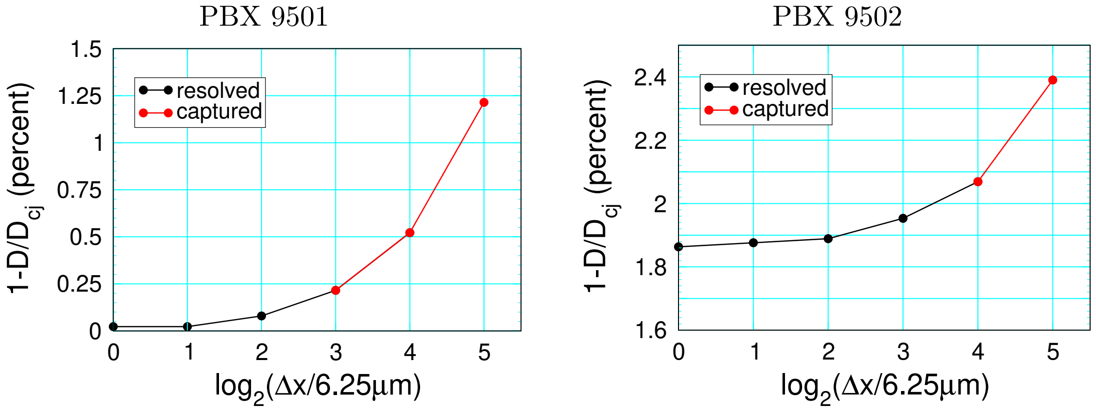

Figure 1.6: Percent change in axial detonation speed with cell size for cylinder test simulations using SURF model [Menikoff, 2019b, figs 5 and 13].

3. Using unconfined rate sticks, the axial detonation wave speed have been measured to a few tenths of a percent based on timing pins along the length of a rate stick 25 to 50 mm apart; see for example [Campbell, 1984]. The accuracy implies that short-wavelength high-frequency fluctuations average out, and that a detonation wave is compatible with a homogenized reactive-burn model. Moreover, it is common to adjust the products equation of state to fit the measured CJ detonation wave speed. This can be viewed as part of the homogenization.

4. A gaseous detonation can exhibit a galloping instability in 1-D and transverse waves along the detonation front leading to cellular wave patterns in 2- and 3-D, see [Fickett and Davis, 1979, §7D]. Experimentally, PBXs have not been observed to exhibit such instabilities. Physically, this may be due to meso-scale heterogeneities overwhelming perturbations that trigger instabilities in a gaseous explosive. However, simulations of a PBX with homogenized burn models also do not exhibit any obvious instability. Since the homogenized burn rates do not explicitly have meso-scale heterogeneities, the instabilities must have a different cause. One possibility is the lower sensitivity of the burn rate to perturbations of the lead shock compared to an Arrhenius reaction rate with a high activation energy often used to model gaseous detonations. This is supported by the observation of detonation instabilities in a MD simulation of a model 2D material with a high activation energy [Heim et al., 2008].

Finally we note that the predictivity of empirical burn models depends on what data is used for the calibration and the accuracy of calibration data. Subsequent chapters will discuss detonation wave phenomena and experiments used to characterize them. The data from the experiments described are among those used to calibrate reactive-burn models.

Part II

Mathematical Description

CHAPTER 2

Reactive flow equations

The natural setting for modeling detonation phenomenon is the reactive flow equations. The conservation form of the 1-dimensional PDEs are

$$\partial_t \begin{pmatrix} \rho \\ \rho u \\ \rho(e + \frac{1}{2}u^2) \\ \rho\lambda \end{pmatrix} + \partial_x \begin{pmatrix} \rho u \\ \rho u^2 + \underline{P} \\ \rho u(e + \frac{1}{2}u^2 + \underline{P}V) \\ \rho u\lambda \end{pmatrix} = \begin{pmatrix} 0 \\ 0 \\ \rho Q\underline{\mathcal{R}} \\ \rho\underline{\mathcal{R}} \end{pmatrix} \tag{2.1}$$

where ρ, u, e and λ are density, particle velocity, specific internal energy and reaction progress variable, respectively. $V = 1/\rho$ is specific volume, $P(V, e, \lambda)$ is the pressure, Q is an energy source term, and $\mathcal{R}(V, e, \lambda)$ is the burn rate. P and $\mathcal{R}$ are material dependent functions and along with Q can be thought of as 'input' parameters.

The first 3 equations are for conservation of mass, momentum and energy, and the fourth is for the reaction progress variable. The hydro flow and the reaction are coupled through the pressure and the burn rate; the red terms in Eq. (2.1).

Typically, λ is taken to be the mass fraction of products. In this case, $\lambda = 0$ and $\lambda = 1$ correspond to the reactants and products, respectively, and $0 < \lambda < 1$ represents partly burned material. For fixed λ, the equation of state (EOS), $P(V, e, \lambda)$ and $T(V, e, \lambda)$, is assumed to be thermodynamically consistent (derivable from a potential, such as the Helmholtz free energy) and thermodynamically stable ($K_S \geq K_T \geq 0$ where K_S and K_T are the isentropic and isothermal bulk moduli, respectively, and $C_P \geq C_V \geq 0$ where C_P and C_V are the specific heat at constant pressure and volume, respectively). In addition, it is assumed that isentropes are convex in the (V, P)–plane, $\partial^2 P/\partial V^2|_S > 0$, where S is the specific entropy. Later, in section 2.2, we show that the energy release of the reaction is a combination of the explicit energy source term Q and an implicit offset of the energy origins for the reactants and the products built into the EOS.

Since source terms, right hand side of Eq. (2.1), do not affect the shock jump relations, the standard fluid flow jump relations for mass, momentum and energy apply to discontinuities in the hydro variables. From the jump relations corresponding to the mass and the reaction progress variable, it can be shown that λ is continuous across a shock wave. As a consequence, the reaction equation reduces to a rate-like equation

$$\boxed{(\mathsf{d}/\mathsf{d}t)\lambda = \mathcal{R}} \tag{2.2}$$

where $(\mathsf{d}/\mathsf{d}t) = \partial_t + u\,\partial_x$ is the convective time derivative along particle paths. Despite the appearance, it is not an ODE since the rate depends on the hydro variables.

In order for the PDEs to describe steady detonation waves, an explosive material must satisfy an additional constraint on its EOS

$$\boxed{(\partial_\lambda P)_{V,e} + \Gamma\rho\,Q > 0} \tag{2.3}$$

where $\Gamma(V,e,\lambda) = V(\partial_e P)_{V,\lambda}$ is the Grüneisen coefficient, and have an irreversible reaction, $\mathcal{R} \geq 0$. This will be shown in a later chapter.

It is noted in section 1.4 that solid explosives are heterogeneous materials and that the burn rate is dominated by hotspots. Several implications follow:

1. Equation (2.1) is for a single reaction. Though it can easily be generalized to multi-step reactions, this is not likely to improve the accuracy of the burn rate since chemical reaction rates are strongly temperature dependent [Tarver et al., 1996] and the hotspot temperature distribution is lost in the homogenization. Multi-step reactions are important for other burn regimes, in particular, thermal ignition in cook off experiments.

2. There are 2 notable cases when multiple reactions are used: carbon clustering and particle burning in metal loaded explosives. These have slow burn rates compared to the hotspot burn rate. In addition, they physically involve diffusion processes that are not well captured by Eq. (2.2).

3. Hotspot burn implies that local regions are either completely burned or completely unburned with λ being the mass average of the burned regions. This is consistent with the reactants being meta-state and the burn rate being irreversible and running to completion.

4. For a single irreversible reaction, the completely burned state will always be the equilibrium products independent of reaction path.

2.1 EOS for partly burned HE

The equations of state of the reactants and products are fit to data and a mixture rule is used to interpolate in λ for partly burned HE. Typically, P-T equilibrium is used for the mixture rule. Thermodynamically, it is defined by the Gibbs free energy

$$G(P,T,\lambda) = \lambda G_p(P,T) + (1-\lambda) G_r(P,T) \tag{2.4}$$

where T and S are the temperature and specific entropy, respectively. The subscripts 'r' and 'p' denote the reactants and products, respectively. To be a valid thermodynamic potential, $G(P,T)$ must be jointly concave in P and T. Since a linear combination of jointly concave functions with positive coefficients is concave, it follows that if G_r and G_p are each thermodynamically consistent and stable potentials then for fixed λ the mixture rule defines a thermodynamic consistent and stable potential.

The specific energy, specific volume and specific entropy are also linear in λ

$$\begin{aligned} e(P,T,\lambda) &= G - P\,V + T\,S = \lambda e_p(P,T) + (1-\lambda) e_r(P,T) && \text{(2.5a)} \\ V(P,T,\lambda) &= \partial_P G \qquad\qquad\quad = \lambda V_p(P,T) + (1-\lambda) V_r(P,T) && \text{(2.5b)} \\ S(P,T,\lambda) &= -\partial_T G \qquad\qquad = \lambda S_p(P,T) + (1-\lambda) S_r(P,T) && \text{(2.5c)} \end{aligned}$$

As functions of V, e and λ, the pressure and temperature are determined by the equations

$$\begin{aligned} P(V,e,\lambda) &= P_p(V_p,e_p) = P_r(V_r,e_r) && \text{(2.6a)} \\ T(V,e,\lambda) &= T_p(V_p,e_p) = T_r(V_r,e_r) && \text{(2.6b)} \\ V &= \lambda V_p + (1-\lambda) V_r && \text{(2.6c)} \\ e &= \lambda e_p + (1-\lambda) e_r && \text{(2.6d)} \end{aligned}$$

We note that there are 4 equations in 4 variables V_r, e_r, V_p and e_p. From the concavity of the mixed Gibbs potential, it follow that a solution to these equations exist and is unique, provided that the reactants EOS and products EOS are both thermodynamically consistent and stable. The P-T mixture rule can be thought of as having the reactants and products phase separated. Physically it is expected that $V_p > V_r$ since the reaction increases the number of moles in the products. This provides a constraint that the P-T mixture rule should respect.

After the solution of Eq. (2.6) is determined, other thermodynamic quantities of the mixture at (V,e) can be obtained from those of the products at (V_p,e_p) and reactants at (V_r,e_r), with $\lambda_p = \lambda$ and $\lambda_r = 1-\lambda$. The mixture isothermal sound speed and specific heat at constant pressure are given by

$$\frac{1}{(\rho\, c_T)^2} = \frac{\lambda_p}{(\rho_p\, c_{T,p})^2} + \frac{\lambda_r}{(\rho_r\, c_{T,r})^2}\ , \tag{2.7a}$$

$$C_P = \lambda_p C_{V,p} + \lambda_r C_{V,r}\ . \tag{2.7b}$$

The specific heat at constant volume and the Grüneisen coefficient can be expressed as

$$C_V = \lambda_p C_{V,p} + \lambda_r C_{V,r} + \frac{w_p w_r}{w_p + w_r}\left[C_{V,p}\tfrac{\Gamma_p}{V_p} + C_{V,r}\tfrac{\Gamma_r}{V_r}\right]^2 T\ , \tag{2.7c}$$

$$\frac{\Gamma}{V} = \frac{w_p C_{V,p}\frac{\Gamma_p}{V_p} + w_r C_{V,r}\frac{\Gamma_r}{V_r}}{(w_p + w_r)C_V}\ , \tag{2.7d}$$

where $w_i = \frac{\lambda_i}{(\rho_i c_{Ti})^2}$. Then the isentropic sound speed is given by the general thermodynamic relation

$$(\rho c)^2 = -(\partial_V P)_e + P(\partial_e P)_V = (\rho\, c_T)^2 + (\Gamma\rho)^2 C_V T\ . \tag{2.7e}$$

Several additional points about the mixture EOS are noteworthy:

1. Solving Eq. (2.6) requires an iterative algorithm and is computationally more expensive than an analytic EOS.

2. Solid EOS are developed for compression. Typically, in expansion at temperature up to several hundred Kelvin, the isothermal bulk modulus goes negative and thermodynamic stability breaks down. This can happen when a detonation wave hits an interface with a low density material, such as air. In this case, P-T equilibrium Eq. (2.6) will fail to have a solution.

3. P-T equilibrium is justified for gaseous explosives since the reactants and products are mixed at a molecular level. For hotspot reaction in a solid EOS, the reactants and products are locally phase separated with the products at a higher temperature than the reactants. Hence, temperature equilibrium is not a good approximation for a solid explosive. However, when the homogenized burn rate is dominated by the pressure, the rate calibration can compensate for the mixture rule. This may affect the range of applicability of the HE model.

4. In principle, a 2-phase EOS model can be used with a temperature for each phase. However, this would require terms in the PDEs to equilibrate the pressure and particle velocity between the phases. There are issues with this class of models. Notably, an additional shock jump condition is needed to partition the energy between the phases; see for example Kapila et al. [2001] and references therein.

5. A mixture model with distinct temperatures for the reactants and products can be obtained by replacing Eq. (2.6b) of the P-T equilibrium model with an empirical relation $V_p = \phi V_r$ where $\phi > 1$ is a model parameter. Stewart et al. [1989] has tested this mixture model by comparing the reaction-zone profile of a detonation wave as ϕ was varied. They found the pressure profiles were relatively insensitive but the temperature profiles were sensitive to ϕ. They also found that ϕ had to be restricted for the mixture equations to have a solution, and for the sound speed to be real. This implies that the

two temperature model would have a limited effect when a pressure dependent burn rate is used.

As discussed in section 1.4, physically the burn rate of a heterogeneous solid explosive depends on hotspots and not the bulk reactants and products temperatures from a mixture rule. As noted above there are issues with all mixture rules. They all depend on an empirical calibration of the burn rate to compensate.

The P-T equilibrium mixture rule is well-behaved provided that the EOSs of the reactants and products are thermodynamically consistent and stable. It has been extensively used for reactive burn models.

When the burn rate is chosen to be a function of only P, the reactive flow PDEs (2.1) do not explicitly depend on temperature. Temperature only enters through the mixture rule. The P-T equilibrium pressure is thus a reasonable variable on which to base an empirical burn rate.

2.1.1 Ideal explosive

It is instructive to then study the ideal explosive EOS as it has simple analytic expressions for the reactants, products and P-T equilibrium of a partly burned explosive. In addition, it provides an example in which the reaction energy is accounted for in an offset of the energy origin q of the products relative to the reactions rather than the source term in the energy PDE of Eq. (2.1); *i.e.*, $Q = 0$. Later we will see there are also analytic expressions for the CJ state and the reactants shock locus.

The ideal explosive EOS has 3 parameters: adiabatic exponent $\gamma > 1$, specific heat $C_V > 0$ and energy release q. The EOSs are listed below:

Reactants (ideal gas EOS)

$$P_r(V, e) = (\gamma - 1)e/V \tag{2.8a}$$

$$T_r(V, e) = e/C_V \tag{2.8b}$$

Products (ideal gas EOS with energy offset q)

$$P_p(V, e) = (\gamma - 1)(e + q)/V \tag{2.9a}$$

$$T_p(V, e) = (e + q)/C_V \tag{2.9b}$$

PT equilibrium EOS

$$V_r = V_p = V \tag{2.10a}$$

$$e_p = e - (1 - \lambda)\, q \tag{2.10b}$$

$$\underline{e_r = e + \lambda\, q \qquad\qquad} \tag{2.10c}$$

$$V = \lambda V_p + (1 - \lambda) V_r \tag{2.10d}$$

$$e = \lambda e_p + (1 - \lambda) e_r \tag{2.10e}$$

Equivalent to ideal explosive EOS

$$P(V,e,\lambda) = (\gamma-1)(e+\lambda q)/V \tag{2.11a}$$
$$T(V,e,\lambda) = (e+\lambda q)/C_V \tag{2.11b}$$

The result is two offset EOS for the reactants and products, and the partially burned material is a linear mixture between them.

2.2 Energy source term

The energy release from the reaction is due to the explicit energy source term Q in the PDEs Eq. (2.1) and an implicit offset of the energy origins for the reactants ($\lambda = 0$) and the products ($\lambda = 1$) built into the EOS. This follows from the transformation

$$Q \to \widetilde{Q} = Q - q \ , \tag{2.12a}$$
$$e \to \widetilde{e} = e - \lambda q \ , \tag{2.12b}$$
$$\begin{aligned} P(V,e,\lambda) \to \widetilde{P}(V,\widetilde{e},\lambda) &= P(V,\widetilde{e}+\lambda q,\lambda) \\ &= P(V,e,\lambda) \ , \end{aligned} \tag{2.12c}$$
$$\begin{aligned} \mathcal{R}(V,e,\lambda) \to \widetilde{\mathcal{R}}(V,\widetilde{e},\lambda) &= \mathcal{R}(V,\widetilde{e}+\lambda q,\lambda) \\ &= \mathcal{R}(V,e,\lambda) \ . \end{aligned} \tag{2.12d}$$

The transformation maps solutions to the PDEs with energy source Q and EOS $P(V,e,\lambda)$ into solutions with energy source $\widetilde{Q}$ and EOS $\widetilde{P}(V,e,\lambda)$. Hence, the energy release can be shifted from a source term ($\widetilde{Q}$) to the EOS ($\widetilde{P}$) by varying the parameter q.

As is frequently done, the transformation can be used to eliminate the explicit energy source term; *i.e.*, choosing $q = Q$ yields $\widetilde{Q} = 0$ and the only source terms in the reactive flow PDEs Eq. (2.1) is for the reaction. Since the energy shift λq is 0 for the reactants and q for the products, effectively the energy origin for the products EOS is shifted relative to the energy origin of the products. For the P-T equilibrium mixture rule, this is equivalent to shifting the energy for the products EOS; $P_p(V,e) \to \widetilde{P}_p(V,\widetilde{e}) = P_p(V,\widetilde{e}+q)$.

To summarize, the energy release of the reaction can be accounted for by either an explicit energy Q, or the energy origin of the products, or the energy origin of the reactants. It also can be a combination of the above. A frequently used convention is to choose the initial reactant energy $e_0 = 0$ and adjust the energy origin of the products EOS such that $e_{cj} = \frac{1}{2}P_{cj}\cdot(V_0 - V_{cj})$, where $P_{cj} = P_p(V_{cj}, e_{cj})$ and cj denotes the detonation state. Then the explicit energy source term Q is zero.

2.3 Characteristic equations

The characteristic equations are listed below (see [Menikoff, 2022b] for derivation).

Acoustic wave families

$$(\mathsf{d}/\mathsf{d}t + c\partial_x)P + \rho c\,(\mathsf{d}/\mathsf{d}t + c\partial_x)u = s\,\mathcal{R}, \quad \text{along } \mathsf{d}x/\mathsf{d}t = u + c \tag{2.13a}$$

$$(\mathsf{d}/\mathsf{d}t - c\partial_x)P - \rho c\,(\mathsf{d}/\mathsf{d}t - c\partial_x)u = s\,\mathcal{R}, \quad \mathsf{d}x/\mathsf{d}t = u - c \tag{2.13b}$$

Contact wave families

$$(\mathsf{d}/\mathsf{d}t)e + P(\mathsf{d}/\mathsf{d}t)V = Q\,\mathcal{R} \quad \text{along } \mathsf{d}x/\mathsf{d}t = u \tag{2.13c}$$

$$(\mathsf{d}/\mathsf{d}t)\lambda = \mathcal{R}, \quad \mathsf{d}x/\mathsf{d}t = u \tag{2.13d}$$

where $\mathsf{d}/\mathsf{d}t = \partial_t + u\partial_x$ is the convective time derivative, $c = (\partial_\rho P)^{1/2}_{S,\lambda}$ is the sound speed and

$$s = (\partial_\lambda P)_{V,e} + \Gamma\rho\,Q\ . \tag{2.14}$$

When the burn rate $\mathcal{R} = 0$, these reduce to the standard hydro characteristic equations without source terms.

Using the thermodynamic identity

$$\mathsf{d}\,e(V,S,\lambda) = -P\,\mathsf{d}\,V + T\,\mathsf{d}\,S + (\Delta G)\,\mathsf{d}\lambda\ , \tag{2.15}$$

where $\Delta G = G_p(P,T) - G_r(P,T)$ and G is the Gibbs free energy, an equivalent form of the characteristic Eq. (2.13c) is

$$T\,(\mathsf{d}/\mathsf{d}t)S = (Q - \Delta G)\mathcal{R}\ , \tag{2.16}$$

If $Q - \Delta G > 0$ then for the reaction to be entropy increasing on particle paths, one must also have $\mathcal{R} \geq 0$. Hence, the reaction is irreversible and thermodynamically the reactants can be thought of as meta-stable. In contrast to shock waves for which only the compressive branch of the shock locus is entropy increasing and physically allowed, the entropy increase from the reaction is what allows for expansive entropy increasing deflagration waves. For non-reactive flow ($\mathcal{R} = 0$), Eq. (2.16) reduces to $(\mathsf{d}/\mathsf{d}t)S = 0$, and the flow is isentropic on particle paths, except for shock waves in compression.

Note, s is invariant under the energy shift transformation, Eq. (2.12). When $Q = 0$, s reduces to $(\partial_\lambda P)_{V,e}$. The dimensionless quantity $\sigma = (\partial_\lambda P)_{V,e}/(\rho\,c^2)$ is known as the thermicity. Hence, the source terms in the characteristic equations are positive when the thermicity and reaction rate are positive. This is needed for an explosive to have a detonation wave; see for example [Menikoff, 2022a]. The thermicity can be expressed as (see for example [Fickett and Davis, 1979, §4a4, eq 4.13e] or [Menikoff, 2012, eq C.30])

$$\sigma = (\Delta V)/V - \Gamma(\Delta H)/c^2 \ , \tag{2.17}$$

where $\Delta V = V_p - V_r$ and $\Delta H = H_p(P,T) - H_r(P,T)$ is the heat of reaction. As an example, for an ideal HE, Eq. (2.11), $\Gamma = \gamma - 1$, $\Delta V = 0$, $\Delta H = -q$, and the thermicity is $\sigma = \Gamma q/c^2$.

Typically, for an explosive $\Delta V > 0$ (reaction increases number of moles in the products) and $\Delta H < 0$ (reaction is exothermic), and both terms on the right hand side of Eq. (2.17) are positive. Some materials, such a solid undergoing a polymorphic phase transition or a polymer when it decomposes, can be endothermic with a sufficiently large volume increase for $\sigma > 0$. Consequently, such a material can support a detonation wave, even though it is endothermic.

2.3.1 Shock acceleration

The characteristics for left and right-facing shock waves are shown in figure 2.1. The 3 incoming characteristics ahead of the front determine the ahead state of the shock wave. Then the one incoming characteristic behind the front determines the shock strength; *i.e.*, the point on the shock locus for the behind state. The 3 incoming characteristics ahead and the 1 behind reflect the properties that a shock wave is supersonic with respect to the flow ahead of the front and subsonic with respect to the flow behind the front.

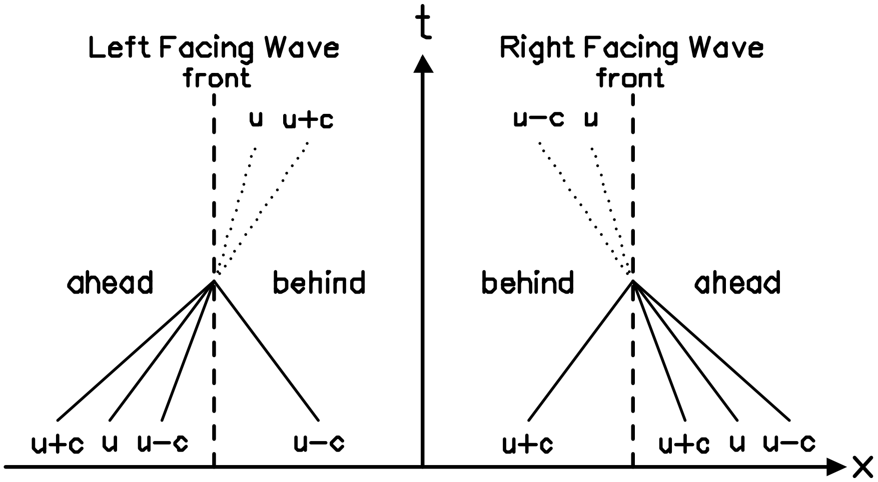

Figure 2.1: Characteristics in rest frame of shock front for left- and right-facing shock waves. Solid and dotted lines are incoming and outgoing characteristics, respectively.

Thus, for a right-facing shock, the shock speed is determined by the $u + c$ characteristic, Eq. (2.13a), behind the front, the ahead state and the shock jump conditions. For an inert, the shock accelerates or deaccelerates depending on whether the pressure increases or decreases behind the shock. This is illustrated by the time sequence of pressure profiles in figure 2.2.

Also shown in the figure are pressure profiles for a shock-to-detonation transition (SDT). For this example, both the pressure gradient and the reaction source term in the behind characteristic contribute to the shock acceleration at early time. For the last profile, the shock has transitioned to a detonation wave. The kink in the profile corresponds to the end of the reaction zone. The steep pressure gradient ahead of the kink is balanced by the reaction source term, and persists as the detonation wave propagates. SDT is discussed further in the chapter on shock initiation.

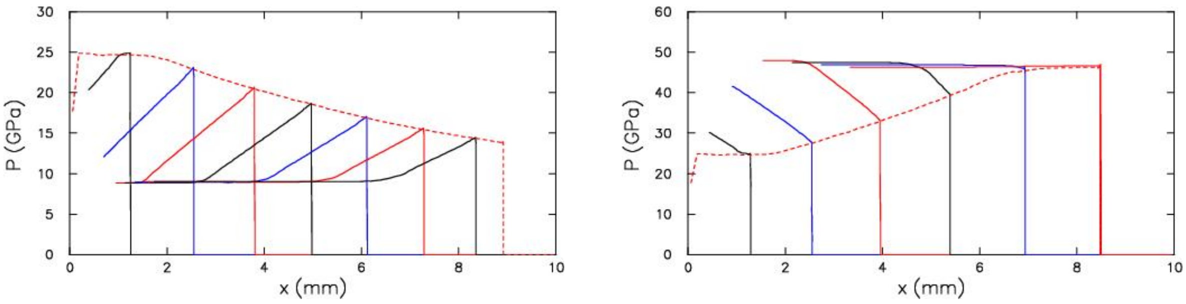
rarefaction wave
shock decays

compressive wave
shock grows

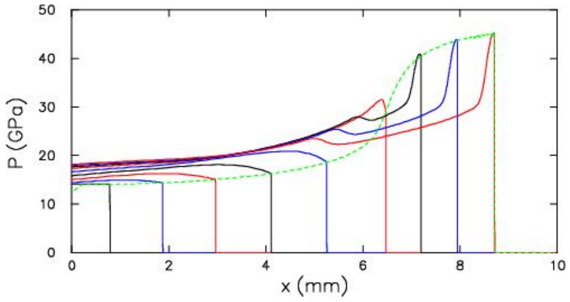
reaction and pressure gradient accelerate shock
shock-to-detonation transition

Figure 2.2: Pressure profiles at sequence of times. For an inert material, top 2 plots, the shock deaccelerates when followed by a rarefaction wave and accelerates when followed by a compressive wave. The dotted lines are shock pressure as function of position. The bottom plot illustrates a shock-to-detonation transition in an explosive. The profiles show that the lead shock pressure builds up and then is leveling off as the shock transits to a detonation.

2.4 Riemann problem

For each characteristic equation, see Eq. (2.13), there is a wave family; shock + rarefaction waves or contact wave. To understand the interactions between these waves, it is helpful to consider the initial value problem with constant left and right states. This is called the Riemann problem; see [Menikoff and Plohr, 1989] and references therein.

A special case of a Riemann problem arises when a shock wave impacts the interface with another material. This gives rise to a transmitted shock in the second material and a reflected wave in the first material. For weak shocks, the pressure ratio of the transmitted shock to incident shock depends on acoustic impedances, $\rho\, c$, of the materials. In general, the change in pressure due to the different material properties is known as a shock impedance match. It occurs in the analysis of experiments to determine the shock locus of a material, and to determine the initial HE shock pressure for a shock-to-detonation transition discussed in a later section; see [Davis, 1998].

Next we show that the solution to the Riemann problem has 3 waves, one for each wave family; left-facing shock or rarefaction, right-facing shock or rarefaction, and a contact between the left- and right-facing waves. The solution utilizes the concept of a wave curve, and the fact that u and P are continuous across a contact.

For a fixed initial hydro state (P_0, e_0, u_0) the right-facing wave curve is defined as the locus of right-facing shock states in compression and right-facing rarefaction states in expansion. Subject to the standard constraints on the EOS for the materials, such as convexity of isentropes and $\Gamma > 0$ [see, Menikoff and Plohr, 1989], $u(P)$ is single valued and monotonically increasing. The left-facing wave curve is defined analogously but $u(P)$ is monotonically decreasing.

Right- or left-facing wave refers to whether a particle path crosses the wave front from right to left or vice-versa, see figure 2.1. Typically, a right-facing wave propagates to the right. However, due to Galilean invariance of the Euler PDEs, a right-facing wave may be propagating to the left.

In the (u, P)–plane, the solution to the Riemann problem is the intersection of the right-facing wave curve based on the specified right state and the left-facing wave curve based on the specified left state. Due to monotonicity of the wave curves, the intersection is unique, and defines the contact wave. For weak shocks, we note that $\mathsf{d}P/\mathsf{d}u$ is the acoustic impedance, and the intersection of the wave curves can be determined analytically.

There are 5 types of solutions illustrated in figure 2.3 for both the (u, P)–plane and the (x, t)–plane. The type specifies whether the left- and right-facing waves are shocks or rarefactions. We note that the solution is scale invariant, *i.e.*, invariant under the transformation that x and t are multiplied by a constant, as are the initial conditions. Hence, the solution maintains the symmetry of the PDEs. Furhermore, the solution to the Riemann problem is unique.

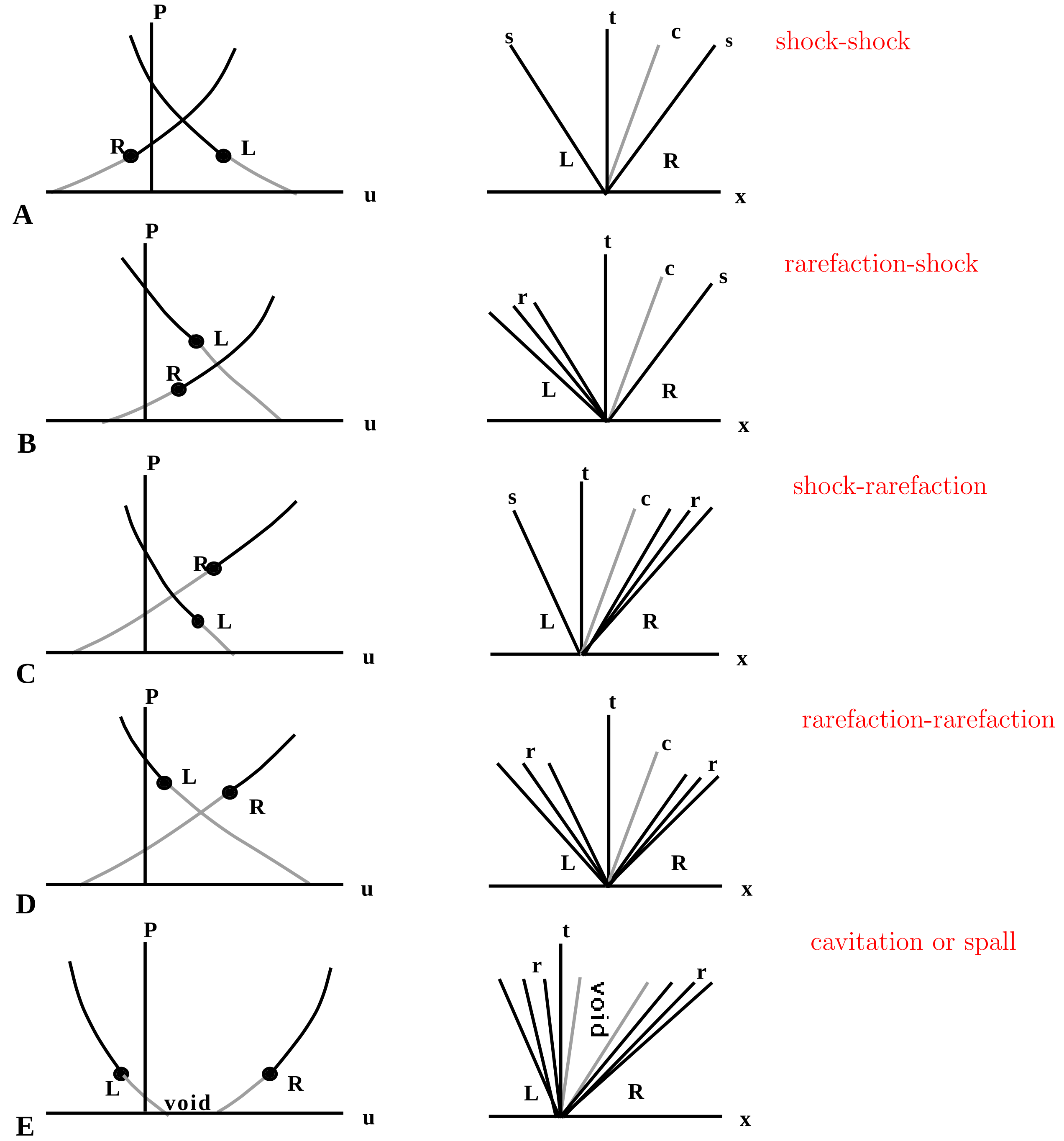

Figure 2.3: Types of solutions to Riemann problem in the (u, P)–plane and (x, t)–plane. In the (u, P)–plane, the solid circles are the initial left (L) and right (R) states. The black and gray curves are the shock and rarefaction loci, respectively. In the wave diagram, (x, t)–plane, the initial left/right interface is at the origin. The contact is the gray line, a rarefaction fan is labeled by ‘r’, and a shock by ‘s’. The red labels on the right hand side indicate wave type (shock or rarefaction) of the left- and right-facing waves.

CHAPTER 3

Shock wave relations

When characteristics cross they give rise to discontinuities known as shock waves. In general, for the PDEs (2.1), discontinuities in the dependent variables, ρ, e, u, with respect to the independent variables, ∂_t or ∂_x, leads to singularities, since the derivative of a step function is ill defined. The singularities can be avoided by imposing constraints on the discontinuities known as the shock jump relations.

The jump relations are determined as follows. First, we assume that a shock wave is quasi-steady; *i.e.*, dependent variables are all of the form $f(x - D\,t)$ in the neighborhood of the shock front, where D is the wave velocity. Second, we shift the velocity with a Galilean transformation to the frame in which the shock front is at rest. Then the jump relations are the condition that the fluxes are continuous across the shock front. For a right-facing shock, it follows from the PDEs in conservation form Eq. (2.1) that the jump relations for mass, momentum and energy are

$$\Delta\big[\rho(u-D)\big] = 0 \ , \tag{3.1a}$$

$$\Delta\big[\rho(u-D)^2 + P\big] = 0 \ , \tag{3.1b}$$

$$\Delta\Big[\rho(u-D)\cdot\big[e + \tfrac{1}{2}(u-D)^2 + P\,V\big]\Big] = 0 \ , \tag{3.1c}$$

where for any function f of the dependent variables, $\Delta[f] = f(x^-) - f(x^+)$ is the jump across the discontinuity at position x, with x^+ ahead and x^- behind the front.

Let the $m = \rho\cdot(u-D)$ be the mass flux through the shock front. Then the jump relations simplify to

$$\rho(u-D) = m \ , \tag{3.2a}$$

$$\Delta\big[\rho(u-D)^2 + P\big] = 0 \ , \tag{3.2b}$$

$$m\cdot\Delta\big[e + \tfrac{1}{2}(u-D)^2 + P\,V\big] = 0 \ , \tag{3.2c}$$

There are 3 cases depending the sign of the mass flux m.

1. Mass flux $m = 0$
   $\Delta[P] = 0$, $\Delta[u] = 0$ and wave speed $D = u$. This corresponds to a **contact wave**; discontinuity in ρ and e with P and u continuous. Moreover, contact discontinuity moves along a particle trajectory.
2. Mass flux $m < 0$
   This corresponds to a **right-facing shock wave** with the ahead state u_0 on the right of the shock front and $m = u_0 - D < 0$.
3. Mass flux $m > 0$
   This corresponds to a **left-facing shock wave** with the ahead state u_0 on the left of the shock front and $m = D - u_0 > 0$.

Several useful shock formulas can be inferred from the shock jump relations. We use the convention that the ahead state is denoted by subscript '0', otherwise variable is at the behind state.

1. From the mass relation, the mass flux is continuous. Hence
   $$\rho_0\,(D - u_0) = \rho\,(D - u) = m\ . \tag{3.3}$$
   It follows that the shock compression ratio is
   $$\boxed{V/V_0 = (D - u)/(D - u_0)}\ . \tag{3.4}$$
2. The momentum relation Eq. (3.2b) can be re-expressed as.
   $$\Delta\big[m^2 V + P\big] = 0\ .$$
   Hence, the Rayleigh line for a point on the shock locus in the (V, P)-plane has slope
   $$-\Delta P/\Delta V = m^2 \text{ or } \boxed{(P - P_0)/(V_0 - V) = m^2}\ . \tag{3.5}$$
3. The momentum relation Eq. (3.2b) can also be expressed as
   $$\begin{aligned} 0 &= \Delta\big[m\,(u - D) + P\big] \\ &= m\,\Delta[u - D] + \Delta[P] \\ &= \rho_0\,(u_0 - D)\,(u - u_0) + \Delta P\ . \end{aligned}$$
   Hence, the shock pressure can be expressed in terms of the shock velocities as
   $$\boxed{P - P_0 = \rho_0\,(D - u_0)\,(u - u_0)}\ . \tag{3.6}$$

4. Alternatively,

$$\begin{aligned} 0 &= \Delta\big[m\,(u-D)+P\big] \\ m^2\,(u-u_0)^2 &= (\Delta[P])^2 \\ -[\Delta P/\Delta V]\,(u-u_0)^2 &= (\Delta[P])^2 \end{aligned}$$

   Hence, the change in particle velocity is

$$\boxed{(u-u_0)^2 = (P-P_0)(V_0-V)}\ . \tag{3.7}$$

5. The energy relation Eq. (3.2c) is equivalent to the Bernoulli function, $e+\frac{1}{2}u^2+P\,V$, being continuous across the shock front. This is a result of the quasi-steady property of a shock wave.

The velocity can be eliminated from the energy jump relation by using the identity

$$\Delta[AB] = \overline{A}\,\Delta[B]+\overline{B}\,\Delta[A]\ , \tag{3.8}$$

where A and B are functions of the dependent variables, and for any function f, its average is $\overline{f}=\frac{1}{2}\,[f(x^-)+f(x^+)]$. The second and third term in the energy Eq. (3.2c) are

$$\begin{aligned} \Delta[\tfrac{1}{2}\,(u-D)^2] &= m^2\,\Delta[\tfrac{1}{2}\,V^2] \\ &= m^2\,\Delta[V]\,\overline{V} \\ &= -\Delta[P]\,\overline{V} \\ \Delta[P\,V] &= \overline{P}\,\Delta[V]+\Delta[P]\,\overline{V} \end{aligned}$$

Combining the terms in Eq. (3.2c) gives

$$\Delta[e]+\overline{P}\,\Delta[V] = 0\ , \tag{3.9}$$

which is equivalent to the **Hugoniot energy equation**

$$\boxed{e = e_0+\tfrac{1}{2}\,(P+P_0)\cdot(V_0-V)}\ , \tag{3.10}$$

where the pressure is specified by the EOS; *i.e.*, $P=P(V,e)$. The shock locus is the set of points (with $V\leq V_0$ for most materials) that satisfy the Hugoniot equation. Frequently, the locus is projected into the (V,P)-plane or the (u,P)-plane. In the (V,P)-plane the locus is the same for right- and left-facing shock waves. It follows from Eq. (3.5) that the right- and left-locus in the (u,P)-plane are reflections of each other about the P-axis.

The Hugoniot equation is used to determine EOS points from experimental measurements of shock waves. Typically, experiments measure the shock speed and particle velocity. Then Eq. (3.6) determines the shock pressure, and Eq. (3.4) the shock specific volume. These equation are typically written in the frame in which the ahead state is at rest, $u_0 = 0$, and using the notation for which u_p is the particle velocity behind the shock front and u_s is the shock velocity;

$$V = (1 - u_p/u_s)\, V_0 \ , \tag{3.11a}$$
$$P = P_0 + \rho_0\, u_p\, u_s \ . \tag{3.11b}$$

The equations can be inverted using Eqs. (3.7, 3.3, and 3.5) to give the particle and shock velocities in terms of the thermodynamic variables

$$u_p = \pm\big[(P - P_0)(V_0 - V)\big]^{1/2} \ , \tag{3.12a}$$
$$u_s = \pm V_0\big[(P - P_0)/(V_0 - V)\big]^{1/2} \ , \tag{3.12b}$$

where ± is '+' and '−' for right- and left-facing waves, respectively.

3.1 Detonation locus

Here we discuss general properties of a detonation wave that are due to the conservation form of the reactive flow PDEs (2.1). In particular, we show that the shock jump relations derived in the previous section extend to the reaction zone of a steady detonation wave; *i.e.*, the jump relations derived in the previous section, Eq. (3.2), apply with flux difference $\Delta[f] = f(x) - f(x_0^+)$, where x_0 is the position of the detonation front (lead shock), and $x < x_0$ is a point within the reaction zone. We note that λ is continuous and does not affect the jump relations. Instead, λ is determined from the rate Eq. (2.2).

The flux difference can be re-expressed as

$$\Delta[f] = \big[f(x) - f(x_0^-)\big] + \big[f(x_0^-) - f(x_0^+)\big] \ . \tag{3.13}$$

For a steady-state wave, conservation requires $\frac{\mathsf{d}}{\mathsf{d}x} f(x) = 0$. Integrating across the interval (x, x_0^-) gives $[f(x) - f(x_0^-)] = 0$. Hence, both bracket terms on the right-hand side of Eq. (3.13) are zero. A consequence of the flux relations is that the shock equations (3.3)–(3.7) also apply to a detonation wave.

With an energy source term, the detonation energy equation is given by

$$e = \lambda Q + e_0 + \tfrac{1}{2}\big[P(V, e, \lambda) + P_0\big] \cdot (V_0 - V) \ . \tag{3.14}$$

The reactants' shock locus and the products' detonation locus correspond to solutions of Eq. (3.14) for $\lambda = 0$ and $\lambda = 1$, respectively. The form of Eq. (3.14) is valid for the reaction energy release in any combination of an explicit energy source term or offset of the energy origin of either the reactants EOS or the products EOS, as discussed previously in section 2.2. Henceforth, for simplicity we assume that the explicit energy source Q is zero.

In contrast to a shock wave, a detonation wave has a profile. The profile is derived in section 2.2 based on the reaction rate and the partly burned loci with fixed λ between 0 and 1. At the end of the reaction zone, $\lambda = 1$. Consequently, the detonation locus (solutions of the energy equation with $\lambda = 1$) determines the possible detonation states without the need to know the reaction rate.

For a shock wave, it can be shown that as $V \to V_0$ and $P \to P_0$, and the shock speed limits to the initial sound speed $D \to \pm c_0$. Hence, the slope of the Rayleigh line limits to $(\rho_0 c_0)^2$. For the strong branch of the detonation locus $P \to P_{CJ}$ and $V \to V_{CJ}$. The detonation speed limits to D_{CJ}, and the Rayleigh line is tangent to the CJ isentrope; $D_{CJ} - u = \pm c$ and $(\rho\, c)^2 = \frac{P-P_0}{V_0-V}$. Hence, overdriven detonation waves limit to the self-supporting CJ detonation. Moreover, the limit of the overdriven detonation locus is tangent to the Rayleigh line at the CJ state. Hence, in the (V,P)-plane the overdriven locus joins up smoothly with the CJ release isentrope as seen in figure 3.1.

At the CJ state, the shock relations and sonic condition can then be expressed as follows:

$$\begin{array}{lll} & & \underline{\text{Ideal HE}}\ \text{with } P_0 = 0 \\ P_{CJ} = \frac{\rho_0 D_{CJ}^2}{\gamma+1-P_0/P_{CJ}} & u_{CJ} = \frac{1-P_0/P_{CJ}}{\gamma+1-P_0/P_{CJ}} D_{CJ} & D_{CJ}^2 = 2(\gamma^2-1)Q \\ V_{CJ} = \frac{\gamma}{\gamma+1-P_0/P_{CJ}} V_0 & c_{CJ} = \frac{\gamma}{\gamma+1-P_0/P_{CJ}} D_{CJ} & e_{CJ} = \frac{D_{CJ}^2}{2(\gamma+1)^2} = \frac{\gamma-1}{\gamma+1} Q \end{array} \tag{3.15}$$

where $\gamma = c^2/(PV)$ is the adiabatic exponent at the CJ state. For an HE, $P_{CJ} \gg P_0$ and to a good approximation the terms P_0/P_{CJ} may be neglected. Typically, $\gamma_{CJ} \approx 3$. In this case, $c_{CJ} = \frac{3}{4} D_{CJ}$ and $u_{CJ} = \frac{1}{4} D_{CJ}$. Moreover, for an ideal HE (§ 2.1.1), $D_{CJ} = 4\, Q^{1/2}$, $e_{cj} = \frac{1}{2} Q$, and $P_{cj} = 2(\gamma-1)\rho_0 Q = 4\,\rho_0\, Q$. In addition, the thermicity is $(\gamma-1)Q/c^2$.

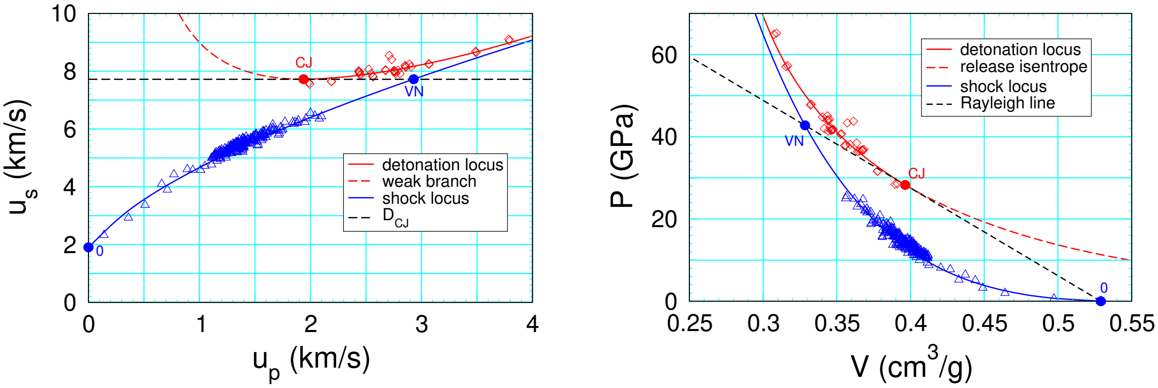

Figure 3.1: Shock and detonation loci for PBX 9502 (at ambient pressure and temperature) in (u_p, u_s)–plane and (V, P)–plane. Symbols are data points.

An illustrative example of the shock and detonation loci, along with experimental data points, are shown in figure 3.1. Several points are worth noting.

1. Experiments measure u_p and u_s and then determine P, V and e from the shock relations. There is a ± 2 or 3 percent scatter in the data. We note that the shock pressure is proportional to the initial density, which can vary with pressing molding powder into a PBX and the temperature of experiments at outdoor firing sites due to thermal expansion. Part of the scatter in the data is due to the fact that each data point is from a separate experiment with a different HE sample. An important question is how much of the scatter is random and how much is due to systematic errors. This affects the extent to which the scatter averages out in calibrating the EOS to the data, especially when there are not a sufficient large number of data points for good statistics.
2. The shock loci of solid reactants in the (u_p, u_s)-plane tend to be concave down at low shock pressure. This is in contrast to metals for which the loci is approximately a straight line up to moderately high pressure; see [Marsh, 1980]. This is due to HE molecules (and most other organic materials in general) not being able to completely fill space because of their irregular shapes, compared to the essentially spherical shapes of metal atoms. Consequently, there is generally an excess "free volume" in organic materials that can be compressed out at lower pressures giving a concave down shape. The effect is somewhat similar to that of 'porosity' in plastics, liquids and sintered metals; see [Menikoff and Kober, 2000b].
3. Overdriven detonation wave experiments require an HE driven flyer plate or projectile from a gas gun to support the detonation wave. One source of errors is due to alignment of the flyer plate with respect to the HE sample. Also, for pressures slightly over P_{CJ}, a sufficiently long length of run is needed to assure a steady state detonation wave has been reached. This is important for HE with a slow reaction; for example due to carbon clustering.
4. The reactants data points come from SDT experiments described in a later chapter. The data points all have a pressure less than P_{CJ}. As the pressure increases, so does the burn rate. A large burn rate affects the velocity measurement. The reaction can give rise to a systematic error in which the data points are shifted up in either the (u_p, u_s)–plane or the (V, P)–plane.
5. To fully determine the steady detonation reaction-zone profile, the reactants EOS is needed within the pressure range $P_{CJ} \leq P \leq P_{VN}$. In this range, the reactants EOS represents an extrapolation which can lower its accuracy. In practice, above P_{VN} the burn rate is so large that the reactants are burned almost immediately and the reactants EOS at these high pressures has little effect on detonation wave simulations.
6. The reactants and products loci are not expected to cross; see discussion on thermicity around Eq. (2.17). This places a constraint on the extrapolation of the reactants EOS to high pressures. Enforcing the constraint can affect the EOS calibration at lower pressures.

3.2 Detonation speed dependence on initial state

A PBX can be pressed to a range of densities. The density can also vary with temperature due to thermal expansion. Over the temperature range $-55 < T < 75\,\mathrm{C}$ the coefficient of thermal expansion is on the order of 10^{-5}/K to 10^{-4}/K. Hence, thermal expansion can affect the density by about 1 percent.

The energy per volume of an explosive is proportional to its density. This in turn affects the CJ state and the detonation speed. Assuming the products are homogeneous and in thermodynamic equilibrium, the CJ detonation speed can be determined by linearizing the Hugoniot Eq. (3.10) and the sonic condition that the Rayleigh line and the CJ isentrope are tangent, $(\rho c)^2 = \frac{P-P_0}{V_0-V}$. The result is [see eq 3.11, Fickett and Davis, 1979, and references therein]

$$\boxed{\frac{\Delta D_{cj}}{D_{cj}} = A\,\frac{\Delta\rho_0}{\rho_0} + B\,\frac{\Delta e_0}{D_{cj}^2}} \tag{3.16a}$$

where

$$A = \frac{\gamma(\gamma-\Gamma-1)}{2\gamma-\Gamma} \quad \text{and} \quad B = \frac{\Gamma}{2\gamma-\Gamma}\,(\gamma+1)^2\ , \tag{3.16b}$$

γ is the adiabatic exponent and Γ is the Grüniesen coefficient. Typically, at the CJ state $\gamma \approx 3$ and $\Gamma \approx 0.5$. In this case, $A \approx 0.82$ and $B \approx 1.45$.

As discussed in Fickett and Davis [1979, §3B,"experimental test of theory"], this relation can also be used as a test of the CJ assumption that the state behind an unsupported detonation is sonic. Without knowing the products EOS, the coefficients A and B can be determined experimentally by measuring the detonation speed as the initial density and initial temperature are varied.

This test was carried out using liquid and pressed TNT by Davis et al. [1965]. It was found that the coefficient A varied by considerable more than the experimental uncertainty. Fickett and Davis [ibid] concluded that one of the assumption of the CJ theory must have broken down.

Though homogenized models are used to model solid HEs, as discussed in the introduction, section 1.4, solid HEs are heterogeneous materials. When the grain size distribution spans the reaction-zone width, the reaction-zone profile is not steady. The heterogeneities gives rise to short-wavelength high-frequency fluctuations in the hydro flow. These fluctuations can affect the local detonation speed and the local position of the sonic point relative to the end of the reaction zone. This violates a basic assumption of the CJ theory used to derive Eq. (3.16); namely, that there is a steady state reaction-zone profile.

Also as noted previously, the precision of the measured detonation speed from a rate stick experiments implies that on a length scale much greater than the reaction-zone width, the fluctuations can average out, leading to a steady detonation speed within a few tenths of per cent. But there can be an energy associated with the fluctuations. If the fluctuation energy varies with the initial state, Eq. (3.16) would be violated.

For pressed TNT the fluctuations are due to porosity, while liquid TNT without bubbles is homogeneous. The reaction zone in the latter case is subject to a transverse instability leading to a cellular wave pattern; see [Fickett and Davis, 1979, §7D]. Also pressed TNT and liquid TNT have a different sensitivity of the burn rate to the lead shock pressure. For pressed TNT, the hotspot burn rate needs to be calibrated, while an Arrhenius rate with a high activation energy should control the rate for liquid TNT. This leads to a qualitatively different curvature effect (detonation speed as function of diameter for an unconfined, or in the case of a liquid weak confined, rate stick; see Campbell and Engelke [1976, fig 2]). Consequently, the reaction-zone profile is very different and undoubtedly so are the fluctuations. Hence, the discrepancy of the detonation speed variation with initial density that Fickett and Davis [1979, §3B,“experimental test of theory”] discussed is likely an effect of fluctuations in the reaction zone due to either material heterogeneities in a solid HE or instabilities leading to transverse waves in a liquid HE.

3.3 Reaction zone heterogeneities

As seen in figure 3.2, PBX 9501 is an example of an HE for which the reaction-zone width and grain scale heterogeneities are comparable. In addition to the grains, the left plot has red guide lines separated by the estimated reaction-zone width of 100 μm based on the curvature effect (discussed in later chapter), and the right plot has illustrative red circles with a 200 μm diameter corresponding to the nominal laser spot size for VISAR and PDV velocity probes.

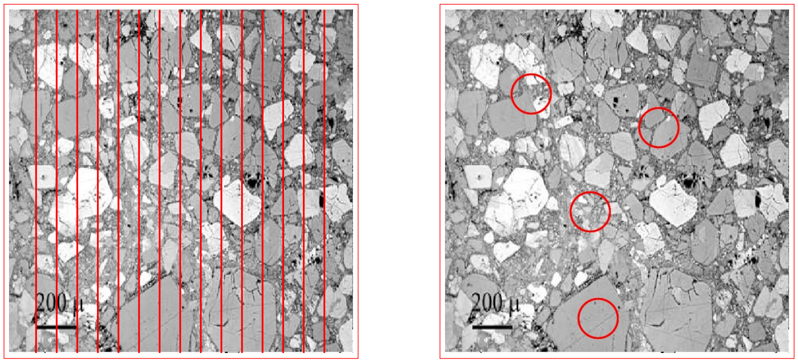

Figure 3.2: Polarized light micrographs for PBX 9501, Skidmore et al. [1998, fig 4]. Red guide lines on left plot are 100 μm apart; the estimated reaction-zone width. Red circles on right plot are 200 μm diameter; laser spot size for VISAR and PDV velocity probes.

For the left plot, consider a detonation wave propagating from left to right. The red guide lines indicate that locally the reaction zone can be within a large single HMX crystal, or can contain small HMX crystals surrounded by a lot of binder, or can be a combination of medium sized crystals separated by a small amount of binder and/or pores. Due to differences in burning and the EOS for the HMX crystals and the binder, the reaction-zone profile can not be steady. It will have short-wavelength high-frequency fluctuations in the flow, both normal to and transverse to the direction of propagation. This will lead to small amplitude irregularities in the shock front at the beginning of the reaction zone and the sonic locus at the end of the reaction zone. Moreover, the von Neumann spike state and the sonic state are likely to fluctuate. Energy associated with the fluctuations can lead to differences between a thermal equilibrium products EOS and a homogenized empirical EOS calibrated to the experimental detonation locus and CJ release isentrope. This would be analogous to the difference between the chemical rate for HMX and an empirical burn rate calibrated to shock-to-detonation transition data.

For the right plot in figure 3.2, consider a detonation wave propagating normal to the plane of the micrograph and impacting a window used with VISAR or PDV probes. The red circles indicate that depending on the position of the probe, it can view either a single HMX crystal, or small HMX crystals with a lot of binder, or a combination of moderate sized crystals with a small amount of binder. When the detonation wave front impacts the window, the shock impedance matches between the HMX crystals and the window and between the binder and the window, will lead to multiple velocities within the probe spot size.

The VISAR analysis assumes a single velocity, while the PDV analysis determines the power spectrum of velocities. To measure the reaction-zone profile, PDV is a better technique. The estimated reaction time for PBX 9501 is about 10 ns. With multiple probes, the PDV resolution of 1 to 2 ns should be adequate to see variations in the reaction-zone profile (excluding the VN spike) due to the heterogeneities. Experiments that measure the reaction-zone profile are described in the next chapter along with steady planar detonation wave profile for homogenized burn model using the 1-D reactive flow PDEs Eq. (2.1).

3.4 Detonation locus from EOS

The detonation locus is determined from the Hugoniot equation for a specified initial state (V_0, e_0) and products EOS. With a general EOS, the locus can not be expressed analytically. Assuming the EOS is convex in the (V, P)–plane, $(\partial^2 P/\partial V^2)_S > 0$, the locus is single valued and can be parameterized by either V or P. It is straightforward to calculate the locus numerically.

For a fixed $V < V_0$, a simple Newton iteration in e can be used to solve for the zero of the

Hugoniot function $h(e;V)$

$$h(e;V) = e - e_0 - \tfrac{1}{2}[P_{prod}(V,e) + P_0]\cdot(V_0 - V) = 0\ . \tag{3.17}$$

This has a solution $e_h(V)$ provided that V_0/V is less than the maximum compression ratio on the locus; *i.e.*, $V > V_{min} = \lim_{P\to\infty} V_h(P)$. Then the locus point is $P_h(V) = P_{prod}\big(V, e_h(V)\big)$. We note that V can correspond to points on either the strong or weak branch of the detonation locus.

Frequently, a Mie-Grüneisen form of EOS is used for the pressure

$$P(V,e) = P_{ref}(V) + \frac{\Gamma(V)}{V}\big[e - e_{ref}(V)\big]\ , \tag{3.18}$$

where the subscript 'ref' denotes a reference curve and the Grüneisen coefficient Γ is a function of only V. The reference curve is typically an isentrope for an HE products EOS. In this case, the Hugoniot function is linear in P and the detonation locus is given by

$$P_h(V) = \frac{P_{ref}(V) - (\Gamma(V)/V)\big[e_{ref}(V) - e_0 - \tfrac{1}{2}P_0\,(V_0 - V)\big]}{1 - \tfrac{1}{2}\Gamma(V)\,(V_0/V - 1)}\ . \tag{3.19}$$

We note that the maximum compression ratio corresponds to the denominator vanishing; *i.e.*, $P_h(V_{min}) = \infty$ for V_{min} such that $1 - \tfrac{1}{2}\Gamma(V_{min})\,(V_0/V_{min} - 1) = 0$.

The CJ state can be determined with a bisection iteration on V to find the point on the detonation locus that satisfies the sonic condition

$$\begin{aligned}(\rho c)^2 &= [\rho(D-u)]^2 = (\rho_0 D)^2\\ &= (P_h - P_0)/(V_0 - V_h)\ ,\end{aligned}$$

where $P_h(V)$ and $e_h(V)$ correspond to a point on the detonation locus and the sound speed $c(V, e_h(V))$ is determined from the products EOS, $(\rho\, c)^2 = -(\partial_V P)_e + P(\partial_e P)_V$. Effectively, the determination of the CJ state is a double iteration. One iteration to find a point on the detonation locus and a second iteration to find the sonic point on the locus. Both iterations are in one variable. They are stable and converge rapidly.

3.4.1 Ideal HE detonation locus

For an ideal HE, see § 2.1.1, the detonation locus can be expressed analytically as a function of pressure. With the simplifying assumption $P_0 = 0$, for $P \ge P_{CJ} = 2(\gamma-1)\rho_0 q$, the specific volume on the strong branch of the detonation locus is given by

$$V(P) = \frac{\gamma-1}{\gamma+1}\left[1 + 2\,\frac{\rho_0\, q}{P}\right] V_0\ . \tag{3.20}$$

The other state variables are determined by the shock jump relations given at the beginning of this chapter. We note for $q = 0$, this reduces to $V = \frac{\gamma-1}{\gamma+1}V_0$, which is the strong shock limit for an ideal gas EOS since $P/P_0 = \infty$. It is also the limit for $P \gg \rho_0\, q$, since the heat release of the reaction is then small compared to the shock energy.

More generally, for $P_0 > 0$, the CJ pressure can be expressed as

$$P_{CJ} = b + [b^2 - c]^{1/2} \ , \tag{3.21a}$$

where

$$b = (\gamma-1)\rho_0 q + P_0 \ , \tag{3.21b}$$

$$c = \left[\tfrac{2(\gamma-1)}{\gamma+1}\rho_0 q + P_0\right] P_0 \ , \tag{3.21c}$$

and for $P \geq P_{CJ}$, the specific volume on the strong branch of the detonation locus is given by

$$\frac{V(P)}{V_0} = \frac{(\gamma-1)\big[P + 2\rho_0 q\big] + (\gamma+1)P_0}{(\gamma+1)P + (\gamma-1)P_0} \ . \tag{3.22}$$

Furthermore, with $q = 0$, this reduces to the reactants shock locus.

3.5 Programmed burn

The programmed burn model was introduced by Wilkins [1965] for numerical simulations of propagating detonation waves in the early days of computing. It is motivated by the Chapman-Jouguet hypothesis that there is a unique detonation speed for an unsupported detonation wave. It applies to CHE with a narrow reaction zone and a small curvature effect (discussed in a later chapter). The model is implemented in two steps:

1. A burn table is precomputed for the detonation time as a function of position, $t_{bt}(x)$, based on a Huygens construction for the evolution of the detonation front with constant wave speed D_{cj}.

2. A pseudo-burn rate is used for the reaction rate

$$\mathcal{R}(x,t,\lambda) = \begin{cases} (1-\lambda)^n\,\tau^{-1} \ , & \text{if } t > t_{bt}(x) \text{ and } \lambda < 1; \\ 0 \ , & \text{otherwise;} \end{cases} \tag{3.23}$$

   where the parameter τ is a time constant for the rate and the parameter $n < 1$ is for the depletion factor to give a finite tail to the numerical reaction zone. The pseudo-burn rate is analogous to artificial viscosity for the dissipation needed by a shock capturing algorithm. With $\tau \sim \Delta x/D_{cj}$, it gives the detonation wave a numerical profile of a few grid cells.

An important issue with the pseudo-burn rate is that it is independent of the hydro-state. Consequently, there is no feedback to keep the hydro front and the burn front in sync; *i.e.*, the leading edges of the pressure profile and reaction progress variable profile should coincide. This can lead to unphysical solutions of the reactive flow PDE, Eq. (2.1), when the detonation speed D used to construct the burn table is not consistent with D_{cj} from the shock jump relations for the products EOS. The inconsistency occurs due to the curvature effect when HE reaction-zone width is not sufficiently small. An extension of programmed burn called detonation shock dynamics (DSD) accounts for curvature effect in constructing the burn table. In a later chapter, the curvature effect will be described in more detail.

3.5.1 Unphysical programmed burn detonation waves

The unphysical detonation waves can be understood from the solutions to the reactive flow PDE for the programmed burn model. It follows from the shock jump relations that a steady wave profile lies along the Rayleigh line as shown in figure 1.1. There are 2 unphysical cases corresponding to the burn table detonation speed D either less than or greater than D_{cj}.

$D < D_{cj}$

In this case the Rayleigh line does not intersect the detonation locus. Instead of a single wave, there is a split wave solution in which a lead shock is followed by a pressure decreasing deflagration wave, as shown in figure 3.3. Since the deflagration wave is subsonic its wave speed is less than that of the lead shock. Consequently, the shock and deflagration waves are separated by a constant state whose width grows in time. This is an unphysical case in which the hydro front leads the burn front.

$D > D_{cj}$

In this case the Rayleigh line intersects the detonation locus at 2 points; one on the strong branch and the other on the weak branch. The state behind the strong detonation is subsonic and therefore it will decay. Thus the stable solution correspond to a weak detonation wave. In this case, the wave is akin to a reactive shock, with the burning occurring in the pressure rise, as shown in figure 3.4, instead of following the lead shock. This is unphysical since there is nothing that can trigger the reaction before the lead shock. Moreover, the flow behind the weak detonation is supersonic, and there is a growing constant state region before the following release wave. Another peculiar property is that the detonation pressure decreases as the detonation speed (and hence the slope of the Rayleigh line) increases.

$D = D_{cj}$

When $D = D_{cj}$ there are 2 possible detonation wave profiles similar to those for the case in which $D > D_{cj}$, except both profiles end at the CJ state. One profile is similar to that

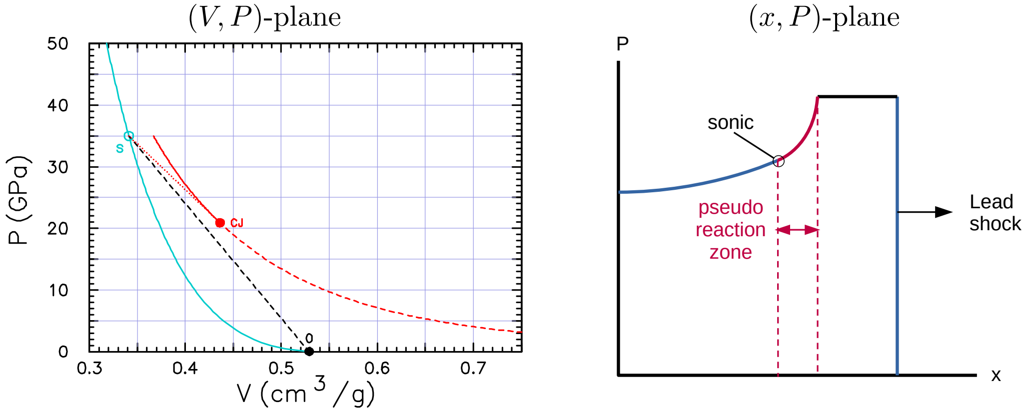

Figure 3.3: Programmed burn solution for $D < D_{cj}$: Lead shock followed by deflagration wave.

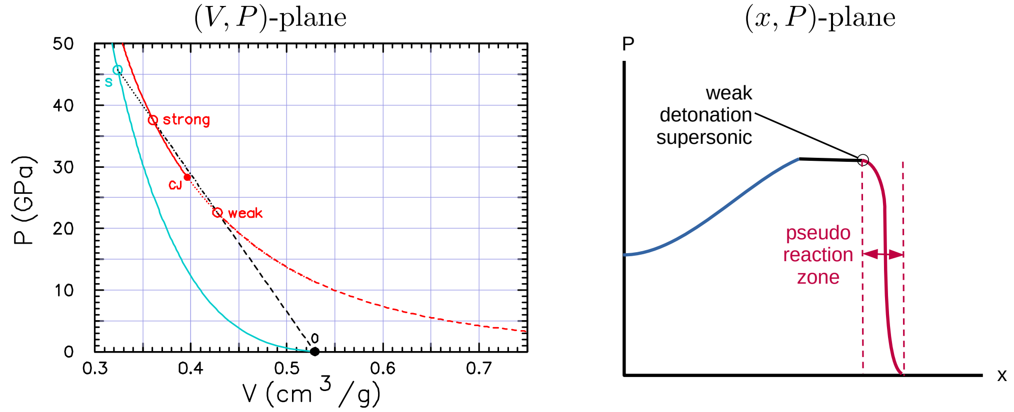

Figure 3.4: Programmed burn solution for $D > D_{cj}$: Supersonic reactive shock.

shown in figure 1.1, a shock to the VN spike state followed by reaction down the Rayleigh line to the CJ state. The second is a reactive shock up the Rayleigh line to the CJ state. The reactive shock profile is more stable and most likely to occur for a programmed burn simulation, especially with coarse resolution.

A natural question is whether missing the VN state is significant. Since the impulse of the spike, $\int dt P(t)$ over the reaction time, is small if the reaction-zone width is very narrow, neglecting the VN state may be adequate for simulations using coarse resolution. We also note that the programmed burn model is designed for propagating detonation waves and is not applicable for shock initiation.

CHAPTER 4

Planar detonation wave

The first detonation model is the Chapman-Jouguet theory (circa 1900). It assumed a propagating detonation wave is a shock like discontinuity from the initial reactants state to the products at the sonic (CJ) state on the detonation locus. This amounts to assuming the reaction-zone width is of zero thickness and hence the reaction rate is infinite.

Physically, the rate is finite and the reaction zone width is non-zero. To account for this, the detonation model of Zeldovich (1940), von Neumann (1942), Doering (1943) — ZND theory — is based on the reactive flow PDEs, Eq. (2.1), with a finite reaction rate. In contrast to the CJ theory, a detonation wave has a structure; lead shock in the reactants followed by a reaction zone, in which the HE burns, to the CJ state in the products.

The advantage of the ZND theory is that it can be used for both shock initiation and propagation of a detonation wave. In addition, the reactive flow PDEs can account for multi-dimensional effects that depend on the reaction-zone width, such as the decrease in the detonation speed with the curvature of the detonation front, as discussed in a later chapter.

In this chapter, we discuss the structure and properties of a detonation wave in one-dimension. First, the ZND wave structure is described. Then its properties are derived from the PDEs. Finally, the reaction zone is compared with experimental data. The comparison is limited in part by experimental resolution and by heterogeneities not accounted for in the reactive flow PDEs, which as described previously represent a homogenized model.

4.1 ZND wave structure

An illustrative example of a wave diagram for a steady planar detonation wave is shown in figure 4.1. Since the CJ state is sonic with respect to the detonation front, the end of

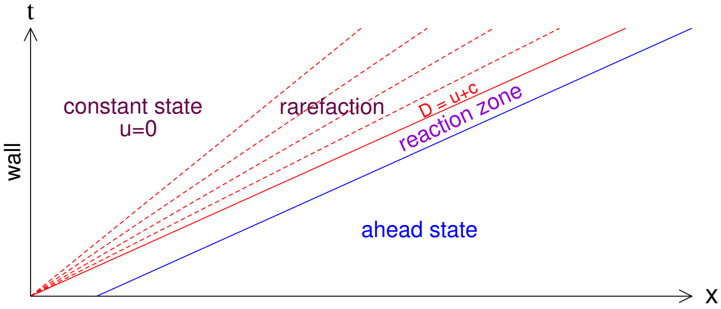

Figure 4.1: Wave diagram for a steady detonation wave followed by a release wave. The red lines correspond to right-facing characteristics; see Eq. (2.13a). The slope of the rays are $t/x = 1/(u+c)$. The solid red line corresponds to the locus in time of sonic points at which the head of the rarefaction wave joints up with the end of the reaction zone.

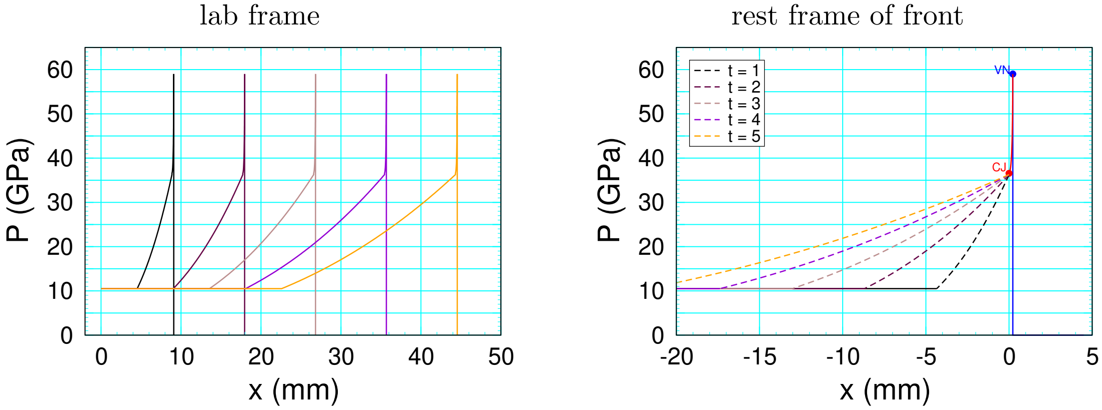

Figure 4.2: Time sequence of pressure profiles in the lab frame and the rest frame of the detonation front. The pressure at the end of the release rarefaction corresponds to a wall boundary condition at $x = 0$.

the reaction zone coincides with the head of the rarefaction. This property implies that the reaction zone is acoustically decoupled from the flow behind; *i.e.*, $x - D\,t < 0$ in figure 4.1. The rarefaction or release wave from the CJ state is known as the Taylor wave. The steady part of the flow refers to the reaction zone. The rarefaction wave spreads out in time as shown in the wave diagram. The rarefaction is followed by a constant state with $u = 0$, which corresponds to a rigid wall boundary condition.

A time sequence of pressure profiles corresponding to the wave diagram is shown in figure 4.2. The pressure at the end of the release wave corresponds to the point on rarefaction with $u = 0$; *i.e.*, a rigid wall boundary condition behind the release wave. The spreading out of the rarefaction is clearly seen in the rest frame of the front.

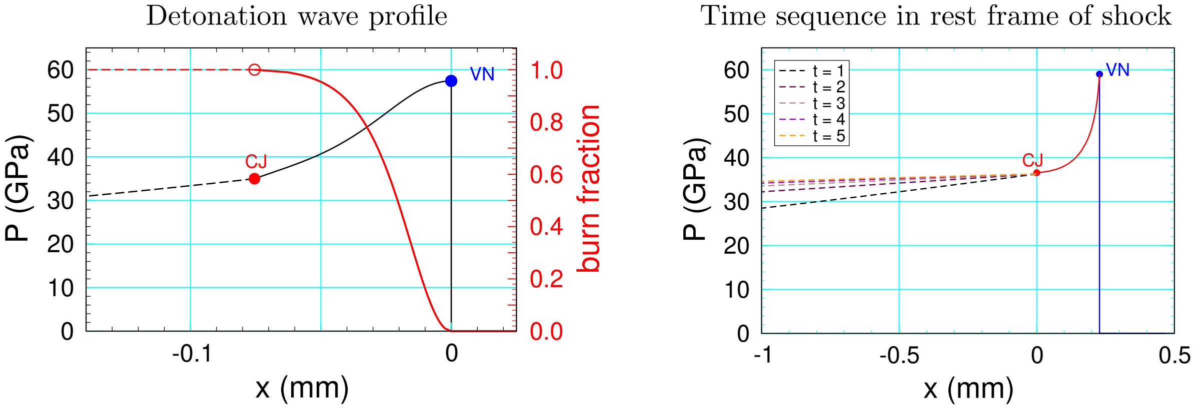

Figure 4.3: Zoomed in detonation wave profile. Reaction-zone profiles of the pressure (black) and products mass fraction (red), and rarefaction wave (dashed black). Right plot shows time sequence.

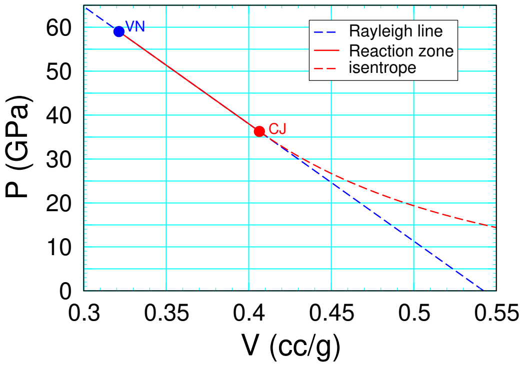

Figure 4.4: Wave trajectories in the (V, P)–plane. Solid and dashed red lines correspond to ZND reaction zone and release wave respectively. Dashed blue line is Rayleigh line through the CJ state.

Figure 4.3 zooms in on the reaction-zone pressure profile. On a length scale much larger than the reaction-zone width (typically about 0.1 mm), the reaction zone appears to have a sharp falloff after the initial shock rise. Hence, the designation of the lead shock as the von Neumann (VN) spike.

On the length scale of the reaction-zone width, behind the lead shock the pressure profile is smooth, except for the kink at the CJ state. In principle, the kink should allow the CJ state to be readily identified. As discuss in a later section, experimentally the kink is smeared out, which can lead to a large uncertainty in the CJ state. With a sequence of profiles, the right plot in figure 4.3, the release waves all start to diverge at the CJ state. This allows the CJ state to be better determined.

Figure 4.3 shows the detonation wave locus in the (V, P)–plane. The reaction zone is along the Rayleigh line and the rarefaction is an isentrope. Though the trajectory of the rarefaction is time dependent, the locus of the isentrope in the (V, P)–plane is independent of time. This simplification allows a semi-analytic solution to be derived for a steady planar detonation wave.

A non-intuitive feature of the ZND profile is that the pressure decreases as the HE burns. This is due to the negative slope of the Rayleigh line; *i.e.*, V increases as P decreases.

The end of the reaction zone is strongly affected by the dependence of the rate on $1 - \lambda$, which is called the depletion factor. Typically, the rate has the form

$$\mathcal{R}(V, e, \lambda) \to (1 - \lambda)^{\nu} f(V, e) \ , \quad \text{as } \lambda \to 1 \ , \tag{4.1}$$

where f depends only on the thermodynamic state (V, e).

To leading order in $1-\lambda$, near the end of the reaction zone, $\lambda(t)$ is determined by integrating the equation

$$(\mathsf{d}/\mathsf{d}t)\lambda = f(V_{cj}, e_{cj})(1 - \lambda)^{\nu} \ . \tag{4.2}$$

There are 3 possibilities for the parameter ν.

1. $0 < \nu < 1$ corresponds to a hotspot burn rate [Starkenberg, 2002, § General Forms]
   The burn time and reaction-zone width are finite,
   $1 - \lambda(t) \propto (t_{cj} - t)^{1/(1-\nu)}$ as $t \nearrow t_{cj}$,
   where t_{cj} is the time at which burning is complete.

2. $\nu = 1$ corresponds to a first order chemical reaction rate.
   The reaction zone has an exponential tail,
   $1 - \lambda(t) \propto \exp(-t)$ as $t \to \infty$.

3. $\nu > 1$ corresponds to a higher order chemical reaction rate.
   The reaction zone has an algebraic tail,
   $1 - \lambda(t) \propto t^{-1/(\nu-1)}$ as $t \to \infty$.

As a consequence, for $0 < \nu < 1$, the slope of the reaction-zone profile at the CJ state, $\frac{\mathsf{d}P}{\mathsf{d}x}$, is monotonically increasing from 0 at $\nu = 1$ to ∞ as $\nu \to 0$. Moreover, as the slope decreases, the tail of the reaction zone gets longer. This behavior is illustrated in figure 4.5.

The entropy change on the shock locus is third order $\mathcal{O}\left((1 - V/V_0)^3\right)$ at the initial state. In contrast, for the detonation locus the entropy change is second order at the CJ state. Consequently, in the neighborhood of the CJ state

$$P_h(V) = P_{cj} + m^2(V_{\mathrm{cj}} - V) + \rho\, c^2 \mathcal{G} \cdot \mathcal{O}\left((1 - V_{cj}/V)^2\right) \tag{4.3}$$

where for the shock locus $\mathcal{G} = \frac{V^2}{2\rho\, c^2}\left(\frac{\partial^2 P}{\partial V^2}\right)_S$ is a dimensionless measure of the curvature of an isentrope, also known as the fundamental derivative of fluid dynamics. To accommodate the increase in entropy, the value of the parameter $\mathcal{G}$ in the Taylor expansion for P_h must be larger than the fundamental derivative in the expansion of the shock locus.

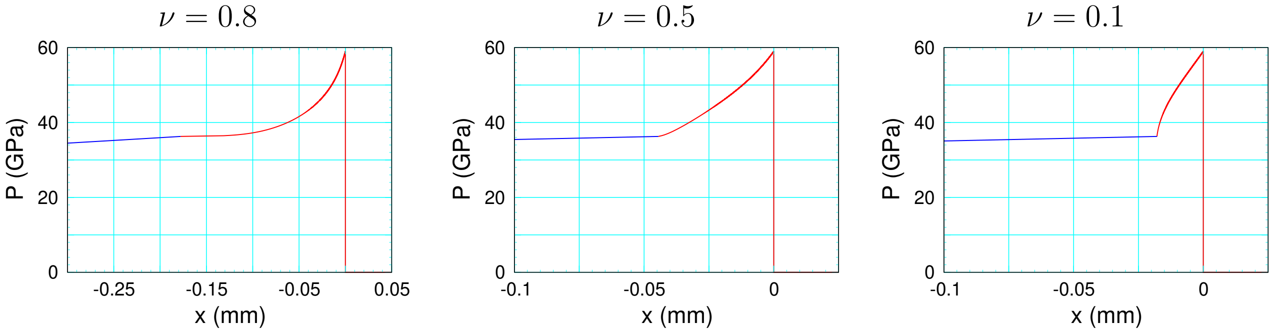

Figure 4.5: ZND pressure profiles for rate $\mathcal{R} = (1-\lambda)^\nu\, P^n$ with $n = 3.5$ and selected values of ν. Red and blue lines correspond to the reaction zone and release wave, respectively. Note that the x-scale is 2.5 × larger for the $\nu = 0.8$ case.

4.2 Derivation of ZND reaction-zone profile

For a steady detonation wave, the dependent variables (ρ, e, u, λ) are all functions of the variable $\xi = x - D\,t$, where D is the wave speed. The reactive flow PDEs, Eq. (2.1), can then be reduced to ODEs. The 3 ODEs corresponding to conservation mass, momentum and energy are perfect differentials. They can be integrated leading to the mass, momentum and energy fluxes being constant across the detonation front and through out the reaction zone. The fluxes being constant are equivalent to the shock jump relations. Details are given in [Menikoff, 2022a].

From the mass and momentum jump relations, Eqs. (3.6) and (3.4), it follows that $P = P_0 + m^2(V_0 - V)$, where $m = \rho\,(D-u)$ is the mass flux in the rest frame of the shock front. Therefore, the trajectory of the detonation profile lies along a Rayleigh line in the (V, P)–plane. The fourth ODE, for the reaction progress variable, is the rate equation

$$\frac{\mathsf{d}}{\mathsf{d}\xi}\lambda = -\,\frac{\mathcal{R}}{D-u}\ . \tag{4.4}$$

Next we derive the ZND detonation profile from the partially burned loci and Eq. (4.4).

Figure 4.6 shows an illustrative example of a family of partly burned loci in the (V, P)–plane. These loci are determined from the Hugoniot equation and the initial state of the reactants. The general features of the loci depend on 2 properties of the products EOS:
1. Burning increases the pressure; *i.e.*, $(\partial P/\partial\lambda)_{V,e} > 0)$ and the thermicity is positive.
2. For fixed λ, the EOS is convex; *i.e.*, $\partial^2 P/\partial V^2)_{S,\lambda} > 0$. This implies that the mass flux is monotonically increasing with pressure on the strong branch of a detonation locus and decreasing on the weak branch; see for example [Henderson and Menikoff, 1998, theorem 1] and [Menikoff and Plohr, 1989, eq 4.26].

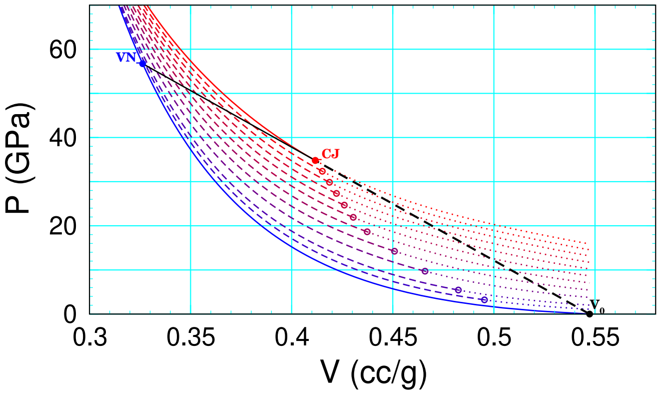

Figure 4.6: Partly burned detonation loci for PBX 9501. The loci are color coded for λ in steps of 0.1 from unreacted (blue, $\lambda = 0$) to fully reacted (red, $\lambda = 1$) and one additional locus with $\lambda = 0.05$. The dashed curves are the strong (subsonic) branch and the dotted curves are the weak (supersonic) branch. Open circles denote the sonic point on each locus. The black curve is the Rayleigh line through the CJ state. The CJ detonation profile corresponds to the solid portion of the Rayleigh line extending from the unreacted VN state to the fully reacted CJ state. The solid blue and red curves are the shock locus of the reactants and the strong branch of the detonation locus, respectively.

The key properties of the loci seen in figure 4.6 are:

1. The partly burned loci cover the region between the shock ($\lambda = 0$) and detonation ($\lambda = 1$) loci.
2. The loci with different m do not cross.
3. The segment of the Rayleigh line between the VN state and the CJ state intersects each loci exactly once. Moreover, the intersection is on the strong branch of each loci. Hence, the reaction zone is subsonic with respect to the front, except for the CJ state which is sonic.

The mass flux m can be thought of as a parameter that selects a unique Rayleigh line. The last property implies that for a given m, the hydro variables are a function of only λ, which are denoted $\widetilde{V}(\lambda; m)$, $\widetilde{e}(\lambda; m)$, $\widetilde{P}(\lambda; m)$, and $\widetilde{u}(\lambda; m)$. The equation for the reaction progress variable is then

$$\frac{\mathsf{d}}{\mathsf{d}\xi}\lambda = -\frac{\mathcal{R}\big(\widetilde{V}(\lambda; m), \widetilde{e}(\lambda; m), \lambda)\big)}{D - \widetilde{u}(\lambda; m)} \ . \tag{4.5}$$

Integrating this equation for $m_{cj} = [(P_{cj} - P_0)/(V_0 - V_{cj}]^{1/2}$ starting at $\lambda = 0$ then gives the ZND profile for an unsupported detonation wave. The same ODE with $m > m_{cj}$ determines the profile for an overdriven detonation wave. There is no profile for a point on the weak branch of the detonation locus.

The profile analysis here is kinematic. Since the dynamics within the reaction zone is neglected, it determines an explicit wave profile for any reaction rate. Hence, the existence of a planar detonation. In 1-D there is also the issue of galloping instability, which depends on the details of the reaction rate; see [Fickett and Davis, 1979, § 6A] and references therein.

To complete the derivation of the ZND profile, for each λ we need to compute a point on the Rayleigh line with a specified mass flux m. This can be done efficiently using a Newton iteration in the variable $V_h = \widetilde{V}(\lambda; m)$ for the zero of the function $f(V_h)$ defined as follows

$$\begin{aligned} e_h(V_h) &= \lambda Q + e_0 + \tfrac{1}{2} m^2 (V_0 - V_h)^2 + P_0\,(V_0 - V_h) \\ P_h(V_h) &= P(V_h, e_h(V_h), \lambda) \\ f(V_h) &= P_h(V_h) - P_0 - m^2 (V_0 - V_h) \end{aligned}$$

where e_h is from the Hugoniot equation and P_h is from the EOS. The iteration is then

$$\begin{aligned} f'(V_h) &= -(c/V_h)^2 + \Gamma\left[P_h(V_h) - P_0 - m^2\,(V_0 - V_h)\right]/V_h + m^2 \\ V_h &\to V_h - f(V_h)/f'(V_h) \end{aligned}$$

where c and Γ are from the EOS at (V_h, e_h, λ). For integrating Eq. (4.5), the iteration for V_h can start with the value from the last time step. The iteration for V_h is robust and converges in a few iteration.

It is instructive to derive alternative ODEs for the ZND profile that do not require the solution of a non-linear equation on each time step. Another ODE can be derived in analogy to the above Newton iteration. Let $e_h(V)$ be the Hugoniot energy on the Rayleigh line and $f(V, \lambda) = 0$ the equation for the Rayleigh line

$$e_h(V) = e_0 + \tfrac{1}{2} m^2 (V_0 - V)^2 + P_0\,(V_0 - V)\ , \tag{4.6a}$$

$$f(V, \lambda) = P(V, e_h(V), \lambda) - P_0 - m^2 (V_0 - V)\ . \tag{4.6b}$$

Then we derive an ODE for V starting with

$$0 = \frac{\mathsf{d}}{\mathsf{d}\xi} f(V, \lambda) = \left[(\partial_V P)_{e,\lambda} + m^2\right] \frac{\mathsf{d}}{\mathsf{d}\xi} V + (\partial_e P)_{V,\lambda} \frac{\mathsf{d}e_h}{\mathsf{d}V} \frac{\mathsf{d}}{\mathsf{d}\xi} V + (\partial_\lambda P)_{V,e} \frac{\mathsf{d}}{\mathsf{d}\xi} \lambda\ . \tag{4.7}$$

Using the thermodynamic relations

$$(\partial_V P)_{e,\lambda} = -(\gamma - \Gamma) P/V\ , \tag{4.8a}$$

$$(\partial_e P)_{V,\lambda} = \Gamma/V\ , \tag{4.8b}$$

$$(\partial_\lambda P)_{V,e} = \rho\, c^2 \sigma\ , \tag{4.8c}$$

and Eq. (4.4), Eq. (4.7) can be reduced as follows

$$\left\{\left[-(\gamma-\Gamma)\frac{P}{V}+m^2\right]+\frac{\Gamma}{V}\left[-m^2(V_0-V)-P_0\right]\right\}\frac{\mathsf{d}}{\mathsf{d}\xi}V+\rho\,c^2\sigma\frac{\mathsf{d}}{\mathsf{d}\xi}\lambda=0 \tag{4.9a}$$

$$\left[-\gamma\frac{P}{V}+m^2\right]\frac{\mathsf{d}}{\mathsf{d}\xi}V=\frac{\rho\,c^2\sigma}{D-u}\,\mathcal{R} \tag{4.9b}$$

$$\left[c^2-(D-u)^2\right]\frac{\mathsf{d}}{\mathsf{d}\xi}V=-\frac{c^2}{m}\,\sigma\,\mathcal{R} \tag{4.9c}$$

The reaction-zone profile is then determined by a system of 2 ODEs

$$\left[c^2-(D-u)^2\right]\frac{\mathsf{d}}{\mathsf{d}\xi}V=-\frac{c^2}{m}\,\sigma\,\mathcal{R} \tag{4.10a}$$

$$\frac{\mathsf{d}}{\mathsf{d}\xi}\lambda=-\frac{\mathcal{R}(V,e,\lambda)}{D-u}\ , \tag{4.10b}$$

plus algebraic equations for the other hydro variables

$$P=P_0+m^2(V_0-V) \tag{4.11a}$$

$$e=e_0+\tfrac{1}{2}m^2(V_0-V)^2+P_0(V_0-V)\ , \tag{4.11b}$$

$$u=u_0+(P-P_0)/m\ . \tag{4.11c}$$

For a planar detonation front, the end of the reaction zone is sonic and the rate goes to zero. This avoids a singularity in the profile. For a diverging detonation wave, we will see in a later chapter that the sonic point lies within the reaction zone and avoiding the singularity determines the detonation speed as a function of the front curvature. The complication is that the wave profile is not exactly on the Rayleigh line. An important result is that the detonation speed of a diverging detonation wave is less than the minimum detonation speed for a planar detonation.

A physically important quantity for a detonation wave is the reaction time along a particle path. From the equation for the reaction progress variable, $\mathsf{d}\lambda/\mathsf{d}t=\mathcal{R}$, the differential of the reaction time τ is given by

$$\mathsf{d}\tau=\frac{\mathsf{d}\lambda}{\mathcal{R}}=-\frac{\mathsf{d}\xi}{D-u}\ . \tag{4.12a}$$

It can be calculated along with the wave profile by adding an auxiliary or passive ODE to the system for the reaction-zone profile

$$\frac{\mathsf{d}}{\mathsf{d}\xi}\tau=-\frac{1}{D-u(\xi)}\ . \tag{4.12b}$$

In terms of the reaction-zone width, w such that $\lambda(-w) = 1$, the reaction time is bounded by

$$\frac{w}{D} < \tau < \frac{w}{D - u_h} \ , \tag{4.12c}$$

where u_h is the particle velocity on the detonation locus; *i.e.*, at the end of the reaction zone. The bounds follow from the monotonicity of $u(\xi)$. More generally, a Lagrangian time history can be expressed parametrically; for example the pressure time history along a particle path $P(t)$ is given by $t = \tau(\xi)$ and $P(\xi)$ for ξ in the interval $-w \le \xi \le 0$.

4.2.1 Taylor wave

The release wave behind the reaction-zone profile shown in the wave diagram, figure 4.1, is a right-facing rarefaction wave in the products. The hydro state for the rarefaction is determined by the ODEs

$$\frac{\mathsf{d}}{\mathsf{d}V}\begin{pmatrix} e \\ u \end{pmatrix} = -\begin{pmatrix} P(V,e) \\ c(V,e)/V \end{pmatrix} \ . \tag{4.13}$$

The first component defines an isentrope, which follows from the fundamental thermodynamic identity $\mathsf{d}e = -P\,\mathsf{d}V + T\,\mathsf{d}S$. The second component for the particle velocity is a consequence of the characteristic equation Eq. (2.13b); *i.e.*, the left-facing Riemann invariant is constant. The ODE trajectory starts at the CJ state $(V_{\mathrm{cj}},\ e_{\mathrm{cj}},\ u_{\mathrm{cj}})$ in order for the release wave to match up continuously with the ZND profile at the end of the reaction zone. The integration continues until the particle velocity matches up with the back boundary, which for the wave diagram, figure 4.1, is $u = 0$ for a rigid wall.

Provided that the EOS is convex, the characteristic speed within the rarefaction, $u + c$, varies monotonically with V. Consequently, the rarefaction can be parameterized by the characteristic speed. Moreover, since the entropy and the left Riemann invariant are constants, the $u + c$ characteristics are straight lines in the (x, t)–plane as shown in figure 4.1.

A complete solution to the reactive fluid equation for an unsupported detonation wave can be constructed as follows. Let Q represent a hydrodynamic variable; $V, e, u,\ P$ or c. Let $Q_{\mathrm{RFR}}(\zeta)$ represent the CJ trajectory of the right-facing rarefaction (RFR) ODEs but parameterized by the characteristic speed, $\zeta = u + c$, and q_t denote the characteristic speed at the tail of the rarefaction. Let $Q_{\mathrm{ZND}}(\xi)$ represent the CJ reaction-zone profile parameterized by ξ as determined in the previous section, but shifted in space such that $\xi_{\mathrm{cj}} = 0$ and $\xi_{vn} > 0$ correspond to the end and start of the reaction zone, respectively. A detonation wave solution for $t > 0$ is given by

$$Q(x,t) = \begin{cases} Q_{\mathrm{RFR}}(q_t) & \text{constant state for } x \le q_t\, t \\ Q_{\mathrm{RFR}}(x/t) & \text{rarefaction wave for } q_t\, t < x \le D_{\mathrm{cj}}\, t \\ Q_{\mathrm{ZND}}(x - D_{\mathrm{cj}} t) & \text{ZND profile for } D_{\mathrm{cj}}\, t < x \le D_{\mathrm{cj}}\, t + \xi_{vn} \\ \text{ahead state} & \text{constant state for } D_{\mathrm{cj}}\, t + \xi_{vn} < x \end{cases} \tag{4.14}$$

For $t \to 0$ there is a discontinuity at $x = 0$. It is resolved into a centered rarefaction for $t > 0$ with only kinks (discontinuity in spatial derivative) at the head and tail of the rarefaction wave. Because of the kinks, the head and tail of a rarefaction are often referred to as weak singularities. This is in contrast to a shock front for which the hydrodynamic variables themselves are discontinuous. For hyperbolic PDEs in 2 variables, such as the reactive fluid equations with 1 space and 1 time variable, weak singularities can only occur along characteristics.

A steady detonation wave in 1-dimension is frequently used as a verification test problem for reactive hydro codes. The semi-analytic solution constructed here is valid for any EOS and any reaction rate. Taking advantage of the form of the solution, *i.e.*, the wave diagram shown in figure 4.1, reduces the solution to ODEs which are well behaved and can be accurately determined numerically. This facilitates comparisons with numerical solutions of the PDEs allowing the accuracy of a code to be assessed.

More generally a family of rarefactions can be constructed as follows. Let $h(\zeta)$ be a monotonically increasing function of the characteristic speed with range from q_t to D_{cj}. Then for $t > t_0$, a non-centered rarefaction can be expressed as $Q(x,t) = Q_{\mathrm{RFR}}\big(h(x)\big)$ where $x = x_0 + Q_{\mathrm{RFR}}\big(h(x_0)\big)(t - t_0)$. Non-centered rarefactions behind a detonation wave reaction zone may occur after shock initiation and affect the kink at the CJ state.

4.2.2 Simulated detonation wave profile

With sufficient resolution, a ZND type profile occurs in numerical simulations. Figure 4.7 is an illustrative example of detonation profiles on axis for the cylinder test (see § 9.2.1) with the conventional HE PBX 9501. Since PBX 9501 has a narrow reaction zone (≈ 70 microns for rate model used in the simulations) compared to the diameter of the HE cylinder (25.4 mm), the curvature of the detonation front is small and the reaction-zone profile is nearly the same as for a planar detonation. For fine resolution, the reaction zone is well resolved. The main difference with the ZND profile is that the lead shock has a numerical width of about 4 cells, which is typical of shock capturing algorithms. Also, the kink in the detonation wave profile between the end of the reaction zone and the start of the release wave is smeared out over a few cells.

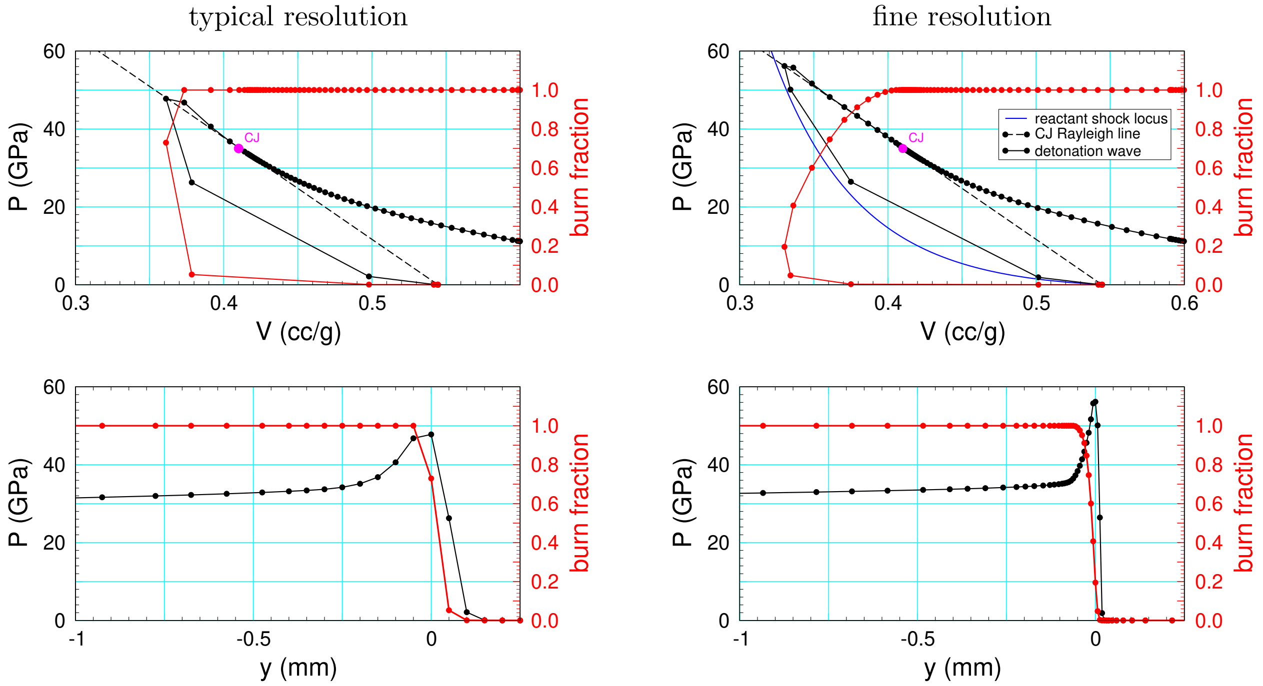

Figure 4.7: Effect of resolution on simulated detonation wave. Circles are grid points. Blue curve is reactants shock locus. Magenta symbol is the CJ state. Simulations use adaptive mesh refinement (AMR). Fine resolution has a cell size of 6.25 micron in the reaction zone. The more typical resolution is 50 microns. For details of simulations see [Menikoff, 2019b].

For the typical resolution, there are only 3 cells in the reaction-zone profile. Moreover, a substantial amount of burning occurs in the lead shock rise. This results in a lower peak pressure than that of the VN spike state. In addition, due to truncation errors, burning ends about 3 cells ahead of the CJ state with a pressure significantly above the CJ pressure. With a CFL number for the time step of less than 0.25, a time history of the reaction progress variable is better resolved than its spatial profile.

Despite the poor resolution of the reaction zone, the CJ state and hence the release wave is nearly the same as that of the fine resolution simulation. This indicates that with an empirical pressure dependent burn rate, a steady underdriven detonation wave is numerically stable. In contrast, an underdriven detonation wave for an ideal HE with a high activation energy Arrhenius reaction rate is physically unstable; see [Fickett and Davis, 1979, § 6A and § 6C] and references therein. The instability leads to a non-steady detonation wave with transverse waves propagating behind the detonation front; *i.e.*, rather than quenching the detonation, the structure of the reaction zone changes from steady to time dependent.

4.3 Reaction-zone profile experiments

Measurements of the reaction-zone profile of a detonation wave only became possible with the development of Doppler velocimetry diagnostics; VISAR (velocity interferometry system for any reflector), see [Barker, 2000] and references therein, and PDV (photonic Doppler velocimeter), see [Strand et al., 2006] and [Dolan, 2020]. Profile experiments consist of an HE cylinder with a planar detonation wave promptly initiated by a projectile from a gas gun or a shock wave driven by a HE plane wave lens. The cylinder needs to be wide enough such that the detonation wave in the neighborhood of the axis is planar, yet long enough such that the reaction zone on axis reaches a steady state; *i.e.*, the flow is 1-D and steady in the neighborhood of the axis. Typically, length/diameter $\lesssim \frac{1}{2}$ is used since the detonation speed and the reactants shock speed is greater than the sound speed. A window of PMMA or LiF is glued to the end of the cylinder with fiber optic VISAR or PDV probes attached to the window surface in the vicinity of the HE axis. A laser beam is sent down the fiber and diffuse reflected light off the window/HE interface is captured by the fiber for the velocimetry measurement of the Lagrangian time history of the particle velocity.

For a VISAR probe, the velocimetry determines the time history of an average particle velocity over the laser spot size. For a PDV probe, the power spectrum of the reflected light determines multiple velocities over the laser spot size. The spot size can vary from 0.5 mm down to about 60 microns. For the velocity measurement the temporal resolution can be as fine as 1 to 2 ns. As we will see below, velocity time histories with PDV probes are compatible with a ZND reaction-zone profile. However, there can be issues from velocity fluctuations (both spatial and temporal) due to heterogeneities within the reaction zone (as seen for example in figure 3.2) leading to multiple time varying particle velocities over the laser spot size reducing the time accuracy. Also 1 ns time resolution may not be fine enough to measure the peak velocity at the VN spike for PBXs with high burn rates of several $100/\mu$s.

4.3.1 Simulated profile experiment

To understand the qualitative features of profile experiments, we first look at simulated profiles. Simulations of PBX 9501 are used as an illustrative example. The simulations use the EOS model specified in [Menikoff, 2014a, App. A1 and A2], and the reaction rate model given in [Menikoff, 2020, see fig 3]. The rate in the high pressure regime for detonation wave propagation is fit to curvature effect data [see, Menikoff, 2021a, § 5 and fig 12], which depends mostly on the reaction-zone width rather than the particular fitting form for the rate.

The shock and detonation loci for the EOS model, along with experimental data, are shown in figure 4.8 . We note that HMX is the explosive component of PBX 9501, and that without porosity an HMX crystal has a much lower reaction rate than PBX 9501; chemical reaction

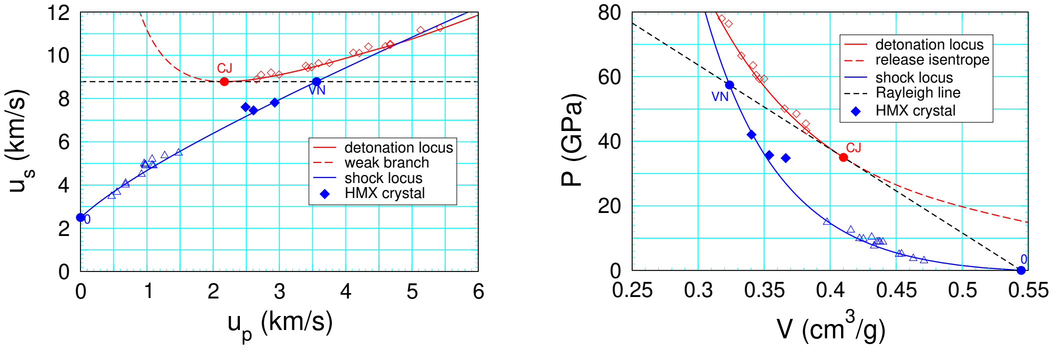

Figure 4.8: Model EOS for PBX 9501 reactants and products.

rate vs hotspot burn rate discussed in chapter 6. This allows for the measurement of shock points at high pressure. The 3 highest data points on the shock locus in figure 4.8 are for single crystal HMX [see, Campbell and Travis, 1986, table 4].

One expects an HMX crystal to be stiffer than the binder; *i.e.*, lower compression ratio, $1-V/V_0$, for a given shock pressure. Consequently, the HMX data points should lie above the PBX 9501 shock locus in the (V,P)–plane and to the left of the locus in the (u_p,u_s)–plane. Furthermore, as HE burns it is expected that the heat release is positive and specific volume to expand. From Eq. (2.17) this implies the thermicity is positive. This in turn implies that the shock and detonation loci do not cross. (The crossing of the loci in figure 4.8 limits the EOS model domain to a pressure below 90 GPa. Since this is considerably higher than P_{VN}, it does not affect the ZND profile.) For the shock locus to be smooth and fit the high pressure data points, the VN spike pressure can not be much lower than the 57 GPa shown in figure 4.8 .

The graphical analysis that accounts for the impedance mismatch when the detonation wave impacts the window is shown in figure 4.9. (Technically, the window CJ state lies on the rarefaction locus from the VN state. Approximating the rarefaction locus with the shock locus, as shown in the figure for simplicity, can introduce an error of up to 1 or 2 percent in the window CJ state.) The analysis assumes that the EOS of the window materials are known. For the HE, only the detonation speed D and hence the slope of the Rayleigh line, $\rho_0 D$ in the (u,P)–plane, are assumed known. For given window states VN and CJ, the equations derived below determine the VN and CJ states of the HE. Picking out the VN and CJ states of the windows from the velocity time history data is discussed later in the experimental data subsection.

We note that the LiF shock locus lies above the PBX 9501 locus in the (u,P)–plane; *i.e.*, LiF has a higher shock impedance than PBX 9501. Consequently, the match of the lead PBX 9501 shock into the LiF window results in a reflected shock in the PBX 9501. Similarly, PMMA has a lower impedance than PBX 9501, and the match of the lead PBX 9501 shock

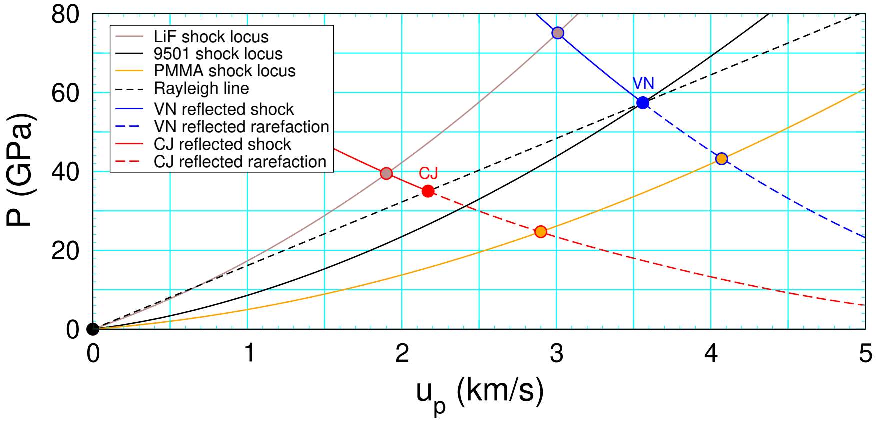

Figure 4.9: Graphical impedance match of PBX 9501 detonation wave impacting PMMA and LiF windows based on EOS model.

into the PMMA window results in a reflected rarefaction in the PBX 9501. (Experiments have shown that PMMA decomposes at the detonation pressure of PBX 9501 [Gustavsen et al., 1998, fig 2], and becomes opaque after 0.5 μs. This can affect the index of refraction, hence, the accuracy of the velocity measurement. In addition, PMMA shock data [see, Marsh, 1980, p 446] shows decomposition starting at $u_p \approx 2.2$ km/s, which corresponds to a shock pressure of about 16 GPa. For detonation profile experiments with a PMMA window, one needs a model EOS for PMMA fit to pressures above that at which the decomposition starts.)

The slope of the reflected HE wave curve (shock locus for increasing pressure and rarefaction locus for decreasing pressure) from the VN state is steeper than from the CJ state. This illustrates the fact that the wave curve depends on the initial state for the shock and rarefaction loci. Since the EOS of the HE is not assumed, the HE wave curves at the VN and CJ state are not a priori known. Instead, we assume that the reflected HE waves are weak. Then the reflected wave curves are linearised and fit to data for 2 windows, one with a higher and the other with a lower impedance relative to the HE.

To leading order in $\Delta u = |u_{win} - u_{VN}|$, the reflected wave speed can be approximated by the sound speed, and the impedance match equation for the VN state is

$$P_{VN} = P_{winVN} - \rho_{VN}\, c_{VN}\, (u_{VN} - u_{winVN}) \ . \tag{4.15a}$$

Since the entropy is third order in shock strength, Eq. (4.15a) applies to both a weak reflected shock, $u_{VN} > u_{winVN}$, and a weak reflected rarefaction $u_{VN} < u_{winVN}$. From the shock jump conditions, the HE shock pressure and density are

$$P_{VN} = P_0 + \rho_0\, D\, u_{VN} \ , \tag{4.16}$$

$$\rho_{VN} = \frac{D}{D - u_{VN}}\, \rho_0 \ . \tag{4.17}$$

Effectively Eq. (4.15a) has two unknowns; u_{VN} and c_{VN}. These can be determined by fitting the impedance match equation to data (P_{winVN} and u_{winVN}) for two different windows; *i.e.*, solving 2 equations for 2 unknowns.

The analogous impedance match equation for the CJ state is

$$P_{winCJ} = P_{CJ} + \rho_{CJ}\, c_{CJ}(u_{CJ} - u_{win})\ . \tag{4.18a}$$

The sonic condition $c_{CJ} = D - u_{CJ}$ and the mass flux relations gives

$$\rho_{CJ} c_{CJ} = \rho_{CJ}(D - u_{CJ}) = \rho_0 D\ . \tag{4.18b}$$

Substituting for the shock pressure,

$$P_{CJ} = \rho_0\, D\, u_{CJ}\ , \tag{4.18c}$$

the impedance match equation (4.18a) is then

$$P_{winCJ} = \rho_0 D\, u_{CJ} + \rho_0 D\, (u_{CJ} - u_{winCJ})\ , \tag{4.18d}$$

which reduces to

$$P_{CJ} = \tfrac{1}{2}\, (P_{winCJ} + \rho_0 D\, u_{winCJ})\ . \tag{4.18e}$$

To give more flexibility in fitting data from 2 windows, one can add the first order term for the reflected HE shock speed, $u_s = c_{CJ} + s\,\Delta u$, where $\Delta u = u_{winCJ} - u_{CJ}$. The impedance match equation is then

$$P_{winCJ} = P_{CJ} - \rho_{CJ}\, (c_{CJ} + s\,\Delta u)\,\Delta u\ . \tag{4.19}$$

Here we treat s as a parameter. If one knew the EOS of the HE, it can be shown that $s = \mathcal{G}/2$. After some algebraic manipulation, Eq. (4.19) reduces to

$$P_{CJ} = \tfrac{1}{2}\left[P_{winCJ} + \rho_0 D\, u_{winCJ} + s\,\rho_{CJ}\,(\Delta u)^2\right]\ . \tag{4.20}$$

Since the HE density is

$$\rho_{CJ} = \frac{D}{D - u_{CJ}}\,\rho_0\ , \tag{4.21}$$

effectively Eq. (4.20) has 2 unknowns; u_{CJ} and s. They can be determined by solving the impedance match equation (4.20) for data (P_{winCJ} and u_{winCJ}) from 2 different windows.

Simulated velocity profiles at the PBX/window interface are shown in figure 4.10. In addition to the change in the peak (VN spike) from the impedance match of the lead shock, there is also a slight change in the profile shape from the reflected wave in the reaction zone.

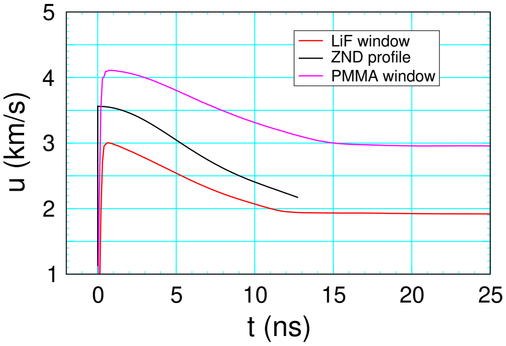

Figure 4.10: Comparison of simulated velocity time histories for ZND profile and impedance match with LiF and PMMA windows. The window profiles also show release wave.

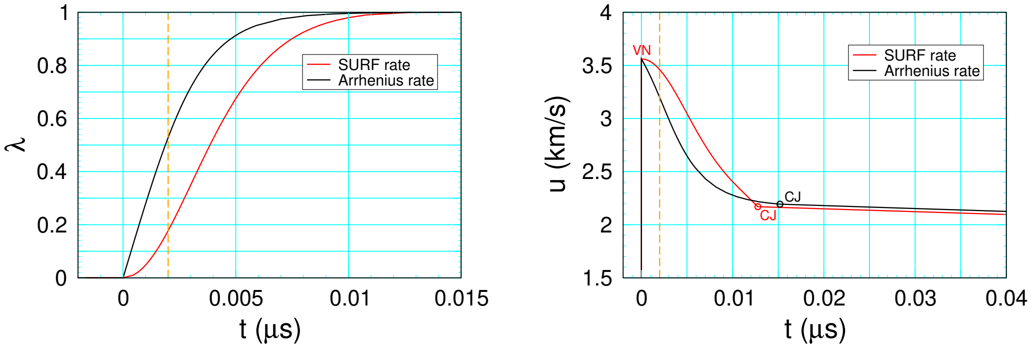

Figure 4.11: Comparison of velocity and reaction-progress variable time histories for 2 model burn rates. Dashed orange guide line is 2 ns after the lead shock.

Moreover, the reaction time for a higher impedance window, which gives a reflected shock, is shorter than the ZND profile reaction time, which in turn has a shorter reaction time than for a lower impedance window which gives a reflected rarefaction.

Another point to note is that the shape of the velocity profile depends on the rate model. Figure 4.11 shows a comparison of the simulated velocity profiles for 2 different rate models (chemical Arrhenius rate and SURF model hotspot burn rate), adjusted to give approximately the same reaction time. The SURF rate neglects the initial volume of hotspots and consequentially has a 2 ns delay for the rate ramping up to a realistic value. For the Arrhenius rate, the profiles of the velocity and reaction progress variable have very large initial slopes. If fluctuations from the heterogeneities decrease the timing resolution of the VISAR and PDV diagnostics [see, Dolan, 2020, §VII] from the nominal value of 2 ns, then the measured peak lead shock velocity could be clipped by 10 to 20 percent; with the Arrhenius rate, $\lambda \approx 0.5$ at 2 ns, and the peak velocity would correspond to a point on a partially burned detonation locus rather than the VN spike point on the reactants locus, and similarly for hotspot burn rate without the initial 2 ns delay.

The rate models also differ in the depletion factor; $(1-\lambda)^\nu$ with $\nu = 1$ and 0.5 for the Arrhenius rate and SURF rate, respectively. This affects the tail of the profile as discussed after Eq. (4.2) and shown in figure 4.5. Even for finite reaction-zone length, for example figure 4.5 with $\nu = 0.8$, there would be a large uncertainty in the experimental value of u_{winCJ} needed for the graphical analysis that determines P_{CJ}.

To get around this issue, a series of experiments with different propagation lengths for the detonation wave can be performed; *i.e.*, experiments with different lengths of the HE sample. When the velocity time histories are shifted such that the lead shock for all the experiments coincide, the time independent reaction zone can be separated from the time dependent rarefaction; see figure 4.3.

Alternatively, the length of the HE can be held fixed and the shock strength can be varied. This varies the run distance to detonation, and effectively the length for propagating a steady detonation wave.

We note that in general shock initiation gives rise to a simple wave or rarefaction since a steady reaction zone would advect a constant entropy along particle paths and a constant Riemann invariant for the backwards characteristic to the flow behind the sonic point. But the profile of the Riemann invariant for the forward characteristic can vary. Thus, the slope of the rarefaction wave can depend on the pressure pulse initiating the HE as well as the distance of run. This suggests the comparison of the velocity profiles would be cleaner if the detonation wave for all experiments in a series were promptly initiated with the same drive pressure pulse and only the run distance is used to vary the slope of the rarefaction wave.

4.3.2 Experimental PBX 9501-like profiles

PBX 9501 is 95 wt percent HMX with a binder consisting of 2.5 percent estane and 2.5 percent BDNPA/BDNPF. It is a well characterized explosive with a fast hotspot reaction rate. The grain scale heterogeneities are shown in figure 3.2. The last PBX 9501 series of profile experiments with VISAR probes were by Gustavsen et al. [1998]. They had unresolved issues with the accuracy of the VISAR diagnostic. Here we discuss 2 more recent series of experiments using PDV probes and PBXs with 95 wt percent HMX.

The first series of experiments is by Gustavsen et al. [2009] for EDC-29, which has a polyurethane binder. The second series is by Pei et al. [2019]. The binder is not specified, but the stated initial density and detonation speed are nearly the same as for PBX 9501. Both series used projectiles from a gas gun to drive a shock wave into cylindrical HE samples and initiate a detonation wave. The HE cylinders were 50.8 mm diameter by 23 mm long for the first series, and 40 mm diameter by 10 mm long for the second. Both series used PDV probes with a LiF window. The reported laser probe spot sizes were 60 μm and less than

200 μm, respectively, and the temporal resolution is 1 to 2 ns; see Pei et al. [2019, § II.D]. Though not specified, we assume that the grain and pore distributions are similar to that of PBX 9501. This is consistent with the experimental data showing comparable reaction times and hence similar hotspot reaction rates.

First series

For the first series, the velocity profiles are shown in figure 4.12. As indicated in the legend, the 4 experiments used different shock strengths to initiate the HE. This effectively varies the run distance to initiate a detonation wave. Since the HE length is constant, the longer the initiation distance, the shorter the propagation distance of the steady detonation. Effectively, this varies the slope of the release wave.

The experimentalists commented that the velocity profile is noisier than for TATB based explosives. They suggested that this results from hydrodynamic fluctuation not averaged out when the probe spot size (60 μm) is much less than the average grain size (150 μm). This is compatible with simple 1-D model of fluctuations from heterogeneities [Menikoff, 2020], which shows that hydro fluctuations in the reaction zone generate high-frequency short-wavelength acoustic noise that advect into the region behind the sonic point. Moreover, the noise is long lived as viscosity and heat conduction are too small to damp the noise on the μs time scale of detonation wave experiments.

There are two anomalies in the measured profiles. First, the release wave velocity for the green profile is significantly above the other profiles. This is likely due to the laser probe spot being over a grain much larger than the spot-size; average grain size of 150 μm and the laser spot size 60 μm. Since the explosive is 95 wt percent HMX, locally a single large grain would give rise to an energy fluctuation of 5 %. It would also perturb the position of the sonic point, which would affect the time when the release wave starts.

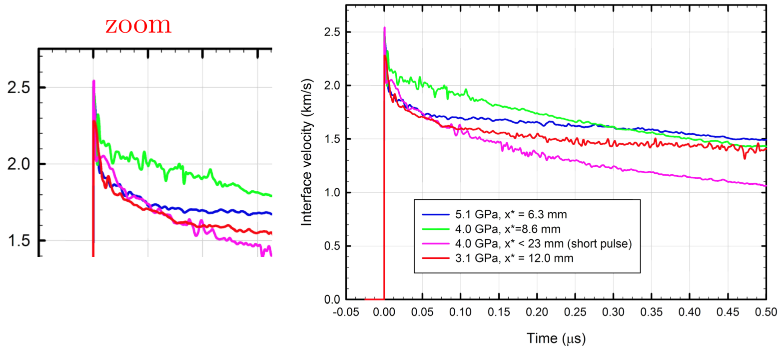

Figure 4.12: PDV velocity profiles for EDC-29 from experiments by Gustavsen et al. [2009, fig 5]. Legend gives the initial shock pressure and run-distance for initiating a detonation wave in EDC-29.

The second anomaly is that the point of divergence for the other 3 profiles occurs at different times; about 0.06 to 0.07 μs for the blue and red curves and 0.10 to 0.11 for the red and magenta curves, rather than at the same CJ point as ZND theory predicts for a steady detonation of a homogeneous explosive shown in figure 4.3. This is also likely due to hydrodynamic fluctuations from heterogeneities. It implies that locally the CJ state is smeared out and not a point. From the experimental time histories, excluding the outlier (green curve in figure 4.3), the winCJ state would occur at a time between 0.06 and 0.11 μs, and velocity between 1.55 and 1.7 mm/ μs. The velocity uncertainty from the heterogeneities is $\pm 4.6\,\%$, which is larger than the measurement uncertainty of 1 to 2 percent.

Second series

The PDV velocity profiles with a LiF window from the second series of experiments are shown in figure 4.13. The figure also shows the PDV signal spectrum for one of the 3 experiments; S1-1. In contrast to the previous series, the experiments all had the same drive conditions; a detonation wave promptly initiated within 1 mm by a 10.9 GPa shock, and then propagated for 9 mm before impacting the window.

An anomalous feature of the profiles are a 1 cycle oscillation behind the steep slope corresponding to the reaction zone. Except for this, the velocity profiles look like the expected ZND profiles. Averaging out the oscillation would result in a profile similar to the red curve for experiment S1-2. It has a fairly abrupt change in the slope at a velocity of about 2 mm/μs. This velocity is slightly higher (about 1.9 mm/μs) than that of the impedance match shown in the wave diagram for PBX 9501, see figure 4.9.

In contrast to the previous series, for which the kink at the CJ point is not apparent, the divergence of the profiles gives a lower u_{winCJ}; between 1.55 and 1.7 mm/ μs. We note that the reaction time is within the uncertainty for the previous series; 0.10 μs versus between

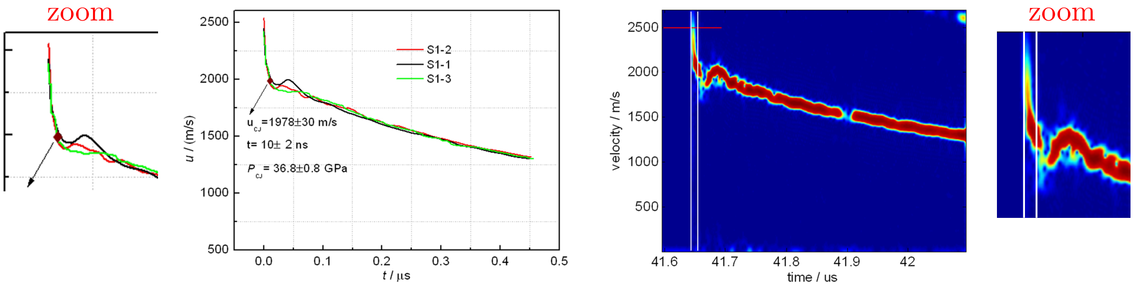

Figure 4.13: PDV velocity profiles (left) for 'PBX 9501 like' detonation wave into Li-F window and PDV signal spectrum (right) from experiments by Pei et al. [2019, figs 4 and 3a]. Zoomed regions are in the neighborhood of the reaction zone. Spacing of white guide lines indicates reaction time of ≈ 10 ns.

0.06 to 0.11 μs. The difference between experimental profiles may be due to differences in the depletion factor of the reaction rate which affects the tail of reaction zone (see figure 4.5), or the laser spot size for the PDV probes.

The oscillation in the profiles may be due to drop outs in the power spectrum; see for example figure 4.13 at $t = 41.9\,\mu$s and $t = 41.66\,\mu$s. It has been suggested that the drop outs are due to a speckle pattern from coherent laser light reflecting off a rough surface [see, Dolan, 2020, §VII.B Signal variation]. In this case, the rough surface would be the laser probe spot size with a distribution of grain sizes and orientations.

The PDV power spectrum also shows a lower intensity and larger velocity variation in the reaction zone than in the release wave. In addition, the spectrum in the reaction zone varies significantly among the 3 PDV experiments; see Pei et al. [2019, fig 3]. The larger velocity variation is indicative of multiple velocities and/or hydrodynamic fluctuations over the laser probe spot-size from PBX heterogeneities on the length scale of the reaction-zone width. The velocity fluctuation would cause a jitter in the position of the CJ state, and increase the kinetic energy over that from the jump conditions used by the ZND model for the reaction zone of a detonation wave, which assumes a homogeneous HE; see [Menikoff, 2020].

We note that the peak velocity of the experimental profile is 15 to 20 percent lower than the VN spike velocity based on an EOS model used for the wave diagram, figure 4.9. Very likely, the peak is clipped due to the large reaction rate that causes a rapid falloff in the velocity behind VN spike. That is, the reaction zone is not resolved in the vicinity of the VN spike.

4.3.3 Experimental PBX 9502-like profiles

PBX 9502 is 95 wt percent TATB with a binder of Kel-F 800. As noted in section 1.2, the TATB reaction produces an excess of carbon, which then forms clusters. The energy released as the clusters grow in size is characterized by a slow reaction rate [Shaw and Johnson, 1987] compared to the fast hotspot reaction rate.

A consequence of the slow reaction rate is that there is a relatively long reaction-zone length and a slow approach to steady state; see [Bdzil and Davis, 1975] and numerical simulations in the next subsection. We shall see that the slow approach to steady state is a complication for measuring the ZND reaction-zone profile.

Here we discuss 2 series of profile experiments. The first is by Seitz et al. [1989] using a variation of VISAR called ORVIS (Optically Recording Velocity Interferometer System); see review by Barker [2000] and references therein. The second is by Gustavsen et al. [2009] using EDC-35 (same composition as PBX 9502) and cold (-55 C) PBX 9502.

The first series of experiments is very extensive. We limit our discussion to those experiments using LiF windows, which is the same type window as used in the second series. The first series had a temporal resolution of 2 to 4 ns with a laser spot-size on target of 65 microns, compared to 1 to 2 ns resolution and spot size of 60 microns for the second series.

For the first series of experiments, the HE samples were promptly shock initiated with a sustained shock (about 1 mm of run distance) after which a detonation wave propagated over run lengths of 13, 25 and 50 mm in cylinders with a diameter to length ratio of at least 2. The initiation shock was driven by an explosive charge assembly utilizing a planar wave lens with diameter of 102 mm.

The second series used a projectile from a gas gun with bore diameter of 50.8 mm to drive a shock that initiated the HE sample. The pressure loading varied the initiation run distance in HE cylinders with a diameter of 50.8 mm and length of 23 mm.

The setups, though not exactly the same, are close enough to meaningfully compare the detonation profiles for the two series.

First series

The profiles for the first series of experiments are shown in figure 4.14. For a fixed time, they show the velocity increasing with the thickness of the HE sample; *i.e.*, length of run after initiation of the detonation wave. This implies that the reaction zone is not steady; *i.e.*, the slow reaction has not completed.

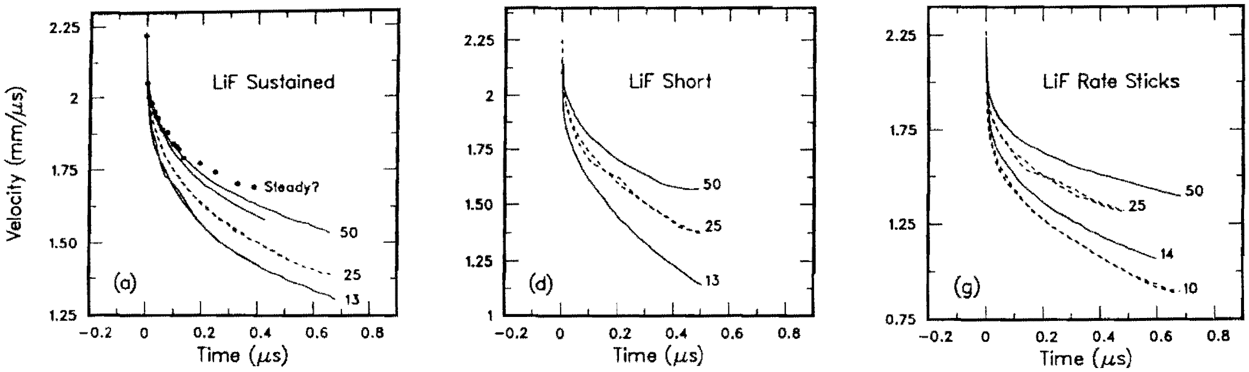

Figure 4.14: ORVIS velocity profiles for PBX 9502 from experiments by Seitz et al. [1989, fig 4a, 4d, 4g] with LiF windows. Sustained and short are planar case with initiation by sustained shock and shock followed shock followed by steep rarefaction, respectively. Rate sticks are non-planar case with unsupported PBX 9502 cylinder. Numbers after curves are the cylinder length in mm for the sustained and short shock initiation, and the diameter for the rate stick. Solid circle "Steady state?" are estimated steady state values from extrapolating velocities with different HE diameters at fixed time. Note, the ranges of the vertical scale are not the same.

Rather than going to larger charges (which is limited by the plane wave lens), the experimentalists extrapolated the profiles from the 3 lengths; 13, 25 and 50 mm. They also did experiments with unconfined rate sticks, and measured the velocity profile on axis; see [Seitz et al., 1989, fig 4g]. The rate sticks are inherently 2-D, but the approach to steady state is much faster than for a planar detonation wave. Despite the 25 and 50 mm diameter rate sticks having length to diameter ratio of 10, the profiles for the rate sticks have a dependence on diameter similar to that of length on the sustained shock experiments. This is due to the curvature effect, discuss in a later chapter, which was not well understood at the time (1989) and not commented on in the paper.

The experimentalist stated in their conclusion “No indication of a classical CJ state (i.e., the end of the reaction zone) has been observed” and “in none of the experiments performed have we definitely observed the steady reaction-zone detonation-wave profile of PBX 9502.” Not observing the CJ state is due to limiting the profile data to $t < 0.7\,\mu$s and the steady state reaction zone ending about $0.8\,\mu$s as seen in the next series.

Second series

The profile data for the second series is shown in figure 4.15. Key points are as follows:

1. The profiles for EDC 35, cold PBX 9502 and the 25 mm length sustained shock of the previous series, see first plot of figure 4.14, are all in good agreement.
2. The profiles for both EDC 35 and cold PBX 9502 show a divergence starting at about $0.9\,\mu$s. The start of the divergence should correspond the CJ point.

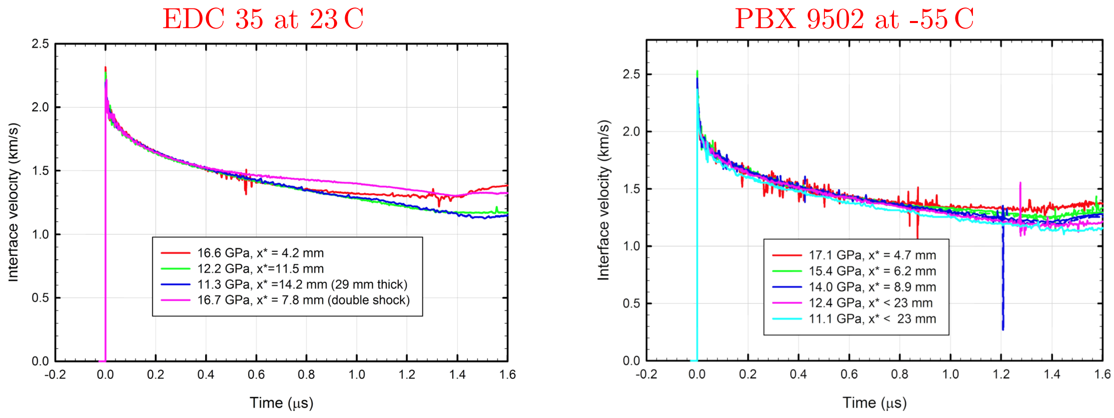
EDC 35 at 23 C

PBX 9502 at -55 C

Figure 4.15: PDV velocity profiles for EDC-35 and cold (-55 C) PBX 9502 from experiments by Gustavsen et al. [2009, figs 3 & 4]. Legend gives initial shock pressure and run-distance for initiating detonation wave in HE.

3. The variation of the pressure initiation is intended to vary the run distance after initiation to make the divergence of the profiles at the start of the rarefaction wave stand out better. The previous series showed that the reaction zone has not reached a steady state at 25 mm of run, which is the thickness of the sample HE for the second series. Consequently, one would also expect the non-steady reaction zone to show a divergence of the profiles before the CJ state is reached.

   The EDC 35 profiles shows no evidence of a non-steady reaction zone. Moreover, they have surprisingly little noise. The cold 9502 profiles shows a small width from the multiple profiles. The effect only on the width may be in part due to the 13 and 25 mm length profiles in the previous series becoming parallel and reducing the non-steady affect to a small translation. Resolving the apparent inconsistency with the non-steady reaction zone is important for interpreting the data.

4. EDC 35 profiles shows the slope changes sign at 1.4 μs for the green and dark blue profiles, and red profile at about 1.2 μs. This indicates side rarefaction have reached the axis of the HE sample cylinder and data at later times should not be used.

   A longer HE sample length would require a larger diameter cylinder. However, the diameter of the sample is constrained by the bore of the gas gun driving the projectile that initiates the HE sample. Thus, with the current system, it is not possible to extend the data to larger times. Fortunately, the CJ state occurs before the side rarefactions.

5. The magenta profile for EDC 35 looks like an outlier. It is the only profile with the HE sample initiated with a double shock.

Simulated approach to steady state

For PBX 9502, the slow rate is due to carbon clustering and described by a model due to Shaw and Johnson [1987]. Later experiments described in [Gustavsen et al., 2017a] are largely in agreement with the model. In contrast to rate models, they showed that carbon clustering is a diffusion process. Moreover, the clusters size and hence the reaction time is finite. A dominate aspect of the model is that the energy released as the cluster size increases goes as $e - e_{eq} \propto t^{-1/3}$ over a finite time interval, where e_{eq} is the equilibrium value of the specific energy. The simulations here use the SURFplus model [Menikoff and Shaw, 2012] to build in the time dependence for the growth of the cluster size, (atoms per cluster linear in time). The cluster model is empirically fit to the curvature effect; [Menikoff, 2017b].

Here we illustrate the slow approach to steady state of an underdriven or unsupported detonation wave compared to a supported or overdriven detonation wave. One-D simulations initiate a reactive wave with either a small hotspot (1 mm) at the CJ state or a strong shock from projectile impact. One measure for the approach to steady state is the distance of run for the wave to reach, within a specified tolerance, a steady wave speed corresponding to a point

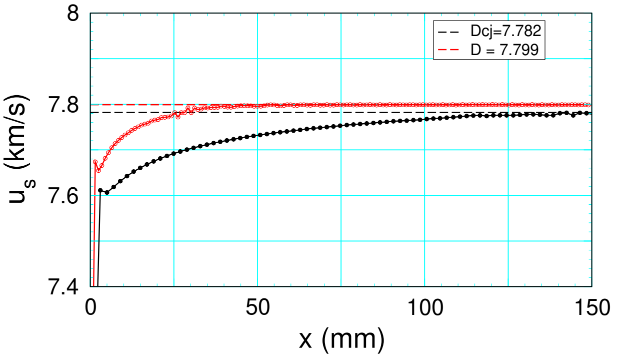

Figure 4.16: Simulated wave speed for PBX 9502 showing approach to steady state for unsupported (black) and slightly overdriven (red) detonation waves; see [Menikoff, 2019a, fig. 10] for details.

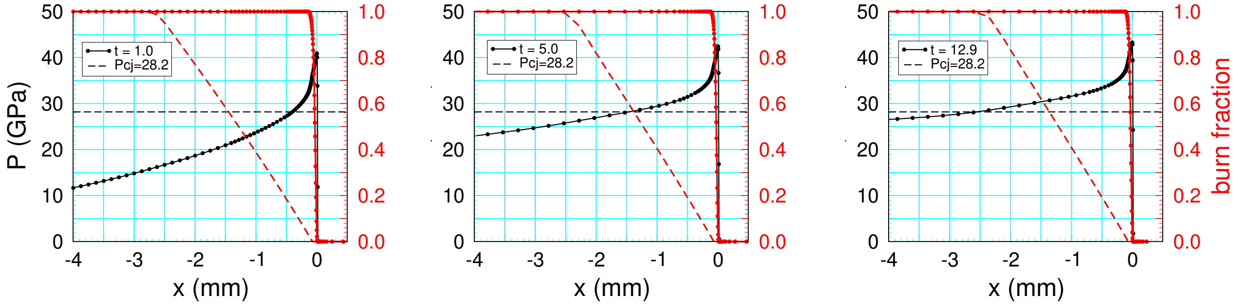

Figure 4.17: Simulated pressure and reaction progress variables profiles at selected times for PBX 9502 showing the approach to steady state for unsupported detonation wave; see [Menikoff, 2019a, fig. 5] for details. Solid black curve is pressure profile. Dashed black line is guide line for CJ pressure. Solid and dashed red curves correspond to reaction progress variables for fast and slow reactions, respectively.

on the detonation locus. This is shown in figure 4.16 for both an unsupported and a slightly overdriven detonation waves. For the unsupported case it takes between 125 and 150 mm of run to reach the CJ detonation speed, comparable to what Seitz et al. [1989] found in their PBX 9502 profile experiments. The slightly overdriven case reaches a steady detonation speed in a shorter distance of run, about 30 mm. The large difference is due to the sonic point at the end of the unsupported reaction zone, since signal travel at the characteristic velocity ($u + c - D \to 0$ at the sonic point) and take a relatively long time to travel from a neighborhood of the end of the reaction zone to the front.

The time sequence of pressure profiles shown in figure 4.17 is a more detailed view on the approach to steady state for an unsupported detonation wave.

Several points to note:

1. The initiation of the detonation wave is due to the fast rate. At the end of the fast reaction, $P > P_{CJ}$.

2. The distance from the lead shock to the point on the profile with $P = P_{CJ}$ increases with time. At this point, the second reaction progress variable increases with time.

3. Since the part of the profile with $P > P_{CJ}$ changes with time, the flow in this interval must be subsonic relative to the front. The release wave is supersonic. Hence there must be sonic point with $P_{\text{sonic}} < P_{CJ}$. The sonic point would be at a point such that the second slow reaction has not completed.

4. Steady state is reached when the pressure at the end of the slow reaction is P_{CJ}.

5. There is no sharp kink in the pressure profile to indicate the position of the CJ state.

Steady state rate stick profile

One set of experiments by Seitz et al. [1989] used unconfined rate sticks. They noted that steady 2-D flow could be achieved easier than steady planar flow. There rate stick profiles at several diameters (up to 50 mm diameter and length to diameter ratio of 10) can be seen in plot (g) of figure 4.14. Their data cut off at a time 0.7 μs. If the data extended up to 1 μs, they likely would have identified the CJ state.

The rate stick profiles introduce several complications relative to the 1-D profiles due to the curvature/diameter effect discussed in a later chapter.

1. The detonation front is curved. Typically, for a diameter of 25 mm the front is close to planar in the neighborhood of the axis.

2. The detonation speed is lower than D_{CJ}. This can be seen diameter effect data, D vs 1/R where R is the radius; for 9502, see figure 9.3. Typically, $(D_{CJ} - D)/D_{CJ}$ is small for a diameter of 25 mm.

3. The sonic point moves from the end of the reaction zone into the interior. The flow behind the sonic point can become time dependent. That may serve to help identify the CJ point.

4. There is a system of ODEs in 1-D, Eq. (7.16), for the reaction zone profile with curvature. This can be used to determine the curvature effect for a specified reactive burn model. As the curvature goes to zero, the ODEs reduce to the planar ZND profile equations.

Recently, rate stick profile experiments have been done with TNT by Sollier et al. [2022, fig 3] with smaller rate sticks (15 mm diameter and length to diameter ratio of 5) than used by [Seitz et al., 1989]. The profiles with LiF windows Sollier et al. [2022, fig 3] were noisy and diverging, possibly due to some of the PDV probes being off axis and the relatively small diameter. For the winCJ velocity, the experimentalist say “we have considered the end of the first release zone as the locus of the Chapman–Jouguet (CJ) state” To this author that corresponds to the end of the fast reaction and occurs at a time of about 0.15 μs. Moreover, the CJ state should be at the change in slope of the second ‘release’ which corresponds to the end of the second slow reaction and occurs at a time between 0.6 and 1.0 μs.

Part III

Detonation Phenomena and Experiments

CHAPTER 5

Shock initiation

A detonation wave is supersonic. To initiate a detonation, at some point a shock wave must be formed, which then can be followed by a shock-to-detonation transition (SDT). Here we focus on a SDT in 1-D with the initial shock generated by the impact of a flyer plate or projectile from a gas gun on a PBX.

The following is the basic mechanism for an SDT:

1. Lead shock initiates reaction from hotspots due to pore collapse.
2. Energy release from burning increases the pressure. A pressure gradient behind shock front and the burn rate source term in the characteristic equation (2.13a) accelerates the lead shock increasing its pressure; see figure 2.2.
3. Increased shock pressure generates more hotspots and increases the burning around each hotspot, hence increases the burn rate.
4. Positive feedback between the burn rate and the shock pressure continues until the energy release saturates and a detonation wave is formed.

The increase in shock pressure with run distance is illustrated in figure 5.1. The qualitative features of $P_s(x)$ are analogous to $T(t)$ for a constant volume burn or "cook-off" experiment: an induction regime in which the shock pressure increases slowly, is followed by a runaway regime in which the shock pressure increases very fast until a detonation wave is reached. We note that the shock speed $u_s(t)$ also has the same qualitative features.

Due to the very steep slope in the runaway regime, the transition point or run-distance/run-time to detonation is not sensitive to the transition criterion; for example, it can be taken as the point at which the CJ pressure is reached or the point at which the shock speed

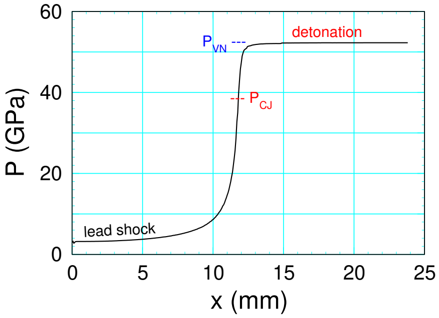

Figure 5.1: Illustrative example of the lead shock pressure versus run distance for an SDT.

is 95 percent of the CJ detonation speed or the inflection point in either the shock speed (maximum acceleration) or the shock pressure.

A key characterization of shock initiation is the run-distance to detonation as a function of initial shock pressure. This requires a series of experiments to determine the transition point as the initial shock pressure is varied. The transition point can be determined from the shock trajectory $x(t)$, since $u_s(t) = \mathsf{d}x/\mathsf{d}t$.

5.1 SDT experiments

Two types of experiments have been used to obtain the shock trajectory for a 1-D SDT. The first is the wedge experiment was introduced by Majowicz and Jacobs in 1958. It used an explosive drive system to initiate a planar shock in a wedge of HE. The second uses a gas gun to launch a flyer plate to initiate a planar shock in a cylinder of HE, and embedded magnetic gauges to get data on both the lead shock trajectory and velocity time histories behind the lead shock; see [Gustavsen et al., 2000] and reference therein for the development of magnetic gauges, and [Gustavsen et al., 1999] for use in a SDT experiment.

5.1.1 Wedge experiment

A sketch of the wedge experiment is shown in figure 5.2. A plane wave lens initiates a planar detonation in a booster HE, which drives a shock in an inert attenuator and then the test HE. The booster and attenuator are designed such that the initial shock pressure in the test HE can be varied while minimizing the pressure gradient behind the shock in the attenuator. Thus, the SDT in the test HE is driven by a sustained planar shock, which can be characterized by the initial shock pressure.

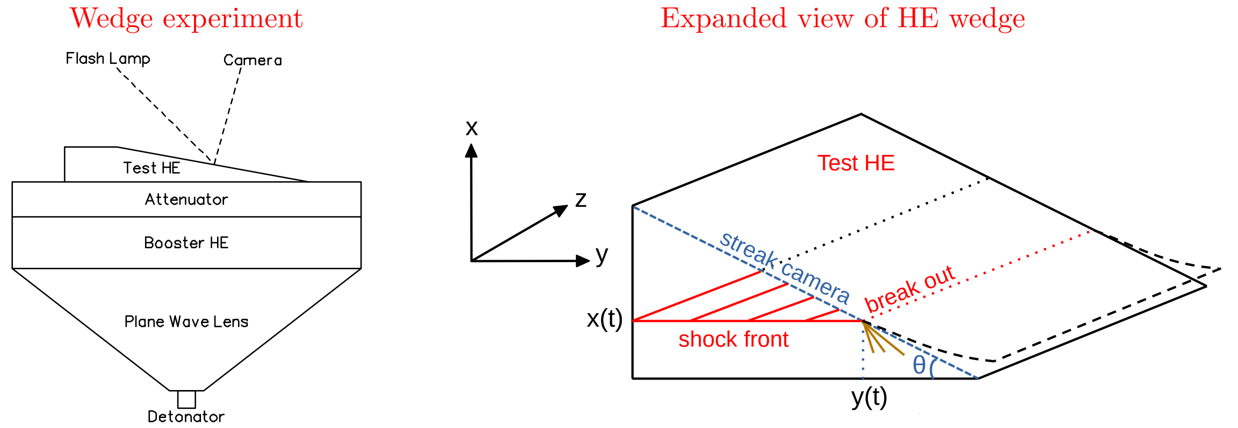

Figure 5.2: Side view of wedge experiment and expanded view of HE wedge. Streak camera measures breakout $x(t)$ along dashed blue line on top surface of center cross section of wedge.

When the wedge angle is not too large, the expanded view of the wedge shows that the phase velocity of the shock breakout on the top surface of the wedge, $u_{phase} = u_s/\sin(\theta)$, outruns the rarefaction into the wedge. Consequently, up to the breakout, $y < y(t)$, the shock front in the test HE is planar.

From shock polar analysis, the lead shock is planar if in the frame of reference in which the breakout point is at rest, the oblique shock is supersonic. This condition can be expressed as

$$(u_s - u_p)^2 + [u_s/\tan(\theta)]^2 > c^2 \ , \tag{5.1}$$

where u_s and u_p are the shock speed and particle velocity in the lab frame, and c is the sound speed behind the shock. Typically, the wedge angle θ is taken to be 30 degrees. The condition for a planar shock is then $(u_s - u_p)^2 + 3u_s^2 > c^2$. This criterion is very conservative and should easily be met.

The breakout causes a change in the intensity of the reflected light from the flash lamp (specular to diffuse reflection), which is recorded with a streak camera. In effect, the breakout determines the lead shock trajectory, $x(t)$, as if each slice of the wedge (fixed y) is an independent 1-D experiment.

In addition, the initial shock pressure for the test HE is determined as follows. Timing pins are used to determine the free surface velocity, u_{fs}, of the attenuator from a portion of its surface not covered by the wedge. Assuming the EOS of the attenuator material is known, this determines the shock velocity in the attenuator just before impact with the wedge. The initial slope of the test HE shock trajectory is the initial shock velocity in the HE, $u_s(t) = \mathsf{d}x/\mathsf{d}t$. Then the initial shock pressure is determined by a shock impedance match using $\rho_0 u_s$ as the slope of the Rayleigh line; see figure 5.3.

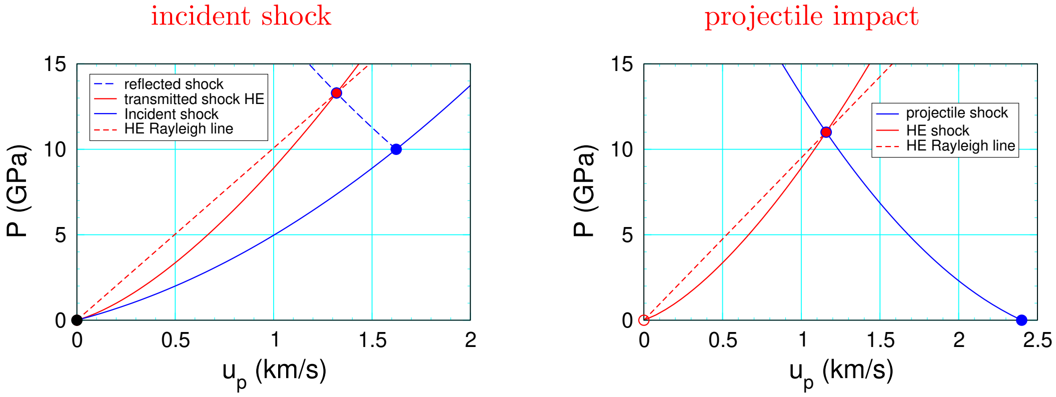

Figure 5.3: Graphical solution for shock impedance match that determines initial shock pressure. Incident shock for wedge experiment, and projectile impact for gas gun experiment.

5.1.2 SDT experiment with embedded gauges

A sketch of the gas gun target and expanded view of the gauge package is shown in figure 5.4. The gauge package consists of 3 layers; 25 μm Teflon + 5 μm aluminum + 25 μm Teflon. The Teflon is to protect the aluminum conductors, while being sufficiently thin to have small perturbation on the flow. As shown in the left figure, the aluminum conductors are arrange in a series of nested loops, one inside the next. The package is embedded in the HE at a 30 degree angle with respect to the cylindrical axis. For the experiment, a magnetic field is setup perpendicular to the cylinder axis and the active end of the conductor loops, as shown in the figure. When a planar shock passes over the loop, it is assumed that the active end of the loop (length L) rapidly equilibrates to the local particle velocity u of the surrounding HE. By Faraday's law of induction, motion of the HE leads to a voltage $= B\,L\,u$, where B is the magnetic field. Consequently, the particle velocity can be determined from the induced voltage.

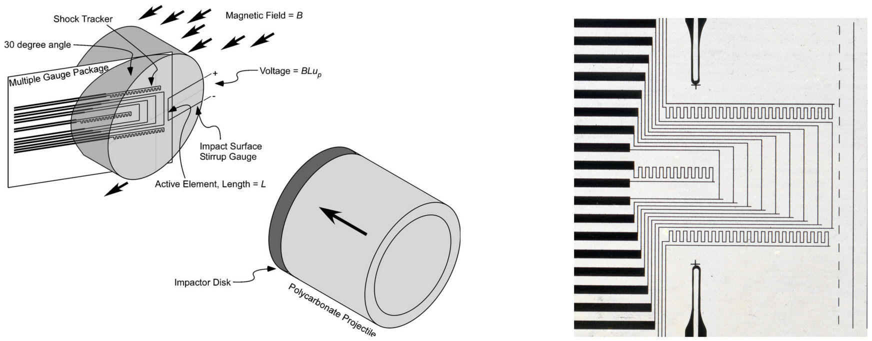

Figure 5.4: Target for gas gun experiment with embedded gauge package [Gustavsen et al., 2006, fig 1], and current pattern of conductors for 10 velocity gauges and 3 tracker gauges [Gustavsen et al., 2005, fig 3].

There are 2 types of loops: for velocity gauges in the center of the gauge package and tracker gauges which give which gives timing pulses each time the active element flips direction. As shown in the figure, there are 10 velocity gauges and 3 tracker gauges (top, center and bottom). The velocity gauges give Lagrangian time histories of the particle velocity and the tracker gauges gives data points for the lead shock trajectory analogous to the trajectory data of a wedge experiment.

Another conductor loop, called a stirrup gauge, is placed on the front surface of the HE. It is used to measure the initial particle velocity from the impact of the projectile on the target HE. The experiments also measure the velocity of the projectile just before impact. From the EOS of the projectile, the projectile velocity and the particle velocity of the HE just after impact, the impedance match is determined, see figure 5.3, and hence the initial shock pressure.

Alternatively, instead of the initial particle velocity, the impedance match can use the HE Rayleigh line with the initial shock velocity from the tracker gauges, $u_{s,0} = \mathsf{d}x/\mathsf{d}t\big(0\big)$. A third method is to use the shock jump condition, $P_{s,0} = \rho_0\, u_{p,0}\, u_{s,0}$. Comparing the value of $P_{s,0}$ from the 3 methods gives a consistency check on its accuracy.

A few additional points:

1. The initial positions of velocity gauges are 0.5 to 1 mm apart. If the run distance-to-detonation is greater than the span of the gauge positions, then the gauge package would need to be embedded downstream from the front surface of the HE in order for the transition to occur between two velocity gauges. When this is done, the center tracker, which extends the furtherest and lies on axis, determines the detonation speed for the longest time after the transition to detonation. Due to short distance of run after transition, the detonation speed may not have reached steady state.

2. The design of the gauge package gives about 4 tracker data points between adjacent pairs of velocity gauges. Thus, the gauge package gives a finer spatial resolution for the tracker gauges than for the initial positions of the velocity gauges.

3. The gauge velocity is an average over the length of the active element, which varies with the position of the velocity gauges. In addition, the effective active element of the tracker gauges is much smaller than that of the velocity gauges. Hence the tracker data points can have a jitter due to heterogeneities, which limits their precision.

4. The time for a gauge to equilibrate to the particle velocity gives a rise time of 10 to 20 ns for the lead shock. In the late stage of the SDT transition when burn rate is large, there can be some reaction in the rise time which gives a systematic error for the particle velocity behind the lead shock.

5. Teflon is a good shock impedance match for PBX 9501 and PBX 9502. This minimizes the strength of reflected waves when the lead shock interacts with gauge package, and hence perturbations to the HE flow from the embedded gauges.
6. Bdzil [2018] raised the issue for an oblique magnetic gauge of shear layers along the active gauge element leading to the particle velocities of the HE and gauge element differing. Simulations show a few percent difference in the velocities [see Menikoff, 2021b, § 5]. This would be a systematic error and would contribute to the uncertainty of the measured gauge velocity.

5.1.3 SDT data

An illustrative example of SDT data from an embedded gauge package for an experiment with PBX 9502 is shown in figure 5.5. Lagrangian time histories are along particle paths. The velocity histories show a lead shock followed by the velocity increasing to a peak and then falling off. The later profiles with initial position further downstream have a stronger lead shock and a higher peak with a steeper velocity gradient behind the front. From the characteristic Eq. (2.13a), both the burn rate and the velocity gradient contribute to accelerating the shock front.

There is a distinctive change in the time history after a detonation wave is formed. The detonation time histories have the peak velocity at the shock front and then the velocity

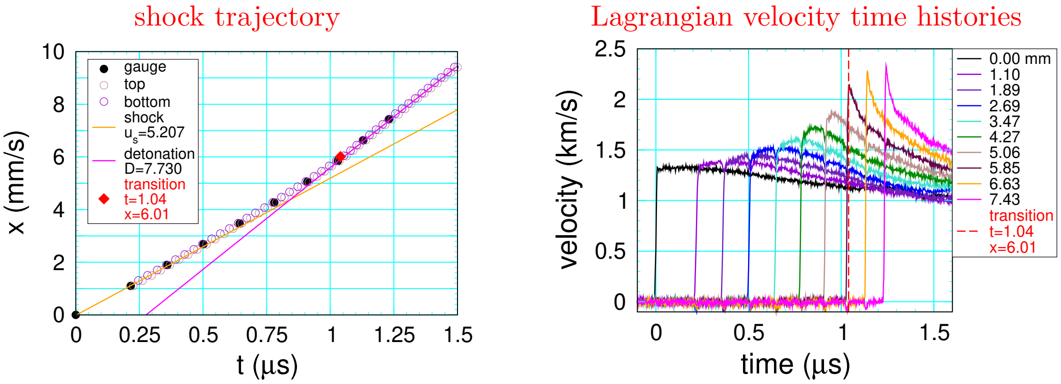

Figure 5.5: Example data from SDT experiment with embedded gauge package; [Gustavsen et al., 2006] shot # 2s-86 for PBX 9502; $x = 0$ corresponds to projectile/PBX interface and $t = 0$ to impact of projectile on PBX. For the shock trajectory plot, orange and magenta guide lines have slopes of the initial shock velocity and detonation velocity after transition, respectively. The initial positions of the velocity gauges are in the legend. $x = 0$ velocity history is from the stirrup gauge. The transition point [ibid, table II] is indicated by the red diamond on the shock trajectory plot and the vertical dashed red line on the velocity time history plot.

decreases monotonically. This is the expected detonation profile for a ZND reaction zone followed by a rarefaction wave.

Based on model EOS loci for PBX 9502 shown in figure 3.1, the VN spike and CJ particle velocities are 2.96 and 1.91 km/s, respectively. The time histories show a peak velocity larger than the CJ velocity but significantly less than the VN spike velocity. This is due to the reaction time being comparable to the gauge rise time of the lead shock, about 15 ns. The estimated reaction times from a ZND profile experiment are about 20 ns for the fast hotspot reaction and 500 ns for the slower carbon clustering reaction; see [Gustavsen et al., 2009, fig 4]. With insufficient temporal resolution, it is not surprising that the gauges clip the VN spike velocity.

The velocity gauge data can be used to calibrate some parameters of an HE burn model. In particular, the shape of the velocity profiles is related to the depletion factor; *i.e.*, the λ dependence of the burn rate.

Typically, experimentalists fit the tracker data to a smooth function, $x(t)$, and used the criterion that the transition point corresponds to the point at which shock speed is 95 percent of the detonation speed; see [Gustavsen et al., 2006, § IV.C]. As can be seen in figure 5.5 the transition point is consistent with the first velocity gauge having the distinctive profile of a detonation wave.

In addition, the gauge data and the tracker data can be combined to obtain Hugoniot data points, (u_p, u_s). Each velocity gauge gives u_p behind the lead shock front, and the smooth fit to the tracker data points determines the shock velocity at the gauge position; see [ibid, § IV.D]. There can be a large scatter in these Hugoniot data points due to uncertainty in the shock position from the shock rise time of the gauge, burning occurring in the shock rise time of the gauge, and uncertainty in the derivative of the shock trajectory for the shock speed; see [ibid, fig 9] and figure 3.1 which shows the reactants locus from an EOS model along with the data points.

For a wedge experiment, the streak camera record can be digitized. Then in an analogous manner to the shock tracker data described above, a smooth function can be fit to the $x(t)$ data points and a transition criterion applied to determine the transition point.

5.2 Pop plot

The run-distance and run-time versus shock pressure characterize the shock initiation process. On a log-log scale the data can be well approximated by a straight line. An illustrative example are the data and fits for ambient PBX 9502 shown in figure 5.6. These are known as Pop

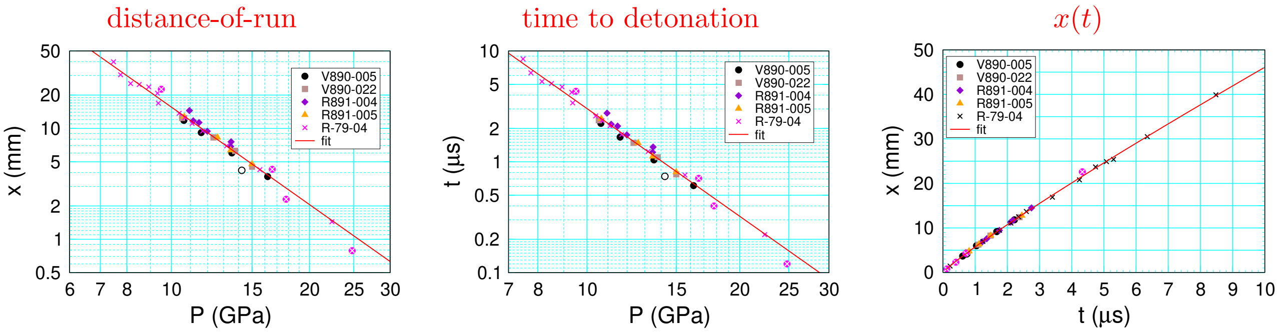
distance-of-run

time to detonation

$x(t)$

Figure 5.6: Pop plot data for ambient PBX 9502 and linear fits on log-log scale. Legend gives the PBX lot. Wedge experiments (lot R-79-04) by [Dick et al., 1988] and gas gun experiments by [Gustavsen et al., 2006]. Outliers to the fits are indicated by open symbols; 1 for lot V890-005 and 4 for lot R-79-04.

plots, named after Alphonse Popolato, who first introduced them; see [Ramsay and Popolato, 1965].

The fits for run-distance and run-time each have 2 parameters

$$\log(x/\text{mm}) = A_x - B_x \log(P/\text{GPa}) \ , \tag{5.2a}$$
$$\log(t/\mu\text{s}) = A_t - B_t \log(P/\text{GPa}) \ . \tag{5.2b}$$

The parameters are chosen to minimize the residual; *i.e.*, for run-distance

$$\text{residual} = \sum_i [\log(x_i) - \log(x_{fit}(P_i))]^2 \ . \tag{5.3}$$

To leading order in $x - x_{fit}(P)$,

$$\begin{aligned} \log(x) - \log(x_{fit}) &= \ln(x/x_{fit})/\ln(10) \\ &= \ln[1 + (x - x_{fit})/x_{fit}]/\ln(10) \\ &\approx \big[(x - x_{fit})/x_{fit}\big]/\ln(10) \ . \end{aligned}$$

Consequently, the fit corresponds to minimizing the root mean square relative error,

$$\text{rms rel error} = \left(N^{-1} \sum_{i=1}^{N} \Big[\big(x_i - x_{fit}(P_i)\big)/x_{fit}(P_i) \Big]^2 \right)^{1/2} \ , \tag{5.4}$$

and similarly for the run-time to detonation with x replaced by t.

A linear relation on a log-log plot implies a power law behavior

$$x/\text{mm} = 10^{A_x} \cdot (P/\text{GPa})^{-B_x} \ , \tag{5.5a}$$
$$t/\mu\text{s} = 10^{A_t} \cdot (P/\text{GPa})^{-B_t} \ . \tag{5.5b}$$

Furthermore, the run-distance versus the run-time is also related by a power law

$$x_*/\mathrm{mm} = 10^{A_x - A_t B_x/B_t} \cdot (t_*/\mu\mathrm{s})^{B_x/B_t} \ . \tag{5.6}$$

where the subscript '*' denotes the transition point. The power law for $x_*(t_*)$ is seen to be a good fit in figure 5.6. We note that while the power laws follow from the Pop plots, the linear form of a Pop plot on a log-log scale is an empirical relation.

Model burn rates are calibrated in part to fit the Pop plot. The calibration simulations mimic the SDT experiments. Since a projectile drives the initial shock wave, it is important that the initial shock pressure for an experimental Pop plot data point be consistent with the pressure from the impedance match of the projectile impacting the HE using the reactants EOS rather than the value of only u_p from the stirrup gauge or u_s from the derivative of the shock trajectory $x(t)$. If the transition criterion on the trajectory only depended on locally smoothing the trajectory, then the pressure for the Pop plot data point could simply be shifted to the value from the impedance match.

The Pop plot provides a way to compare the relative sensitivity to shock initiation for different HE. If the Pop plot for the first HE lies above the Pop plot for the second HE, then the first HE is less sensitive; *i.e.*, for a given pressure, the run-distance to detonation is longer for the first HE. It is possible for two Pop plots to cross. In this case one HE may be less sensitive at low shock pressures and more sensitive at high shock pressures.

5.2.1 Outliers and repeatability

The fits to the data shown in figure 5.6 exclude outliers for which the residual is greater than 2 standard deviations. The root mean square relative errors in the fits are 7.4 and 7.9 percent for the run-distance and run-time, respectively; see [Menikoff, 2018b, table 2] for details.

For Pop plot data points, there are uncertainties in both variables. The uncertainty in P can be shifted to an uncertainty in the relative error, $\Delta x/x = B\,\Delta P/P$ and similarly for t. The fits have $B = 2.920$ and 3.226 for B_x and B_t, respectively. With $B \approx 3$, a $\pm 2\,\%$ uncertainty in P implies about a $\pm 6\,\%$ relative error in x or t. Thus, the uncertainty in P can explain most of the scatter.

This is compatible with the plot of $x_*(t_*)$ having less scatter than the Pop plots for run-distance and run-time, since the curve $x_*(t)$ only uses P as a parametric parameter; *i.e.*, $(x_*, t_*) = \big(x(P), t(P)\big)$. Moreover, the power law parameters for the $x_*(t)$ are based on the Pop plot parameters. This suggests that the uncertainties in P are random, and that the fit parameters (A and B) are more accurate than the values of the individual data points.

We also note that there is a systematic difference with lot. For the Pop plot shown in figure 5.6, the 5 data points for lot V890-005 are all under the fit, while the 6 data points for lot R891-004 are all above the fit. Consequently, some of the uncertainty can be due to heterogeneities; *i.e.*, meso-scale variations in the HE sample that affect the burn rate. This motivates looking at reproducibility of experiments and outliers in more detail.

Repeatability

For all the experiments whose data is shown in figure 5.6, only two pair are near duplicates; *i.e.*, same projectile velocity. These are shots (2s-44, 2s-58), and shots (2s-40, 2s-57); see [Gustavsen et al., 2006, table II and fig 4]. All 4 experiments used lot R891-004 (violet diamond symbol in the figure) for the test sample. For the plots, the initial pressure of the first pair is 10.9 GPa, and the second pair is 13.5 GPa.

Comparisons of velocity profiles for pairs of gauges at the same location are shown in figure 5.7. For both pairs of shots, the profiles at x=0 (projectile/HE interface) are nearly the same. Hence the drive conditions for each shot in the pair are the same. For the first pair of shots, only two gauges were at corresponding positions since the gauge package for shot 2s-58 ended at too low a location. The profiles for these gauges are nearly the same. So at least the start of the SDT was reproducible.

For the second pair of shots the difference between pairs of profiles gets larger as the gauge position increases. The last pair of corresponding profiles indicate a detonation wave for shot 2s-40, while for shot 2s-57 the shock had not quiet transited to a detonation. From the tracker gauges, the transition (run-distance, run-time) were (6.88 mm, 1.22 μs) for shot 2s-40 and (7.58 mm, 1.36 μs) for shot 2s-57. The difference is (10, 11.5) percent. From figure 5.6, the lower data point (2s-40) is closer to the linear Pop plot fit. This is likely due to variations of heterogeneities affecting the burn rate.

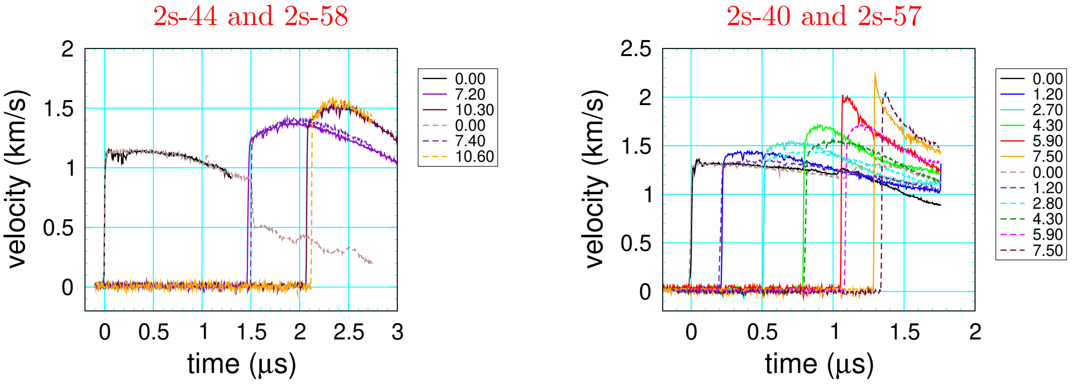
2s-44 and 2s-58

2s-40 and 2s-57

Figure 5.7: Comparison of embedded velocity gauge data for two pairs of shots, (2s-44, 2s-58) and (2s-40, 2s-57), with nearly the same initial shock pressure. Solid and dashed curves correspond to first and second shot in the pairs, respectively. The legend identifies the initial gauge locations (in mm) from the front surface of the HE. Data from [Gustavsen et al., 2006, table II and fig 4]

Outliers

Figure 5.6 shows 1 outlier for lot V890-005; open black circle at $P = 14.2\,\mathrm{GPa}$. It is instructive to compare the data for the outlier with shot 2s-86 (same lot) solid black circle at $P = 13.55\,\mathrm{GPa}$. We note that the relative error for the run-distance with respect to the fit is 24 percent for the outlier and 6.5 percent for the comparison shot. With respect to the residual for the fit this corresponds to 3.2 and 0.9 standard deviations for the data points, respectively.

The gauge data for the for the outlier and comparison shot are shown figure 5.8. For shot 2s-86, the transition run-distance is close to the location of the first gauge with a detonation profile. But for shot 2s-43, the stated transition run-distance is before the location of a gauge with a detonation profile. That is, the transition point based on the fit to the tracker data is inconsistent with the velocity gauge data. The stated transition point of 4.19 mm is too small, and based on the velocity profiles should be closer to 5.08 mm. This would change the run-distance by 17 percent, and shift the data point much closer to the Pop plot fit shown in figure 5.6.

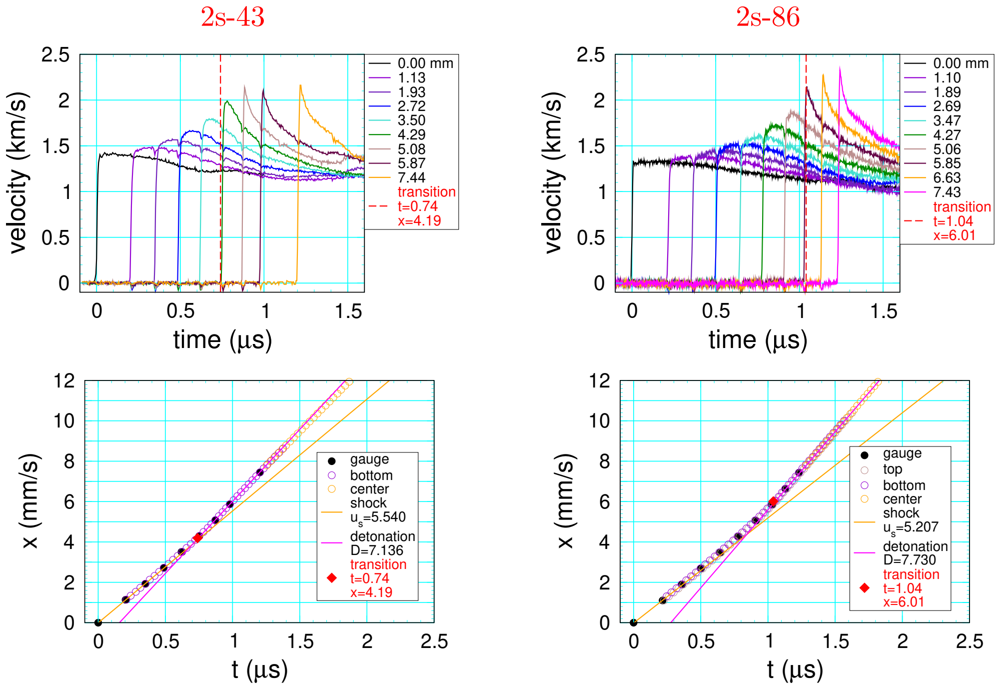
2s-43

2s-86

Figure 5.8: Gauge and tracker data for shots 2s-43 and 2s-86. The transition point is indicated by the red diamond on the shock trajectory plot and the vertical dashed red line on the velocity time history plot; see [Gustavsen et al., 2006, table II]. For the shock trajectory plots, orange and magenta guide lines have slopes of the initial shock velocity and detonation velocity after transition, respectively.

We note that there is an anomaly in the tracker data. The slope of the magenta guide line in figure 5.8 gives the detonation wave speed after the transition. For shot 2s-86, the detonation wave speed is $D = 7.73\,\mathrm{km/s}$. While for shot 2s-43, $D = 7.14\,\mathrm{km/s}$. Moreover, 6 mm after transition the detonation speed is lower, $D = 6.71\,\mathrm{km/s}$. The CJ detonation speed is $D_{cj} = 7.78$ based on extrapolating diameter effect data of Campbell [1984]. After the transition-to-detonation, we expect the detonation wave to approach steady state. But it is surprising that the difference in detonation speeds for the two shots to be so large, and for 2s-43 the detonation speed to be low and decreasing. This may have affected the fit to the shock trajectory and the transition criterion.

It is instructive to examine the shock velocity based on simple finite differences of adjacent tracker gauge data points. A comparison of $u_s(x)$ for the two shots is shown in figure 5.9. Since the precision of the data is about 3 digits and the finite difference derivatives have round-off errors, u_s is noisy. Nevertheless, the shock velocity changes abruptly in a transition interval (shaded region in figure) with a width of about 1.5 mm. For shot 2s-86, the transition point is towards the high end (larger x) of the interval. In contrast, for shot 2s-43, the stated transition point is near the beginning (smaller x) of the interval. The transition point based on the velocity gauge profiles is toward the end of the interval, which is consistent with shot 2s-86.

Basing the transition point on a well defined criterion for a smooth fit of $x(t)$ is aimed at attaining higher accuracy and an objective means to determine the transition point. While this works most of the time, shot 2s-43 shows that it may break down for outliers. Outliers may also be due to variations in heterogeneities among HE samples, which would affect the burn rate. The latter case would imply an inherent limit on the accuracy of the Pop plot.

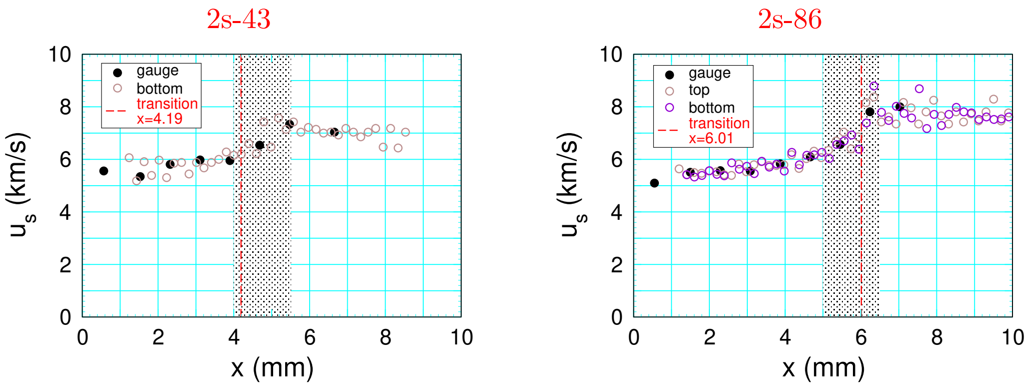

Figure 5.9: Shock speed versus run-distance for shots 2s-43 and 2s-86 from finite differences of tracker gauge data. Transition run-distance from [Gustavsen et al., 2006, table II] is indicated by the vertical dashed red line. Shaded region indicates transition interval over which shock speed changes rapidly.

5.2.2 Pressure range for Pop plot

Pop plot data has a limited pressure range. For high initial shock pressure, the initial burn rate is large and the run-distance to detonation is small. The burning increases the uncertainty in determining the initial shock pressure, and decreases the number of $x(t)$ data points up to transition, which greatly increases the uncertainty in determining the transition point. Moreover, starting with a high burn rate skips the induction regime of a SDT shown in figure 5.1. This affects the interpretation and hence criterion for determining the transition point. For PBX 9502, figure 5.6 shows that the highest pressure Pop plot data point at 25 GPa, which is 10 percent less than $P_{cj} = 28\,\text{GPa}$, is an outlier on the low side.

For low initial pressure, the low rate leads to a long induction and a large run-distance to detonation. To avoid side rarefaction from affecting the 1-D flow in the neighborhood of the diagnostics, the width of a HE wedge or diameter of a HE cylinder needs to be at least twice the run-distance at transition. For the wedge experiments with PBX 9502 the plane wave lens could support a 100 mm diameter flyer plate, and hence run-distances up to 50 mm. For the gas gun experiments, the projectile diameter is limited to the bore of the gas gun which is 50 mm, and hence run-distance of up to 25 mm. The off-axis position of the gauge package conductors, see figure 5.4, would further limit the run-distance.

There were experiments by [Vandersall et al., 2010] out to run-distances of 80 mm using a 155 mm Howitzer to drive a projectile. For HMX based PBXs, Pop plots extended to initial pressures of 1 to 2 GPa are shown in figure 5.10. It can be seen that the linear Pop plot fit on a log-log scale breaks down at low pressures. The greater run-distances at low pressures implies a lower burn rate; *i.e.*, shock driven pore collapse is not as effective at generating hotspots below a threshold pressure of 1.5 to 2 GPa. As discussed below this is due to elastic-plastic effects resulting in a non-zero shock rise time.

Magnetic gauge experiments with PBX 9501 show that at low pressures the shock front is dispersed; *i.e.*, a shock has a profile with a non-zero rise time [see, Dick et al., 1988, figs 6–9].

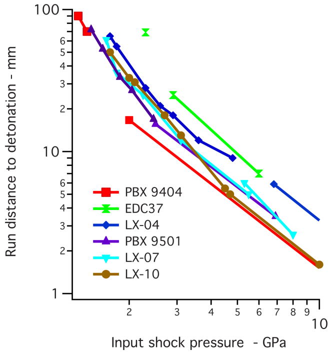

Figure 5.10: Pop plots for HMX based PBXs from Vandersall et al. [2010, fig 15].

The shock rise time decreases with shock pressure from about 1 μs at pressure of 0.3 GPa to 0.5 μs at 0.56 GPa, to a partly partly dispersed profile (discontinuous shock followed by smooth rise to final shock state) at 1.2 GPa. This is similar to a diffuse shock profile based on equilibrium and frozen shock loci discussed by Fickett and Davis [1979, see figs 4.3 and 4.4] for reactive flow with an endothermic reaction. In this case, the shock entropy comes from the reaction, while for PBX 9501 the reaction rate is small at low pressure and the shock entropy comes in part from plastic flow.

For PBX pores with a diameter of a few microns or less, at pressures below a GPa, the implosion time is a few ns or less. If the shock rise time is comparable to the implosion time, then effectively the implosion occurs in the shock rise and is driven by a pressure lower than the shock pressure. This would lead to weaker hotspots.

5.2.3 Pop plot variations

For a given HE, the Pop plot varies with initial temperature, initial density and lot. Data for PBX 9502 and PBX 9501 illustrate the magnitude of these variations.

The temperature range for applications is from -55 C to 75 C. Figure 5.12 shows the variation of the PBX 9502 Pop plots for several temperatures. The Pop plot parameters A and B for each temperature are given in [Menikoff, 2018a, table 1].

The general trend is that the Pop plot shifts down as the temperature increases. This implies shock sensitivity increases with temperature. The increase in sensitivity correlates with decrease in density due to thermal expansion and presumably an increase in porosity.

The temperature variation plot also shows data for different lots. The cold Pop plot (-55 C) has the largest variation with lot. Figure 5.11 shows the data and fit for each lot. The Pop plot parameters A and B for fit to each lot are given in [Menikoff, 2018a, table 3]. The relative

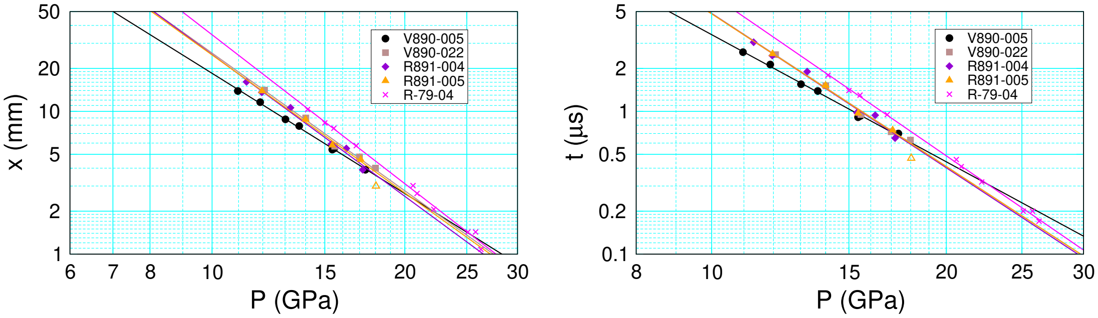

Figure 5.11: Pop plot for cold (-55 C) PBX 9502. Data from [Gustavsen et al., 2012].

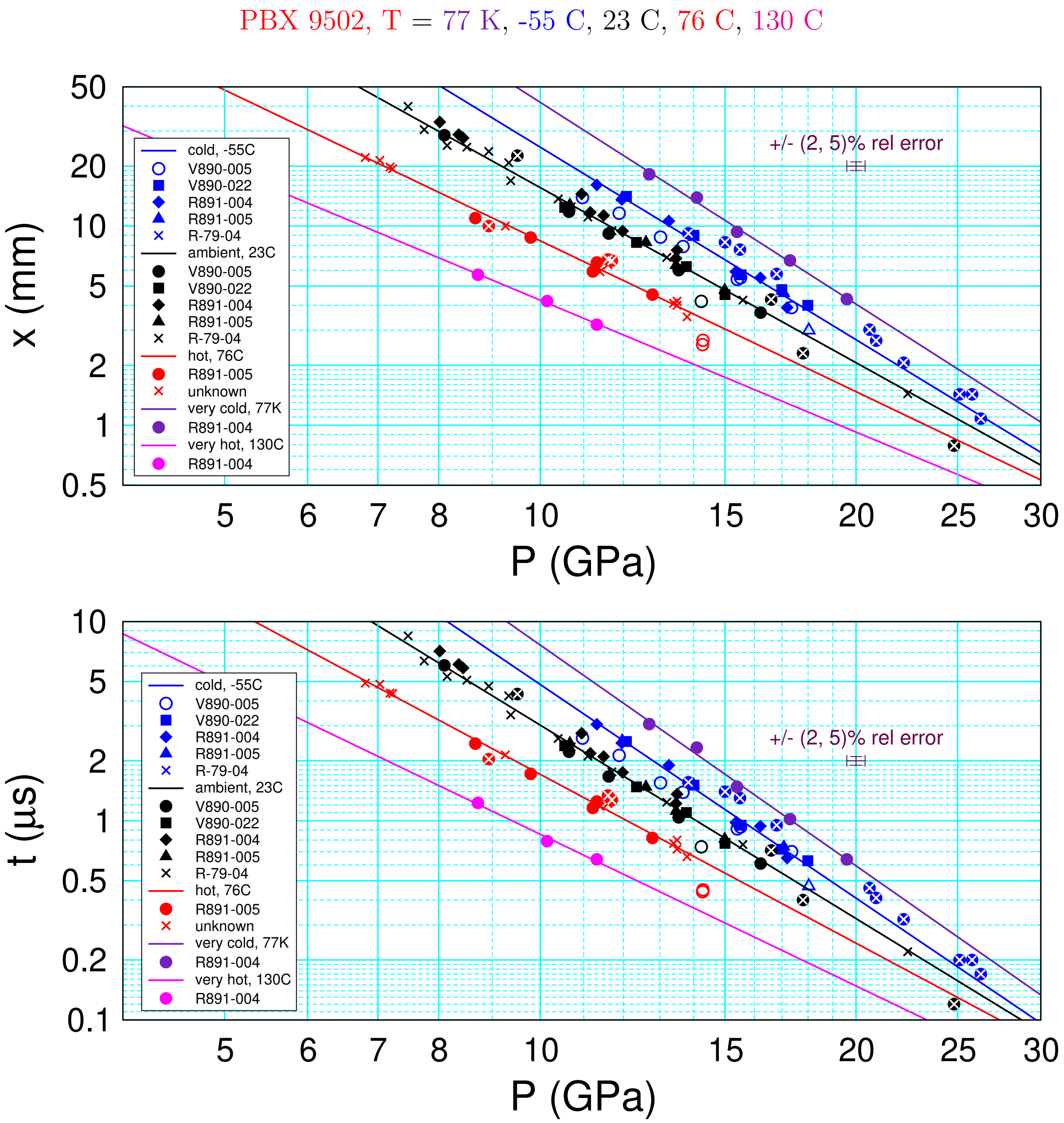

Figure 5.12: PBX 9502 Pop plot variation with temperature: at -196 C (77 K) [Hollowell et al., 2014], at -55 C [Dallman and Wackerle, 1993, Gustavsen et al., 2012], at 23 C [Dick et al., 1988, Gustavsen et al., 2006], at 76 C [Dallman and Wackerle, 1993, Gustavsen et al., 2017b] and at 130 C [Gustavsen et al., 2018b]. Error bar is meant only as a guide.

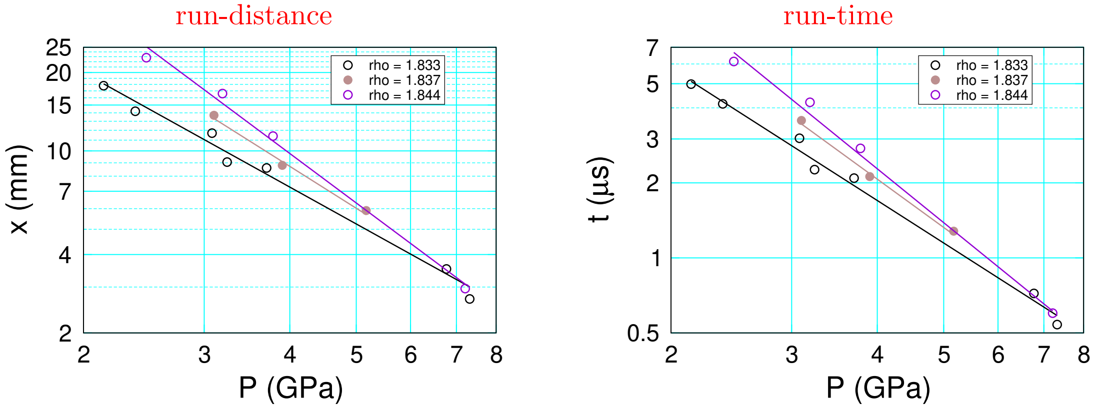

Figure 5.13: PBX 9501 Pop plots for three initial densities. Data from [Gustavsen et al., 1999, fig 12].

error for fitting all 5 lots is 11.1 percent. But it drops to 5.5 percent when the extreme lots (V890-005 and R-79-04) are excluded. We also note that the variations among the lots are correlated for both run-distance and run-time.

For the density variation, there is also data for PBX 9501. The ambient Pop plots are shown in figure 5.13 for three initial densities: 1.833, 1.837 and 1.844 g/cc. The density variation is small, ± 5 mg/cc or ± 0.3 percent, but the difference in run-distance and run-time is large. At 3 GPa, the run-distance varies from 11 to 17 mm or ± 40 percent, and the run-time varies from 2.8 to 4.3 μs or ±42 percent. The reason for the sensitivity is that the burn rate depends on hotspots from pore collapse. Because the porosity is small, a small change in density gives rise to a large change in porosity. Without porosity, the density (TMD) is estimated to be 1.860 g/cc. Hence, the porosity varies from 0.0086 to 0.0145 or ± 50 percent.

For a given HE, reactive burn models are typically calibrated to the Pop plot at the specified initial density and initial temperature. The variation of the Pop plot with lot would then limit the accuracy for shock initiation. For other initial densities and initial temperatures the burn rate would need to be recalibrated. Effectively, this is treating an HE at different initial conditions as a new distinct explosive. It is especially important for the large effect initial temperature has on shock initiation.

5.3 Complex shock loading

The Pop plot is based on shock ignition driven by a sustained planar shock. It is simple and well suited to calibrating a model burn rate. However, fitting Pop plot data does not guarantee a reactive burn model would match ignition data for more complex shock loading conditions.

Example of other loading condition are listed below.

1. Short shock.
   This refers to the case when a planar shock is sustained for less than the 1-D run-time to detonation. The condition can be set up experimentally on a gas gun with a thin projectile impacting a sample HE and diagnosed with an embedded gauge package. A short shock is an idealization of an inert fragment impacting an HE. The key issue is whether or not the impact leads to a detonation or the reaction is quenched by subsequent rarefactions from behind.

2. Shock followed by rarefaction.
   This occurs in the gap test; see for example [Gibbs and Popolato, 1980, § 4.2]. It consists of a detonation wave in a specified donor HE impacting an inert gap material followed by an acceptor (test) HE. The rarefaction is from the Taylor wave in the donor HE. For a thicker gap, the lead shock has a lower pressure and the rarefaction has a lower pressure gradient. It is used to test the relative sensitivity of HEs. An HE is more sensitive if the donor HE detonates with a thicker gap.

3. Multiple shocks.
   Experiments with a sequence of 2 planar shock waves impacting an HE can be set up experimentally on a gas gun using a layered projectile with a low impedance material followed by a high impedance material. The lead shock can desensitize the HE and affect the subsequent burn rate. A weak transverse shock can quench a propagating detonation wave. Shock desensitization is discussed in more detail in the next subsection.

4. Shock initiation with a divergent lead shock.
   A diverging lead shock occurs for initiation of a booster HE from a detonator. A test version of a detonator/booster with diagnostics for the breakout of the detonation wave on the booster surface is the onionskin test; see for example [Francois et al., 2014].

5.3.1 Shock desensitization

Shock desensitization is the phenomenon in which the first shock limits the amount by which later shocks can increase the burn rate. It implies that the burn rate is not strictly a function of only the local thermodynamic state but also depends on the time history. Campbell and Travis [1986, fig 5 and table 4] noted that a single crystal of HMX is very shock insensitive. It could not be initiated by a detonation wave in PBX 9404, which is 94 wt percent HMX and has a CJ pressure of 35 GPa. Moreover, a sustained shock at 35 GPa did not initiate a single HMX crystal within the 7 mm length of the crystal. Whereas the Pop plot for PBX 9501 (95 wt percent HMX with CJ pressure of 35 GPa) shown in figure 5.13, has a run-distance of less than 3 mm at 7 GPa.

Assuming the burn rate is due to hotspots from pore collapse, Campbell and Travis [1986] interpreted shock desensitization as being due to the first shock collapsing the pores without igniting them, which would remove potential hotspot sites for subsequent shock waves. Next we discuss additional experiments that clearly show shock desensitization.

Two planar shocks

As noted previously, a layered projectile from a gas gun can generate 2 shocks in an HE. A series of 3 double shock experiments with PBX 9502 were performed by [Aslam et al., 2011] and diagnosed with a VISAR probe at the back surface of PBX 9502. The two shock pressures and the velocity time history for each shot are shown in Figure 5.14.

The velocity time histories show plateaus after each of the two shocks. The second plateau is followed by weak compressive waves due to wave reflections off the interfaces of the projectile layers. The reflected waves are a complication and end the useful range of the velocity data. The slopes of the plateaus are very small and imply that the burn rates are small. For comparison, the run-times to detonation for the first shock ($P_1 \leq 9$ GPa) from the Pop plot, figure 5.6, are greater than $4\,\mu$s. Hence, the burn rate is small, and for a few tenths of μs before the second shock overtakes the first, the velocity is nearly constant.

For the second shocks, the run-times to detonation from the Pop plot are 0.4, 0.16 and $< 0.1\,\mu$s at pressures of 19, 25 and 33 GPa, respectively. The plateau after the second shock implies that the burn rate changed very little. Thus, the first shock desensitized the PBX.

Additional double shock experiments were carried out by Gustavsen et al. [2018a]. For PBX 9501 they found that a weak shock, 1.4 to 1.6 GPa, followed by a stronger shock, > 7.5 GPa, leads to partial desensitization; lower reaction rate behind second shock than would occur from the second shock alone. We note that the weak shocks had a noticeable rise time, which is in agreement with previous study of low pressure (less than 2 GPa) PBX 9501 shocks by Dick et al. [1998]. This likely is due to plastic deformation in the neighborhood of contact

Double shock PBX 9502

	P_1	P_2
shot	GPa	GPa
2s-450	5.3	19
2s-463	7.0	25
2s-465	9.0	33

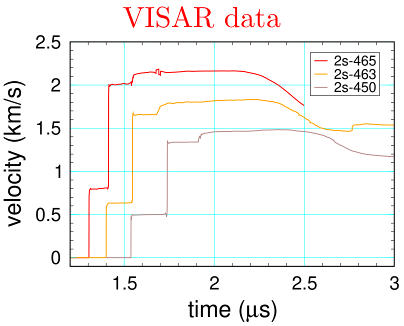

Figure 5.14: Double shock experiment data [Aslam et al., 2011].

points between large grains, and reminiscent of compaction waves in granular explosives; see for example [Menikoff and Kober, 2000a] and [Menikoff and Kober, 1999, § 7]. In terms of hotspots from pore collapse, assuming the binder is soft (lower bulk modulus) compared to the HE crystals, the large grains may provide a hoop stress 'cage' that shields small pores from collapse. Then, the additional more uniform deformation from the second stronger shock would break the cage and collapse the remaining pores generating more hotspots and increasing the burn rate.

Quenching a propagating detonation wave

Figure 5.15 shows a sketch for Phermex shot # 1697. A slab of PBX 9502 is detonated at the bottom with a plane wave lens. Another HE (datasheet) launches a steel plate that impacts the side surface of the PBX simultaneously and drives a transverse shock with pressure of about 6 GPa into the PBX; *i.e.*, normal to the direction of the detonation wave.

The dynamic radiograph shows the detonation wave front and transverse shock interacting to give a shock and contact at about the end of the PBX slab. Moreover, the angle of the contact indicates that the width of the detonation front shrinks as it propagated. Consequently, the weak transverse shock is quenching the propagating detonation wave.

A PBX is not fully desensitized when the first shock is not supported. An example in 1-D is

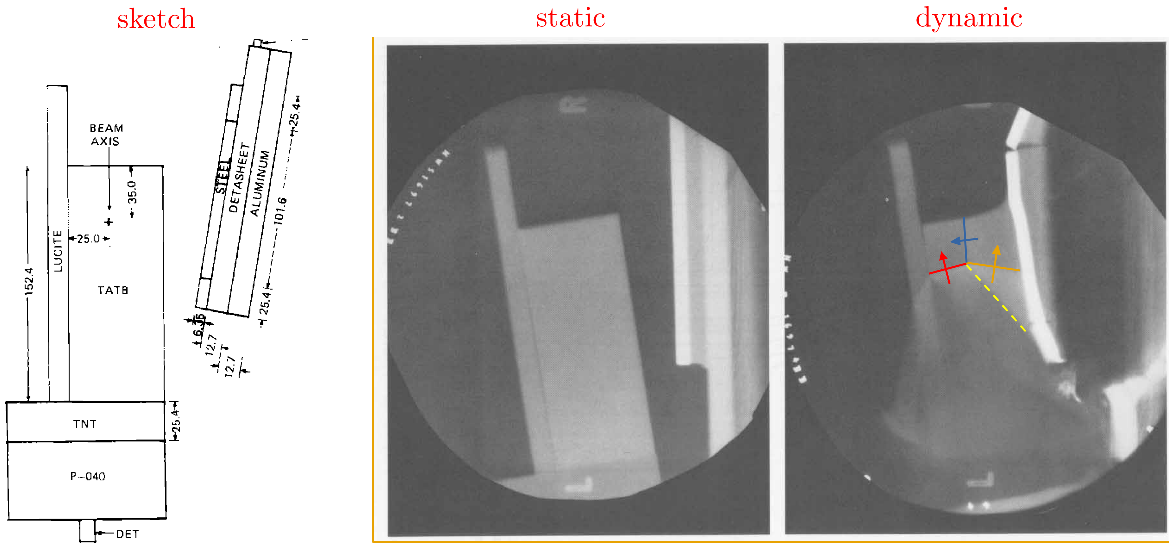

Figure 5.15: Sketch of Phermex shot # 1697 along side static and dynamic radiographs from [Mader, 1979, pp 414-415]. In the dynamic, red line is the detonation front, blue line is the transverse shock, orange line is shock in precompressed PBX and dashed yellow line is contact. Arrows indicate the direction of shock propagation.

for a shock into a PBX followed by a release wave and then re-shocked [Aslam et al., 2018]. In 2-D, an example is a variation of the detonation quench experiment in which the transverse wave is from a thin layer of datasheet directly along the side of PBX 9502, see [Handley et al., 2019]. The detasheet generated a weak transverse shock followed by a rarefaction. The experiment showed that the detonation wave is not quenched. Currently, the partial desensitization by a second shock is not understood.

5.4 Initiating a detonation wave

For some simulations, it is useful to promptly initiate a detonation wave. One way to do this is with a booster HE initiated with a programmed burn model; see section 3.5. The detonation wave in the booster will drive a shock wave in the surrounding HE. If the booster is large enough, then a shock-to-detonation transition would detonate the surrounding HE.

A simpler way to initiate an HE is with a macroscopic 'hotspot'; *i.e.*, a few mm size hotspot (rather than a micron size hotspot which occurs on the mesoscale). The hotspot can be initialized with the HE products at the CJ states, and hence a high pressure. In analogy with the booster, the high pressure of the hotspot drives a shock wave into the HE surrounding the hotspot and triggers a shock-to-detonation transition. The HE can be initiated faster and the hotspot can be a smaller size if the initial hotspot region is also set with the CJ particle velocity directed normal to the hotspot surface. This is due to the larger shock pressure from the impedance match, as seen in figure 5.16.

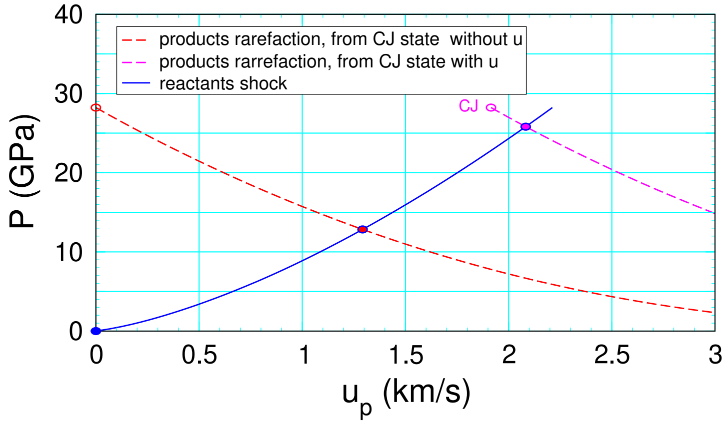

Figure 5.16: Impedance match for initiating detonation wave with a macroscopic hotspot at the CJ pressure with and without the CJ particle velocity. The match pressure in the reactants then drives a shock-to-detonation transition.

CHAPTER 6

Ignition and growth concept of hotspots

The idea that hotspots are important for initiating of a detonation wave started with experiments on friction, shear heating and low velocity impact; see [Bowden and Yuffee, 1952] and references therein. Then an extensive series of experiments by Campbell et al. [1961a] extended the hotspot idea to shock initiation of a heterogeneous explosive.

At the end of the introduction, it was asserted that hotspots generated by pore collapse dominate the burn rate. Here we discuss data from shock initiation experiments that support the assertion. This leads to the *ignition and growth concept* of hotspots introduced by Lee and Tarver [1980]. The concept can be used to motivate the form of a sub-grid burn rate for a homogenized reactive burn model.

6.1 Data supporting hotspot burn rate

Three types of data support the claim that a shock-to-detonation transition (SDT) is due to hotspots:

1. Time-to-detonation of SDT experiments.
   The chemical reaction rate at the shock temperature of the bulk material is orders of magnitude too small for the measured time-to-detonation of a SDT experiment. In contrast to other dissipative mechanisms, such as plastic work or shear heating that generate fairly small increases in temperature, pore collapse can generate large increases in temperature. This is discussed in the next subsection, 6.1.1.
2. Shock desensitization.
   The following examples imply that without porosity or if the potential for hotspots is limited by squeezing out pores (shock desensitization) then the burn rate is low:

   i. Single crystal HMX with little porosity is very insensitive compared to HMX based PBX 9501 which has about 1.5 percent porosity.
   ii. Double shock initiation data shows that the burn rate is limited by the first shock.
   iii. Quenching of a propagating detonation wave by a weak transverse shock also shows that the burn rate is limited by the first shock.
   iv. Distance-to-detonation for SDT experiments is very sensitive to porosity.

   This phenomena has been described previously in subsection 5.3.1.

3. Homogeneous versus heterogeneous shock initiation.
   Qualitatively different SDT velocity time histories for homogeneous and heterogeneous HE implies different burn mechanisms. Homogeneous explosives (gases and liquids) are modeled well with chemical reaction rates that depend on temperature. Empirical burn rates for heterogeneous explosives (PBXs) that fit experimental data, are better fit to pressure rather than temperature. This is discussed in subsection 6.1.2.

6.1.1 Chemical reaction rate

We use the HMX based PBX 9501 as an illustrative example since both SDT data and chemical reaction rate data are available. Its Pop plot is shown in figure 5.13. The data covers the initial shock pressure range from roughly 2 to 8 GPa. Over this range, the time-to-detonation varies from 7 to 0.5 μs. Utilizing the heat capacity based on the phonon spectrum (see for example [Menikoff, 2014b] and references therein) of HMX, the shock temperature is shown in figure 6.1. The shock temperature corresponding to the Pop plot data is less than the HMX melt temperature at 1 bar. Pyrolysis test data shows that very little reaction occurs below the melt temperature (550 K at 1 bar); [Gibbs and Popolato, 1980, p 113, fig 1].

Also shown in figure 6.1 is the “global” fit of Henson et al. [2002] to HMX ignition-time data on an Arrhenius plot (log time vs 1/T). Below the melt temperature, the experimental ignition time is greater than 2000 seconds. This is orders of magnitude longer than the Pop plot time-to-detonation. Consequently, the μs time scale for shock initiation of PBX 9501 is not the result of a chemical reaction rate at the shock temperature.

Instead a localized hotspot burn rate is needed. Moreover, the velocity gauge data for SDT experiments show evidence that imply at least some hotspots thermally runaway and generate reactive wavelets (burn centers) on a sub μs time scale. The early time history from the first two gauges of shots 1s-1147 and 1s-1145 illustrate this and are shown in figure 6.2.

The first two gauges of shot (1s-1145) with initial shock pressure of 5.17 GPa show that the velocity is nearly constant up to a time of about 0.3 μs. Then the velocities start to deviate;

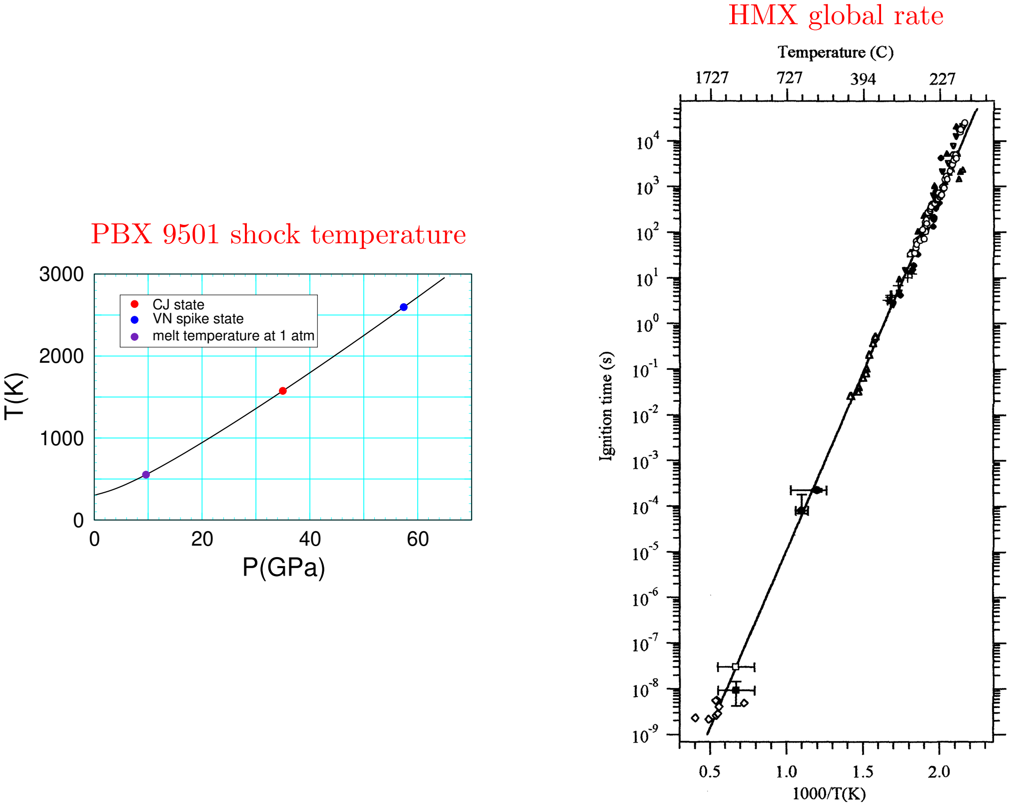
PBX 9501 shock temperature

HMX global rate

Figure 6.1: PBX 9501 shock temperature and ignition time for the HMX "global rate" of Henson et al. [2002, see fig 1 and caption for symbol references]. The Arrhenius fit to ignition time is $A^{-1} \times \exp(T_a/T)$ where $A = 5.6e12/\mathrm{s}$ and $T_a = 17.9\mathrm{e}3\,\mathrm{K}$.

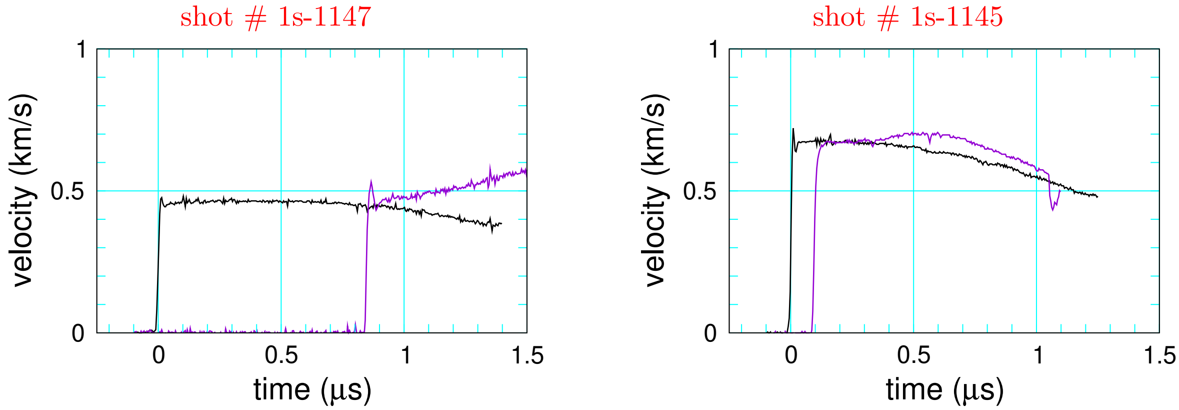
shot # 1s-1147

shot # 1s-1145

Figure 6.2: First two velocity gauges for SDT experiments with PBX 9501 by Gustavsen et al. [1999]. Shot 1s-1147 had initial shock pressure of 3.10 GPa and left plot shows gauges at interface (x=0) and x=3.01 mm. Shot 1s-1145 had initial shock pressure of 5.17 GPa and right plot shows gauges at x=0 and x=0.43 mm.

decreasing for the first gauge and increasing for the second gauge. The change in velocity of the first gauge is due to reaction increasing the pressure. This creates a pressure gradient which causes the velocity on the second gauge to increase. Therefore, we can conclude that negligible reaction occurs before $t = 0.3\,\mu$s. This can be explained by thermal runaway of some hotspots that then trigger reactive wavelets at $0.3\,\mu$s after the arrival of the lead shock. Thereafter, the burn rate is dominated by a reactive wavelet. For this case, the shock arrives at the second gauge at $0.1\,\mu$s, and burning along the second gauge would start at $0.4\,\mu$s.

The first gauge of shot (1s-1147) also shows that the interface velocity is initially constant. Since the initial shock pressure is lower than that of the previous shot, 0.310 versus 5.17 GPa, the hotspot thermal runaway time increases to 0.7 versus $0.3\,\mu$s. In this case, the reaction on the second gauge would begin $0.65\,\mu$s after shock arrival time of $0.85\,\mu$s or $1.5\,\mu$s.

This illustrates that the thermal runaway time of hotspots increases with decreasing shock strength. Conversely, the hotspot runaway time decreases with increasing shock strength. For 1-D SDT experiment, the lead shock strength increases with distance of run. Hence, the thermal runaway time will decrease with distance of run. Moreover, if the initial shock is sufficiently strong then the hotspot runaway time becomes negligible for all the velocity gauges.

An important issue for hotspots is their size, temperature and thermal runaway reaction time. Tarver et al. [1996] called these critical conditions. Their estimate is based on the competition between the heat release from the chemical reaction rate (which raises the temperature) and heat conduction (which lowers the temperature). They assumed constant volume burn starting with a high temperature region (1-D slab, cylinder or sphere of HE) to represent a hotspot and a boundary temperature. The chemical reaction model used the reaction energies and heat capacities for the temperature, along with the 3-step McGuire and Tarver [1981] reaction model calibrated to data for one-dimensional time to explosion (ODTX) experiments. Numerical simulations of the reactive diffusion equation were used to determine for HMX both the critical temperature and the time to explosion as a function of hotspot diameter; see [Tarver et al., 1996, fig 5 and 6].

From their figures, a 1μs runaway time required a hotspot temperature of 1000 K, and a hotspot diameter of $2\,\mu$m. A shorter explosion time would require higher temperatures and smaller diameter. For example a $0.1\,\mu$ explosion time would require a diameter of $0.4\,\mu$m and temperature of 1100 K. We note that the hotspot diameter is compatible with pore size distribution discussed in subsection 1.3.2.

In contrast to the ignition time at constant volume, pore collapse is dynamic and reaction can occur during the late stage of collapse and subsequent outward rebound. Consequently, ignition time from figure 6.1 is only approximate for pore collapse. The needed hotspot temperature to trigger burn centers for PBX 9501 is likely up to 1200 K at the low pressure end of Pop plot data range, and over 2000 K at the high end of the Pop plot data.

6.1.2 Homogeneous vs Heterogeneous shock initiation

SDT experiments have been performed for both heterogeneous solid explosives [Campbell et al., 1961a] and homogeneous liquid explosives [Campbell et al., 1961b]. For additional SDT experiments using embedded velocity gauges see subsection 5.1.3 for heterogeneous explosives, and [Sheffield et al., 1989] and references therein for homogeneous explosives. As can be seen in the (x,t) wave diagrams, figure 6.3, and the velocity profiles, figures 6.4 and 6.5, SDT for heterogeneous and homogeneous explosives are qualitatively different.

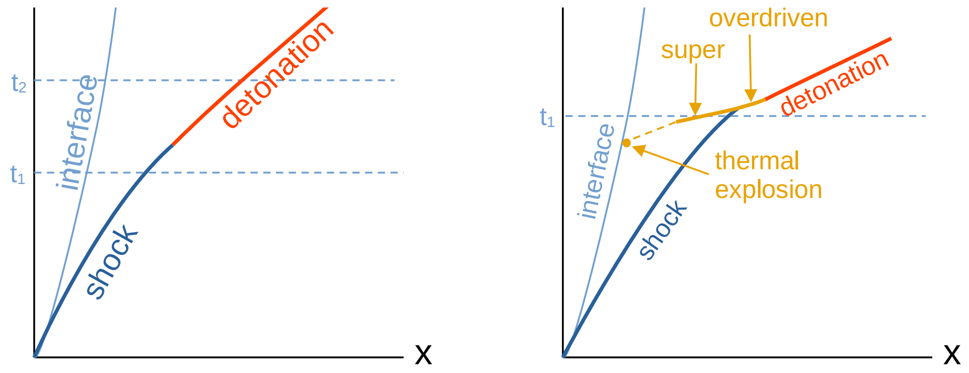

heterogeneous SDT

homogeneous SDT

Figure 6.3: Wave diagrams in (x,t)–plane of heterogeneous and homogeneous SDT.

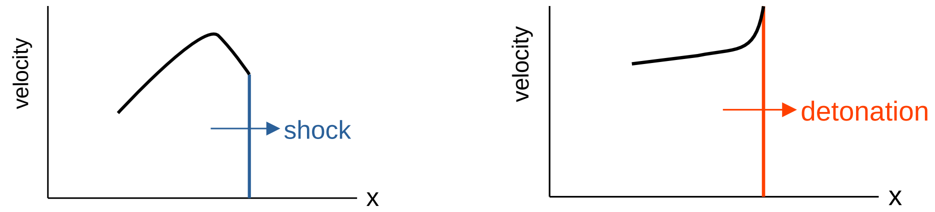

heterogeneous SDT time t_1

heterogeneous SDT time t_2

Figure 6.4: Lagrangian particle velocity profiles at selected times for heterogeneous SDT.

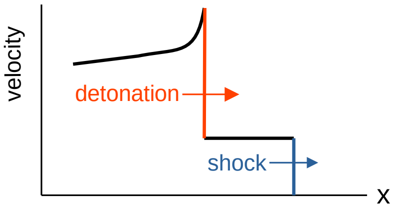

Figure 6.5: Lagrangian particle velocity profile for homogeneous SDT at time t_1 when super detonation occurs.

For the heterogeneous case, the lead shock strength increases and builds up to a detonation wave. In contrast, for the homogeneous case, thermal runaway occurs near the HE interface resulting in a reactive wave in the shocked explosive. Subsequently, the detonation wave overtakes the lead shock resulting in an overdriven detonation wave in the ambient explosive, which then decays to an underdriven detonation wave.

The detonation wave in the pre-shocked explosive is often referred to as a "super-detonation." Because the ahead state has a higher density and hence a higher energy release per volume, the super-detonation has a larger detonation speed and a much higher shock pressure than a detonation wave in the ambient explosive.

As an illustrative example, the shock and detonation loci in the (V, P)–plane for the normal detonation wave and super-detonation wave in nitromethane are shown in figure 6.6. A pre-shock of 9.2 GPa increases the density by a factor of 1.66 . This results in a large increase in the CJ detonation pressure, from 11.1 to 38.4 GPa, and CJ detonation speed, from 6.25 to 9.23 km/s.

From a mathematical point of view, homogenized models are used for both solid and liquid explosives. The burn rate can be calibrated such that simulations can match SDT experiments for either case shown in figure 6.3. Consequently, the difference between homogeneous and heterogeneous explosive models is the fitting form used to calibrate the burn rate; a temperature dependent Arrhenius form $(A \exp(-T_a/T))$ for a homogeneous liquid or gaseous

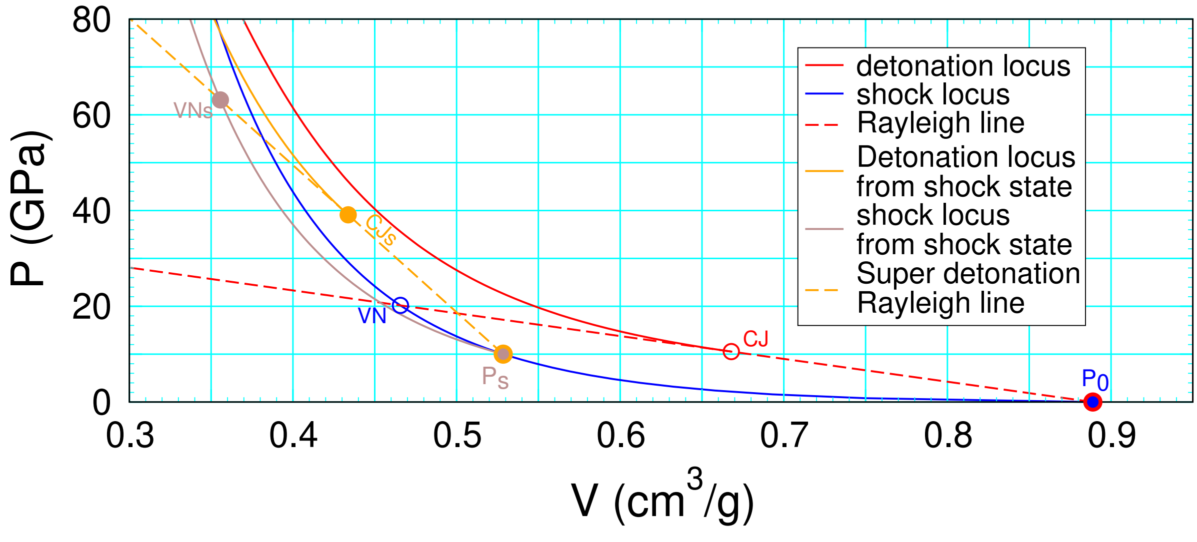

Figure 6.6: Detonation loci for nitromethane with ambient ahead state and for "super-detonation" in pre-shocked explosive. Blue and red curves are the shock and detonation loci, respectively, for initial state P_0 with ahead state at rest. Brown and orange curves are the shock and detonation loci, respectively, for pre-shocked state P_s.

explosive, and a pressure dependent fitting form (such as P^n) for a heterogeneous solid explosive. The fitting forms also are compatible with instabilities observed for homogeneous gaseous explosives; see Fickett and Davis [1979] section 6C for galloping instability in 1-D and chapter 7 for a transverse wave instability in 2-D.

We also note that by adding glass beads or micro-balloons, the qualitative features of a SDT changes from homogeneous to heterogeneous [Dattelbaum et al., 2010]. In addition, adding air bubbles to a liquid explosive, such as nitroglycerin, has a similar effect on sensitizing shock initiation as adding porosity to a PBX.

6.2 Ignition & Growth concept

The previous section motivated the need for a burn rate based on hotspots generated by pore collapse in order to explain the qualitative features of shock initiation in a heterogeneous solid explosive. On the meso-scale level, the physical steps for a shock driven hotspot burn rate are described by the *Ignition & Growth concept* introduced by Lee and Tarver [1980]. These steps are outlined in table 6.1; henceforth denoted IG.1, $\cdots$, IG.4 .

When the reactive-profile width of a wavelet, shown in steps IG.3 and IG.4, is less than the radius of curvature of the wavelet front, the wavelet corresponds to an expanding deflagration wave[1]. Based on the detonation and deflagration loci shown in figure 1.2, the deflagration speed is much less than the detonation speed. This is a general property since, with respect to the flow ahead, a detonation wave is supersonic while a deflagration wave is subsonic.

For propellants, most of the heat release occurs in the gas phase. Thermal conduction back to the solid surface, needed to vaporize the surface and generate the gas, depends on the pressure. The deflagration speed has been measured and found to be proportional to P^n with $n \sim 1$. The pressure dependence has been extended to condensed phases and higher pressures using a diamond anvil cell. We note that the diamond anvil cell measurements are a lower bound for the deflagration speed since the explosive surrounding the hotspot is at room temperature, whereas for an ignition and growth hotspot the surrounding explosive is at the shock temperature.

For HMX, measurements went up to the CJ pressure [Zaug et al., 2009, fig 4]. The deflagration speed ranges from 10 m/s at 2 GPa up to a few 100 m/s at the CJ pressure of 35 GPa, with ambient temperature ahead of the wave. Compared to the CJ detonation speed for PBX 9501 (8.8 km/s), the deflagration speed at the low end of the Pop plot data (2 GPa) is estimated to be 3 orders of magnitude lower. Because of the low deflagration speed, the

---

[1] Based on estimates of the thermal diffusion coefficient, the width of a deflagration wave profile is on the order of 0.1 micron.

Table 6.1: Key steps in the Ignition & Growth concept [Lee and Tarver, 1980]

IG.0: Heterogeneous HE
Meso-scale pores and cracks
Inter-granular or intra-granular
sub-micron to micron scale

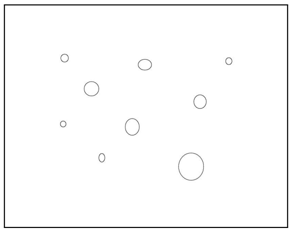
potential hotspot sites

IG.1: Shock front collapses pores
Generates localized regions with temperature $T \gg T_{shock}$
Reactants hotspots form on pore implosion time scale
of a few times (pore diameter)/(shock speed) $\leq 1\,\mu$s
With increasing shock pressure, implosion time decreases
and hotspot temperature increases

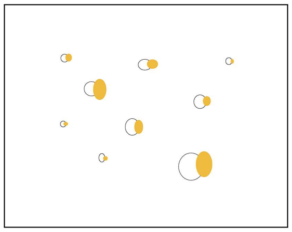
shock sweeps over pores

IG.2: Burn centers form
Competition between heat conduction & reaction
Depending on hotspot size and temperature
hotspots either quench or thermally runaway forming
Products burn centers with $T \gtrsim T_{deflagration} \sim 3000\,\mathrm{K}$
Burn center density increases with shock pressure

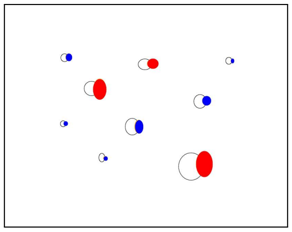
Ignition phase

IG.3: Burn centers trigger reactive wavelets

$$\boxed{\begin{aligned}&\text{Vol avg burn rate} = (\text{burn center number density}) \times \\ &\qquad(\text{avg wavelet front area}) \times (\text{deflagration speed})\end{aligned}}$$

Burn rate increases as front area grows
Width of reactive front very narrow ($\lesssim 0.1$ micron)
Reactants and products are phase separated
with products having a higher temperature

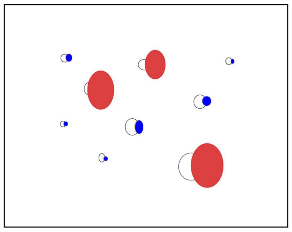
Early growth phase

IG.4: Depletion of reactants
Reactive wavelets overlap decreasing front area
Burn rate decreases as front area shrinks
λ dependence of burn rate is geometric effect
from growth of wavelets

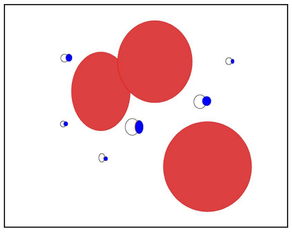
Late growth phase

pressure jump across a deflagration wave is very small. Hence, pressure equilibrium between the reactants and products is a good approximation.

Based on growth phase for the ignition & growth concept, steps IG.3 and IG.4, an estimate of the time for an explosive to burn completely is $\frac{1}{2}\,d_{avg}/D_{defl}$, where d_{avg} is the average distance between burn centers, and D_{defl} is the deflagration wave speed. Hence, the volume average burn rate is $\mathcal{R} \sim 2D_{defl}/d_{avg}$. Despite $D_{defl} \ll D_{CJ}$, a sufficiently large rate for a SDT can be obtained if d_{avg} is sufficiently small. However, d_{avg} is constrained by the pore size and the porosity of the explosive.

The number of pores can be related to the volume of a pore and the porosity

$$\text{porosity} = \frac{\text{pore volume}}{\text{total volume}} \times (\text{number of pores}) \ . \tag{6.1}$$

To understand the scaling of the rate with pore size, for simplicity the distinction between pores, hotspots and burn centers will be neglected. The initial volume average burn rate listed in step IG.3 can be re-expressed as

$$\mathcal{R}_0 \sim \frac{\text{pore area}}{\text{pore volume}} \times \text{porosity} \times D_{defl} \ . \tag{6.2}$$

Since the area to volume ratio scales as 1/(pore size), at fixed porosity the rate can be made sufficiently large by having a large number of very small pores.

Moreover, as discussed in sub-section 1.3.2, USANS measurements of PBXs show a significant volume of pores with diameter below 1 micron. As an illustrative example, at 1 percent porosity the number of pores with diameter less than 1 micron in a volume of 1 mm^3 would be greater than 2.5e6. This is large enough to expect that the average response of an HE to be reproducible with a burn rate based on the ignition & growth concept of hotspots.

Additional comments:

1. Model dependent variables.
   Since the average burn rate is proportional to the number density of burn centers, which is set by lead shock, burn models need to keep track of the lead shock pressure. In general, homogenized burn models may need 1 or more model dependent 'grid' variables. This is analogous to material strength models using extra variables for plastic strain, dislocation density and work hardening.

2. Hotspot mechanism for shock initiation.
   For shock pressures in the range of Pop plot data, simulations show that the hotspot temperature is high enough to generate burn centers; see for example [Nassar et al., 2019, figs 8 & 16] and references therein. Moreover, for stronger shocks, a greater number of hotspots become burn centers. Other dissipative mechanisms, such as plastic work, do not generate high enough temperatures to promptly trigger burn centers.

3. Pore collapse at low shock pressure.
   Below the range of Pop plot data, pore collapse does not generate high enough hotspot temperatures. Experiments with PBX 9501 show that below 1 GPa, the shock profile has a non-zero width; see [Dick et al., 1998, figs 6–8]. (This is likely due to plastic yield at the contact surface between grains supplying the needed shock dissipation.) When the shock rise time is comparable or larger than pore collapse time, the effective shock pressure for pore collapse is limited. This in turn limits the pore collapse temperature. In this case, other hotspot mechanisms would be needed, such as shear heating for low velocity impact of a projectile on an HE, and the time scale for ignition would be longer than occurs for SDT.

4. Length scales.
   The size of a hotspot is much less than the reaction-zone width of a detonation wave. Consequently, a single hotspot can release enough energy to trigger a deflagration wavelet, but not a detonation wave.

CHAPTER 7

Diameter effect and curvature effect

For a planar detonation wave, it follows from the detonation locus in the (V, P)-plane (see for example figure 3.1) and the slope of the Rayleigh line through the CJ state, Eqs. (3.5) and (3.3), that $(P_{CJ} - P_0)/(V_0 - V_{CJ}) = (\rho_0 D_{CJ})^2$. Then since the Rayleigh line is tangent to the detonation locus at the sonic point, it then follows that the CJ detonation wave has the minimum detonation speed and the sonic point is at the end of the reaction zone. Both of these properties break down for a curved detonation wave.

This gives rise to phenomena know as the *diameter effect* and the *curvature effect*. For both phenomena, the detonation speed is less than the minimum based on the detonation locus. This property of the detonation speed for an unsupported curved detonation wave is observed in data from unconfined rate sticks with different diameters.

An *unconfined rate stick* is an HE cylinder surrounded by air. It is detonated at one end and is sufficiently long for the axial detonation speed to become steady. A rule of thumb is that a run distance of 4 diameters is large enough to achieve a steady detonation speed, within measurement uncertainty. Due to the boundary condition that the HE is confined by air, which has a low shock impedance compared to solid HE, the detonation wave will have a curved front.

The detonation speed is measured with timing pins along the length of the rate stick. With a careful setup, the measured detonation speed can be constant to within a few tenths of a percent; see for example [Campbell, 1984]. We note that the measured detonation speed is the average speed over the distance between the timing pins, and not the instantaneous wave speed inferred from reaction-zone profile experiments discussed in subsection 4.3.2. The difference is from the HE heterogeneities which gives rise to short-wavelength fluctuations within the reaction zone.

The **diameter effect** is the dependence of the axial detonation speed D_z on the diameter of a rate stick. The **curvature effect** is the dependence of the detonation speed on the local front curvature, *i.e.*, the relation $D_n(\kappa)$, where D_n is the normal wave speed corresponding to the lead shock pressure and κ is the sum of the principal curvatures. $D_n(\kappa)$ can be determined from the shape of the detonation wave front; *e.g.*, a streak camera measurement of the break out times along a diameter at the end of the rate stick; see 7.4 for details.

7.1 Diameter effect

Curves showing the diameter effect are usually plotted as D_z versus $1/R$, where D_z is the axial detonation speed and R is the cylinder radius. For several selected HEs, diameter effect curves are shown in figure 7.1. For large R, it can be seen that the detonation speed is linear

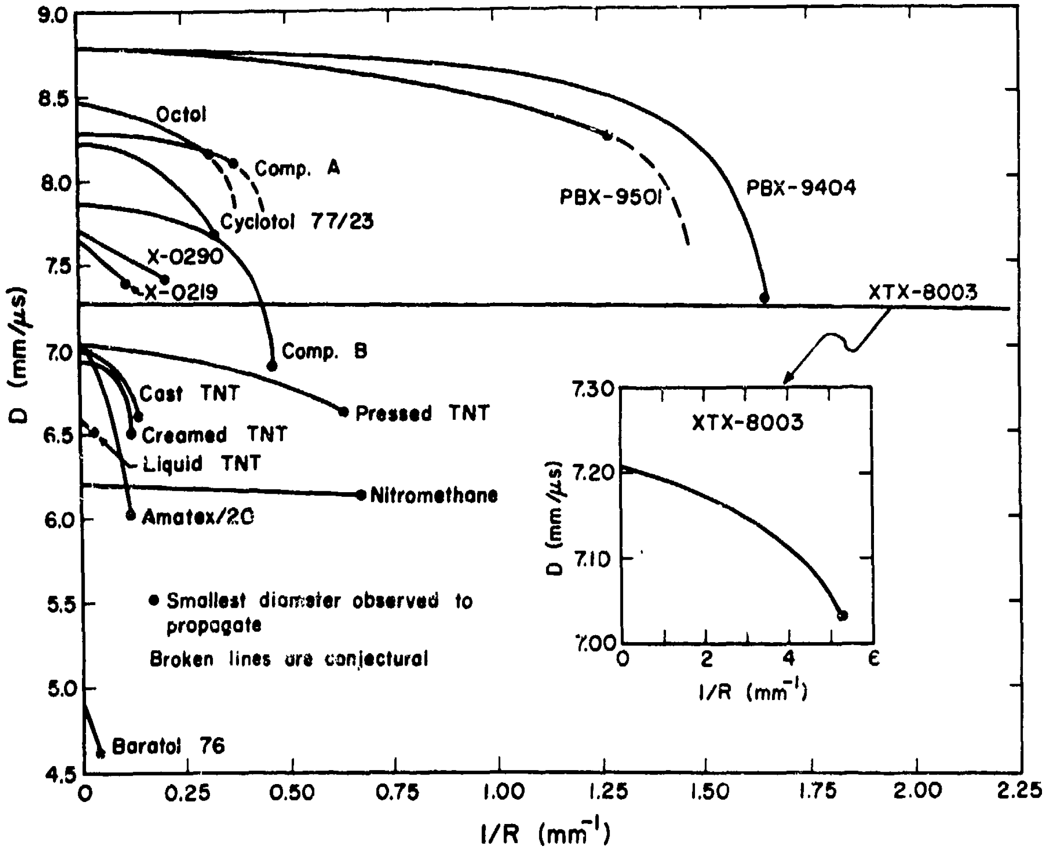

Figure 7.1: Detonation speed versus $1/R$ showing the diameter effect for several HEs [Campbell and Engelke, 1976, fig 2].

in $1/R$; *i.e.*, the detonation speed is given by

$$D_z(1/R)/D_{CJ} \rightarrow 1 - A/R \ , \tag{7.1}$$

where A has dimensions of length and corresponds to the slope of the normalized detonation speed, $D_z(1/R)/D_{CJ}$, at $1/R = 0$. This can be used to extrapolate diameter effect data to the planar limit, $R \rightarrow \infty$, and determine the CJ detonation speed; *i.e.*, $D_z(1/R) \rightarrow D_{CJ}$ as $1/R \rightarrow 0$. As will be discussed later, figure 8.2 shows that as R increases the shape of the detonation front converges to planar. The convergence is not uniform due to the boundary condition at the edge of the HE.

The function $D_z(1/R)$ has two important properties. First, the detonation speed is monotonically decreasing as $1/R$ increases, and for R finite is less than the CJ detonation speed, which is the minimum planar (1-D) detonation speed.

Second, there is a minimum radius, shown in figure 7.1, below which a detonation wave fails to propagate. The corresponding diameter, is known as the *failure diameter*. As discussed in the next chapter, the failure is due to energy flow in the reaction zone transverse to the detonation front.

We note that a rate stick confined by different inerts would display different detonation speeds with radius, and have different failure diameters. Moreover, the diameter effect is for a specific geometry with a specific boundary condition, namely, an unconfined cylinder of HE. Other geometries, such as a 3-D slab of HE with a rectangular cross section, would also display a detonation speed less than D_{CJ} and failure to propagate below a critical size.

As we will see in later sections, the diameter effect can be explained by the curvature effect. Moreover, the diameter effect can be determined utilizing an algorithm based on $D_n(\kappa)$ known as **Detonation Shock Dynamics**, see subsection 7.2.3. Hence, the curvature effect is more general than the diameter effect.

7.2 Overview of curvature effect

The review article by Bdzil and Stewart [2007] describes the theory for the propagation of unsupported curved detonation waves. It applies to diverging detonation waves when $\kappa\, w \ll 1$, where κ is the front curvature and w is the reaction-zone width.

The theory utilizes singular perturbation theory to account for the fast time-scale in the main part of the reaction-zone and a slower time-scale in neighborhood of the sonic locus (analog of planar sonic point) near the end of the reaction-zone. The sonic locus is important since only the energy release up to the sonic locus drives the detonation wave. This and the diverging flow cause the detonation speed to decrease with front curvature.

Key results of the theory are listed below:

1. A quasi-steady solution for the 2-D reaction zone to leading order in $\kappa\, w$ consists of the union of 1-D detonation wave profiles normal to detonation front (lead shock wave). Each profile is in the local frame in which the detonation front is at rest. The profiles for curved detonation waves are the analog of the planar ZND wave profile derived in section 4.2. They are specified by a system of ODEs (given in subsection 7.2.1) with a parameter for front curvature κ. The use of 1-D wave profile ODEs for 2-D flow implies that transverse gradients can be neglected compared to streamwise gradients (normal to shock front) when κ is small.

   In addition, boundary conditions at the HE interface are based on shock polars for the confining inert; see subsection 7.2.4.

2. The curved detonation wave profile ODEs correspond to reducing the reactive Euler PDEs to quasi-steady ODEs with a term proportional to κ to account for front curvature; see next subsection. The initial condition for the profile trajectory is the state behind the lead shock. For a given κ, the trajectory is singular unless it goes though the critical point of the ODEs. This condition determines $D_n(\kappa)$. It is discussed in more detail in subsection 7.2.2.

3. The detonation wave propagates with the local normal detonation speed based on the front curvature, *i.e.*, $D_n(\kappa)$; see subsection 7.2.3. This leads to an extension of the programmed burn algorithm described in subsection 3.5 called Detonation Shock Dynamics (DSD). Programmed burn propagates the detonation wave with constant speed D_{cj}, while DSD accounts for the variation of the detonation speed with front curvature; *i.e.*, $D_n(\kappa)$.

7.2.1 Profile ODEs

The ODEs for the 1-D detonation wave profile with front curvature can be derived from either the 2-D PDEs for the reactive Euler equations expressed in terms of the Betrand-intrinsic coordinates for the reaction zone, see for example [Yao and Stewart, 1996, Appendices A & B and eqs B1–B5], or the 1-D PDEs for cylindrically symmetric reactive flow, see for example [Bdzil and Stewart, 1989]. Here we derive the profile ODEs from the reactive cylindrically symmetric flow PDEs

$$\partial_t \begin{pmatrix} \rho \\ \rho\, u \\ \rho\, E \end{pmatrix} + \partial_r \begin{pmatrix} \rho\, u \\ \rho\, u^2 + P \\ \rho\, u\, (E + PV) \end{pmatrix} = -\frac{1}{r} \begin{pmatrix} \rho\, u \\ \rho\, u^2 \\ \rho\, u\, (E + PV) \end{pmatrix} , \tag{7.2}$$

where $E = e + \frac{1}{2}\, u^2$, $\frac{1}{r}$ can be replaced by the front curvature κ, and $(\partial_t + u\partial_r)\lambda = \mathcal{R}$.

There are two parts to deriving the profile ODEs. First, the PDEs (7.2) are reduced to ODEs with the detonation speed (D) and front (κ) as fixed parameters. Second, the ODEs are transformed in order that the singularity at the sonic point with respect to the front, ($u - D = c$), stands out.

For a steady right facing detonation in the Lab frame (reactant ahead of lead shock at rest), the hydro variables (V, e, u, λ) are all functions of the independent variable $\xi = r - D\,t$. Hence, $\partial_r = \mathsf{d}/\mathsf{d}\xi$ and $\partial_t = -D\,\mathsf{d}/\mathsf{d}\xi$. Substituting these derivatives, the PDEs reduce to the ODEs

$$\frac{\mathsf{d}}{\mathsf{d}\xi}\Big(\rho\,(u-D)\Big) = -\kappa\rho\,u \tag{7.3a}$$

$$\frac{\mathsf{d}}{\mathsf{d}\xi}\Big(\rho\,u\,(u-D)+P\Big) = -\kappa\rho\,u^2 \tag{7.3b}$$

$$\frac{\mathsf{d}}{\mathsf{d}\xi}\Big(\rho\,(u-D)\,(E+P\,V)+D\,P\Big) = -\kappa\rho\,u\,\big(E+P\,V\big) \tag{7.3c}$$

$$\frac{\mathsf{d}}{\mathsf{d}\xi}\Big(\lambda\Big) = \frac{\mathcal{R}}{u-D} \tag{7.3d}$$

For a quasi-steady wave, we take κ and D to be fixed parameters. This assumes that (profile width) $\cdot\,\kappa \ll 1$ and D varies slowly in time.

These equations can be simplified. Multiplying Eq. (7.3a) by u and subtracting it from Eq. (7.3b) yields

$$(u-D)\,\frac{\mathsf{d}}{\mathsf{d}\xi}u + V\,\frac{\mathsf{d}}{\mathsf{d}\xi}P = 0\ . \tag{7.4}$$

Substituting Eq. (7.3a) into the energy Eq. (7.3c) yields

$$(u-D)\frac{\mathsf{d}}{\mathsf{d}\xi}\Big(e+\frac{1}{2}u^2+P\,V\Big) + D\,V\frac{\mathsf{d}}{\mathsf{d}\xi}P = 0\ . \tag{7.5}$$

Substituting Eq. (7.4) into the energy Eq. (7.5) to eliminate the $\mathsf{d}(u^2)/\mathsf{d}\xi$ term and combining P and V terms yields

$$(u-D)\left[\frac{\mathsf{d}}{\mathsf{d}\xi}\,e + P\,\frac{\mathsf{d}}{\mathsf{d}\xi}V\right] = 0\ . \tag{7.6}$$

Since the mass flux $\rho\,(u-D)$ is not zero, the second factor on left hand side of Eq. (7.6) must be zero. Hence,

$$\frac{\mathsf{d}}{\mathsf{d}\xi}\,e + P\,\frac{\mathsf{d}}{\mathsf{d}\xi}V = 0\ . \tag{7.7}$$

This implies that the entropy change is due only to the reaction.

These equations for the wave profile are in the Lab frame. For some purposes it is convenient to transform to the shock-attached frame for which the lead shock is stationary. This amount to changing the velocity

$$\widetilde{u} = u - D\ . \tag{7.8}$$

In addition, the initial condition at the start of the profile (particle velocity) needs to be changed in order to correspond to the lead shock at rest. The profile ODEs are then given by

$$\frac{\mathsf{d}}{\mathsf{d}\xi}\Big(\rho\,\widetilde{u}\Big) = -\kappa\rho\,(\widetilde{u}+D) \tag{7.9a}$$

$$\widetilde{u}\frac{\mathsf{d}}{\mathsf{d}\xi}\widetilde{u} + V\frac{\mathsf{d}}{\mathsf{d}\xi}P = 0 \tag{7.9b}$$

$$\frac{\mathsf{d}}{\mathsf{d}\xi}e = -P\,\frac{\mathsf{d}V}{\mathsf{d}\xi} \tag{7.9c}$$

$$\frac{\mathsf{d}}{\mathsf{d}\xi}\lambda = \frac{\mathcal{R}}{\widetilde{u}} \tag{7.9d}$$

We note that they are identical to the profile equations given in Stewart and Yao [1998, eqs 1-4]. They differ somewhat from Bdzil and Stewart [1989, eqs 24 a-e]. This is due to the choice of left or right facing wave and choice of frame (Lab or shock-attached). Otherwise the sets of equations are equivalent.

We also note that the cylindrically symmetric PDEs are a special case of the 1-D duct flow equations with $\kappa = (\mathsf{d}A/\mathsf{d}\xi)/A$ where A is the cross sectional area of the duct. Consequently, the quasi-steady detonation profiles can be thought of as corresponding to the flow in a stream tube in the shock-attached frame.

In contrast to the Lab frame, the profile in the shock-attached frame is time independent. Consequently, as we show next, the Bernoulli function $B = e + P\,V + \frac{1}{2}\,\widetilde{u}^2$ is a constant of the motion.

$$\frac{\mathsf{d}B}{\mathsf{d}\xi} = \frac{\mathsf{d}e}{\mathsf{d}\xi} + \frac{\mathsf{d}\,(P\,V)}{\mathsf{d}\xi} + \widetilde{u}\,\frac{\mathsf{d}\widetilde{u}}{\mathsf{d}\xi}\ . \tag{7.10}$$

Substituting Eq. (7.9c) for e, Eq. (7.9b) for $\widetilde{u}$ then combining $P\,V$ term yields $\frac{\mathsf{d}B}{\mathsf{d}\xi} = 0$. The Bernoulli function can be used to replace equation for $\mathsf{d}u/\mathsf{d}\xi$, hence reduce the number of ODEs for the system.

Next we derive form of the profile ODEs that shows the singular nature of the sonic locus. From thermodynamic relations for the pressure derivatives, Eq. (4.8), it follows that

$$\frac{\mathsf{d}P}{\mathsf{d}\xi} = -(\gamma-\Gamma)\frac{P}{V}\frac{\mathsf{d}V}{\mathsf{d}\xi} + \frac{\Gamma}{V}\frac{\mathsf{d}e}{\mathsf{d}\xi} + \rho\,c^2\sigma\frac{\mathsf{d}\lambda}{\mathsf{d}\xi}\ . \tag{7.11}$$

Combined with the entropy equation, Eq. (7.9c), to eliminate e in Eq. (7.11) yields

$$\frac{\mathsf{d}}{\mathsf{d}\xi}\big(P\big) - c^2\frac{\mathsf{d}}{\mathsf{d}\xi}\big(\rho\big) = \rho\,c^2\,\sigma\,\frac{\mathcal{R}}{\widetilde{u}}\ . \tag{7.12}$$

Next using Eq. (7.9b) to replace $\mathsf{d}P/\mathsf{d}\xi$ with $\mathsf{d}\widetilde{u}/\mathsf{d}\xi$ gives

$$\rho\,\widetilde{u}\,\frac{\mathsf{d}}{\mathsf{d}\xi}(\widetilde{u}) + c^2\frac{\mathsf{d}}{\mathsf{d}\xi}(\rho) = -\rho\,c^2\,\sigma\,\frac{\mathcal{R}}{\widetilde{u}}\ . \tag{7.13}$$

Then Eq. (7.9a) can be used to eliminate $\mathsf{d}\widetilde{u}/\mathsf{d}\xi$ from Eq. (7.13). The result is

$$(c^2-\widetilde{u}^2)\,\frac{\mathsf{d}}{\mathsf{d}\xi}\rho = -\rho\,c^2\,\frac{\sigma\,\mathcal{R}}{\widetilde{u}} + \kappa\,\rho\,u\,\widetilde{u}\ . \tag{7.14}$$

Finally, combining Eq. (7.14) with Eq. (7.9)a to eliminate $\mathsf{d}\rho/\mathsf{d}\xi$ gives

$$(c^2-\widetilde{u}^2)\,\frac{\mathsf{d}}{\mathsf{d}\xi}(\widetilde{u}) = c^2\left[\sigma\,\mathcal{R} - \kappa\,u\right]\ . \tag{7.15}$$

Collecting the 4 equations for $\mathsf{d}\rho/\mathsf{d}\xi$, Eq. (7.14), $\mathsf{d}\widetilde{u}/\mathsf{d}\xi$, Eq. (7.15), $\mathsf{d}e/\mathsf{d}\xi$, Eq. (7.9c), and $\mathsf{d}\lambda/\mathsf{d}\xi$, Eq. (7.9d), the final ODEs for the wave profile are

$$(c^2-\widetilde{u}^2)\,\frac{\mathsf{d}}{\mathsf{d}\xi}(V) = \left[c^2\,\frac{\sigma\,\mathcal{R}}{\widetilde{u}} - \kappa\,u\,\widetilde{u}\right]V \tag{7.16a}$$

$$(c^2-\widetilde{u}^2)\,\frac{\mathsf{d}}{\mathsf{d}\xi}(\widetilde{u}) = c^2\left[\sigma\,\mathcal{R} - \kappa\,u\right] \tag{7.16b}$$

$$\frac{\mathsf{d}}{\mathsf{d}\xi}(e) = -P\,\frac{\mathsf{d}}{\mathsf{d}\xi}(V) \tag{7.16c}$$

$$\frac{\mathsf{d}}{\mathsf{d}\xi}(\lambda) = \frac{\mathcal{R}}{\widetilde{u}} \tag{7.16d}$$

where $\widetilde{u}$ is velocity in shock-attached frame and $u = \widetilde{u} + D$ is the velocity in the Lab frame. The initial condition of the ODEs is the rest state of the shock; *i.e.*, shock-attached frame. The EOS for the partly burned HE determines P, c, σ and $\mathcal{R}$ as functions of V, e and λ. We note that when $\widetilde{u}^2 = (u-D)^2 \to c$, both $\mathsf{d}\,V/\mathsf{d}\xi$ and $\mathsf{d}\,\widetilde{u}/\mathsf{d}\xi$ blow up. This singularity at the critical point λ_c is discussed in the next subsection. We note that only the reaction for $\lambda < \lambda_c$ is decoupled from the flow behind. Hence, the reaction after the critical point is not steady.

Alternatively, the profile ODEs can be expressed with the reactive coordinate λ as independent variable instead of ξ, and P as dependent variable instead of e; see Stewart and Yao [1998, eqs 18-24] and references therein. The time or spatial dependence of the wave profile can be determined parametrically by adding an auxiliary or passive ODE, $\mathsf{d}\xi/\mathsf{d}\lambda = \widetilde{u}/\mathcal{R}$ for $\xi = x - D\,t$, *e.g.*, the pressure profile would be $\big(\xi(\lambda),\ P(\lambda)\big)$ for $0 \le \lambda \le \lambda_c$. As noted previously, $\widetilde{u}$ can be determined from the Bernoulli function instead of Eq. (7.16b). Then with reactive coordinate λ, the system would reduce to 2 ODEs for $\mathsf{d}\rho/\mathsf{d}\lambda$ and $\mathsf{d}e/\mathsf{d}\lambda$.

7.2.2 Diverging and converging detonation waves

The profile ODEs, Eq. (7.16), apply to both diverging and converging detonation waves with the convention that κ is positive for diverging detonation waves and negative for converging detonation waves. A diverging detonation wave corresponds to the center of curvature lying within the products behind the front. Similarly, a converging detonation wave corresponds to the center of curvature lying within the reactants ahead of the front.

The properties of the profile ODEs depends on the sign of κ. There are 3 cases:

1. $\kappa = 0$, planar detonation front.
   The detonation wave profile ODEs, Eq. (7.16), reduce to the planar ZND profile ODEs, Eq. (4.10), when adjusted for the frame of reference. The ZND profile is subsonic for overdriven detonation waves and sonic at the profile end for underdriven detonation waves.

2. $\kappa > 0$, diverging detonation front.
   There are 2 types of profiles. The first type is completely subsonic, *i.e.*, $c^2 - \widetilde{u}^2 > 0$. These profiles are the analogue of planar overdriven detonation waves. The second type has a sonic point, $c^2 - \widetilde{u}^2 = 0$, within the profile. The portion of the profile from the front to the sonic point is acoustically decoupled from the flow behind. These detonation profiles are self-supporting. They are the analogue of a planar CJ detonation wave. Since only the energy release up to the sonic point drives the CJ-like detonation, the detonation speed is less than D_{CJ}. The diverging flow further lowers the detonation speed.

   However, there is a complication. The profile has a singularity at the sonic point unless the rate condition $\sigma\mathcal{R} - \kappa(\widetilde{u} + D_n) = 0$ also vanishes. Note that $\widetilde{u} + D_n = u$ is the velocity in the Lab frame. The point at which both conditions are met is a critical point of the ODEs. The only admissible profile with a sonic point must have a detonation speed D_n such that the trajectory starting from the reactants shock state with shock speed D_n goes through the critical point. This defines the $D_n(\kappa)$ curve.

   For some EOS and rate models the D_n curve can be Z-shaped, hence multi-valued; see [Stewart and Yao, 1998, Fig 2]. The branch with the highest D_n is used for the $D_n(\kappa)$ curve. Hence, the profile ODEs determine the curvature effect. The middle branch is unstable and the lower branch is associated with "low velocity detonations"; see [Stewart and Yao, 1998], [Gao et al., 2014] and references therein. Since the critical point is a saddle type, there are overdriven detonation wave profiles for all $D > D_n(\kappa)$.

3. $\kappa < 0$, converging detonation front.
   The rate condition is always positive; *i.e.*, $\sigma\mathcal{R} - (\widetilde{u} + D_n)\,\kappa > 0$. Therefore, the sonic condition cannot be zero. Consequently, all converging steady state reaction-zone profiles must be subsonic. This means that the converging detonations are the analog of

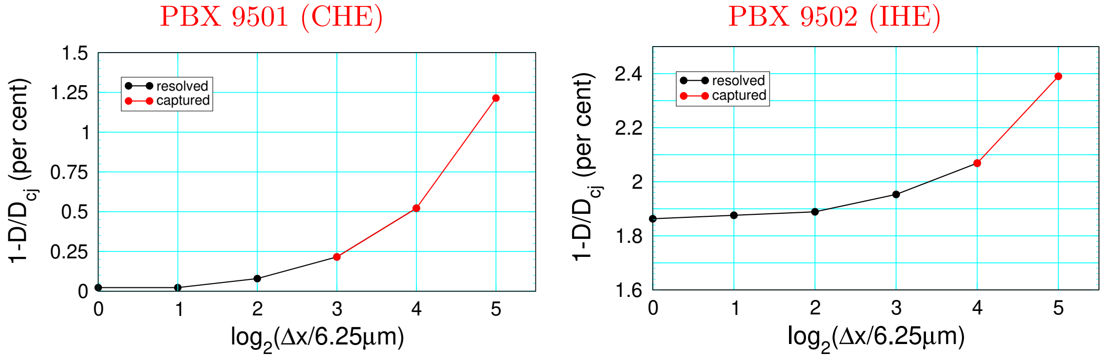

Figure 7.2: Detonation speed versus cell size for 1 inch cylinder test. Simulations with the SURF model using the xRage code; see [Menikoff, 2019b, fig 5 and 13]. Black portion of the curves correspond to the reaction zone at least partially resolved. Red portion of the curves correspond to only 1 or 2 cells in the reaction zone profile. The largest cell size is 0.2 mm; 32 times the finest cell size.

planar overdriven detonation waves. Moreover, there is a profile for all $D_n \geq D_{min}(\kappa)$, with $D_{min}(\kappa) > D_{CJ}$. Furthermore, $D_{min}(\kappa)$ increases with increasing $-\kappa$.

For a planar detonation wave, the detonation state depends only on the EOS and is independent of the burn rate; see section 4.2. In contrast, for a curved detonation wave, $\kappa \neq 0$, the detonation state is determined by integrating the reaction-zone profile ODEs. For a specified detonation speed, the detonation pressure depends on the burn rate. Moreover, for an underdriven diverging detonation with $\kappa > 0$ only the portion of reaction zone from the front to the sonic point can be steady. One reason an underdriven diverging detonation wave has a lower detonation speed is that the HE energy released after the sonic point does not contribute to driving the detonation wave.

For the curvature effect, the reaction-zone width is an important length scale. The slope of $D_n(\kappa)$ strongly depends on the reaction-zone width. Since the reaction-zone width is small, numerical resolution can greatly affect the detonation speed. As an illustrative example, the dependence of the detonation speed on cell size for the cylinder tests of PBX 9501 and PBX 9502 are shown in figure 7.2. It can be seen that the accuracy of the detonation speed decreases rapidly when the reaction zone is captured rather than resolved; *i.e.*, the cell size is greater than the reaction-zone width of the burn model. In effect, with coarse resolution the numerical reaction-zone width determines the magnitude of the curvature effect. We note that the convergence rate depends on the burn model and the hydro code used for the simulations.

There are 2 physically distinct regimes associated with the burn rate that are important for calibrating empirical burn rates. A high pressure regime, $P_{cj} \lesssim P < P_{vn}$, associated with propagating detonation waves, and a low pressure regime, $P \lesssim P_{cj}$, associated with shock initiation. Different types of data are used to calibrate empirical burn rates in these regimes;

curvature effect data for the high pressure regime, and Pop plot data for the lower pressure regime. We also note that the resolution requirement is higher for the propagating regime since the burn rate of a PBX increases rapidly with pressure. Consequently, burning gives rise to steeper gradients in the propagation regime than the ignition regime.

The curvature source terms in Eq. (7.16) also enter into the characteristic equation and affect the acceleration of a shock wave. Consequently, shock initiation involves a competition among 3 physical effects: i. Pressure gradient behind lead shock front, ii. Chemical reaction source term, and iii. Geometric source term for the front curvature of the lead shock.

7.2.3 Detonation Shock Dynamics (DSD)

DSD can be viewed as a generalization of the programmed burn model (section 3.5) that accounts for the local curvature dependent detonation speed. It applies to propagating underdriven diverging detonation waves, since only they are acoustically decoupled from the flow behind the detonation wave.

The evolution of the detonation front or burn table is based on a level set algorithm developed by Aslam et al. [1996]. The algorithm computes both the local normal detonation speed D_n the burn time. We note that the use of $D_n(\kappa)$ implies that the HE is initially at rest. In addition, the algorithm requires the boundary angles between the detonation front and interfaces with inert materials.

Away from HE boundaries, the evolution equations for the front are hyperbolic. In the neighborhood of the boundary, the evolution equation can be parabolic. The boundary angle is based on shock polars for the reactants EOS and an inert EOS; see [Short and Quirk, 2018] and references therein. Shock polars are briefly discussed in the next subsection.

To minimize potential issues with the hydro front and the burn front getting out of sync, see figures 3.3 and 3.4, Wescott [2007] suggested that the standard pseudo-burn rate, Eq. (3.23), have an additional factor of D_n to a power, *i.e.*,

$$\mathcal{R}(x,t,\lambda;t_{bt},D_n) = \begin{cases} [1-\lambda]^n\,\tau^{-1}\cdot\left[D_n(x)/D_{CJ}\right]^d\ , & \text{if } t > t_{bt}(x) \text{ and } \lambda < 1; \\ 0\ , & \text{otherwise;} \end{cases} \tag{7.17}$$

where $D_n(x)$ is the local normal detonation speed, $t_{bt}(x)$ is the burn time, and the parameters of the pseudo-burn rate (n, τ and d) fit to the $D_n(\kappa)$ relation. To some extent, the factor with D_n would allow the pseudo-rate and hence the numerical reaction-zone width to be adjusted with front curvature.

Another potential issue with a pseudo-burn rate is that for a given κ the detonation pressure on the sonic locus may differ from that of a reactive-burn model which is fit to $D_n(\kappa)$ and with the reaction-zone numerically resolved. This is especially so if the numerically stable pseudo reaction-zone profile has burning occurring in the shock rise, as seen in figure 3.4, instead of a curved detonation profile.

7.2.4 Shock polars

We have previously seen in 2.4 that the solution to a 1-D shock impedance match can be determined with a graphical analysis as the intersection in the (u, P)-plane of the wave curves (shock locus in compression and rarefaction locus in expansion) for the outgoing left and right states. The graphical solution is possible because u and P are continuous across a contact.

Similarly, there is a graphical analysis for a steady 2-D wave pattern generated by the impact of an oblique shock on a material interface. In both cases there is an incoming shock on a material interface that generates 3 outgoing waves; transmitted shock, a contact (deflected material interface), and a reflected shock or rarefaction.

For a 1-D impedance match the elementary waves are shocks in compression, rarefactions in expansion and contacts (entropy discontinuity and/or material interface). The analog for 2-D wave patterns are oblique shocks in compression, Prandtl-Meyer fans in expansion and contacts (entropy discontinuity and/or material interface plus a slip line which is a discontinuity in tangential velocity).

An oblique shock is characterized by a shock polar (analog of 1-D wave curve). These are the shock pressure as a function of the turning angle, θ, which is the deflection angle of streamline through the oblique shock; see Eq. (7.18). Two-dimensional wave patterns generated by an incoming shock impacting a material interface have three outgoing wave; transmitted oblique shock, contact wave (which is deflected material interface) and reflected oblique shock or Prandtl-Meyer fan. In the frame in which the wave pattern is stationary, the pressure and tangential velocities along the outgoing contact are continuous. Consequently, the outgoing waves can be determined graphically as the intersection of the outgoing shock polars.

Illustrative examples of the 1-D and 2-D graphical analyses are shown in figures 7.3 A and C, respectively. As shown in figure 7.3 B, for an oblique shock the particle velocity and tangential component of the velocity, $q_\parallel$, are continuous across an oblique shock. Due to $q_\parallel$, the polar pressure $P(\theta)$ is double valued. Below the sonic pressure, which is below the maximum turning angle as shown for red polar in figure 7.3 C, the flow behind the shock is supersonic. Above the sonic pressure, the flow is subsonic. Moreover, there is no reflected wave from a point on the shock polar above the sonic point. For an HE, it is the reactants shock polar with the incoming velocity corresponding to the CJ detonation speed (*i.e.*, $q_0 = D_{CJ}$) that is used to determine the boundary angle and interface pressure. The peak pressure on this polar corresponds to the VN spike pressure.

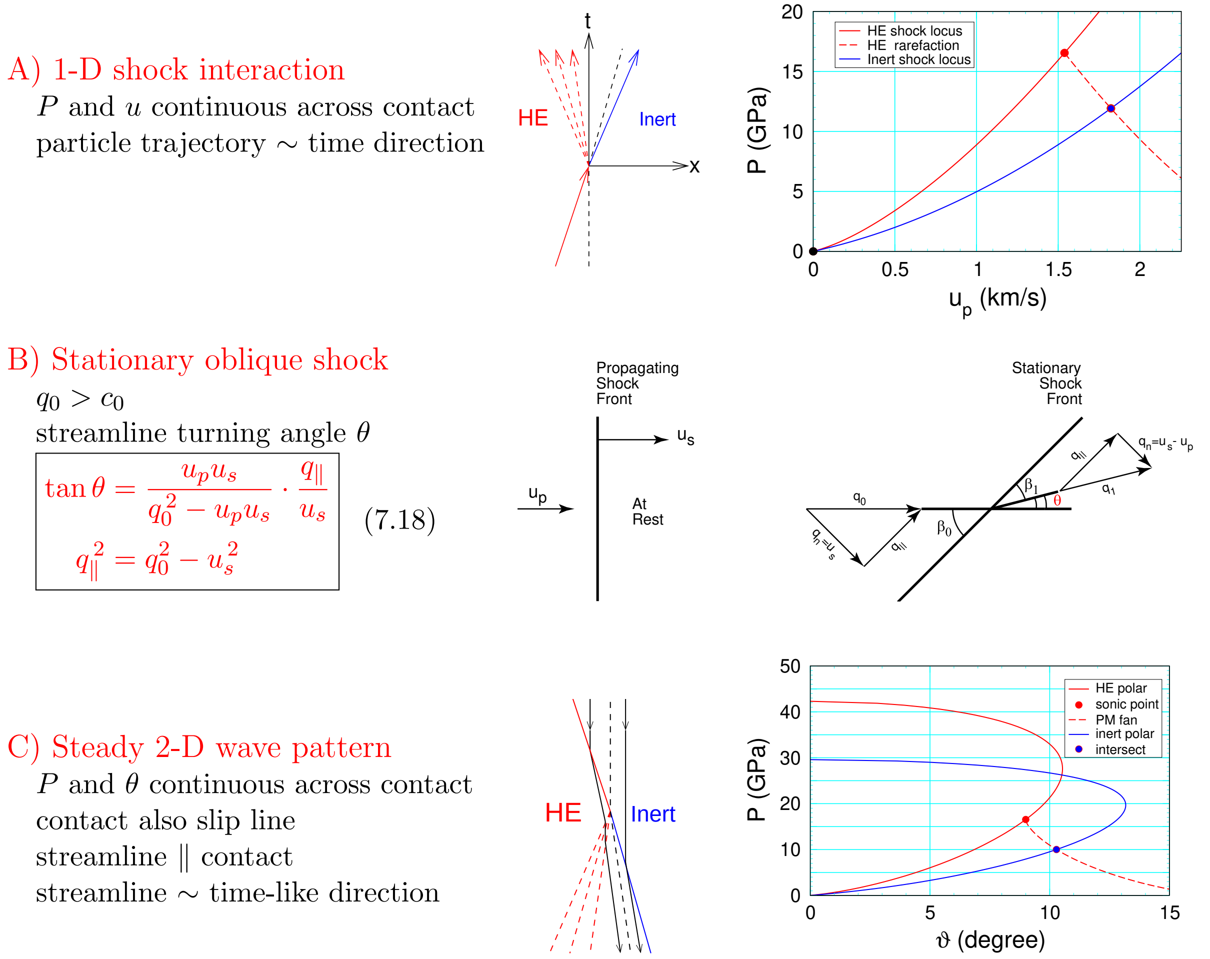

$$\boxed{\begin{aligned}\tan\theta &= \frac{u_p u_s}{q_0^2 - u_p u_s}\cdot\frac{q_\parallel}{u_s}\\ q_\parallel^2 &= q_0^2 - u_s^2\end{aligned}} \qquad (7.18)$$

Figure 7.3: Illustrative examples of graphical solutions for a shock impedance match in the (u, P)-plane using wave curves, and for a steady wave pattern in the (θ, P)-plane using shock polars.

The shock polar plot in figure 7.3 C shows the case for PBX 9502 confined by plexiglass (PMMA), for which the reflected wave corresponds to a Prandtl-Meyer fan that goes through the sonic point on the HE shock polar. This case occurs when the detonation is weakly confined by the inert. Weak confinement corresponds to the shock impedance of the inert being less than that of the reactants. In this example, the sonic pressure is below the CJ pressure and much lower than the VN state pressure. We note that all weakly confined rate sticks with the same diameter would have the same detonation speed and shape of the detonation front because the HE boundary pressure would be the same; *i.e.*, the sonic pressure on the reactants shock polar.

This example also illustrates a complication of the 2-D shock polar analysis. In contrast to a 1-D impedance match, there can be multiple solutions for the steady 2-D wave pattern, such as a Prandtl-Meyer fan in figure 7.3 C starting below the HE sonic point. For a curved detonation front, the solution for the HE polar needs to be above the sonic point for an oblique shock and at or above the sonic point for a Prandtl-Meyer fan. Other solutions are not physical and inadmissible; see [Short and Quirk, 2018, figs 5 & 7].

One issue with the HE boundary condition is due to surface roughness at the HE and/or inert interfaces. If the surface roughness gives rise to small gaps comparable to the size of the reaction-zone width, then the confinement pressure would effectively be less than that derived from the shock polar analysis. For a fast reaction rate, the gap size need only be tens of microns to affect the confinement.

7.3 Overdriven curved detonation waves

Supported planar detonation waves can become diverging due to side rarefactions. In general, overdriven detonation waves can be either converging or diverging. Both are subsonic with respect to the flow behind the front and are outside the domain of DSD.

Converging flow ($\kappa < 0$) can cause a pressure gradient to buildup behind a detonation front and increase the detonation speed. In effect, the converging flow can provide the support for an overdriven detonation. The analogy for a converging shock wave is the Guderley similarity solution; see [Whitham, 1974, pp 196–198].

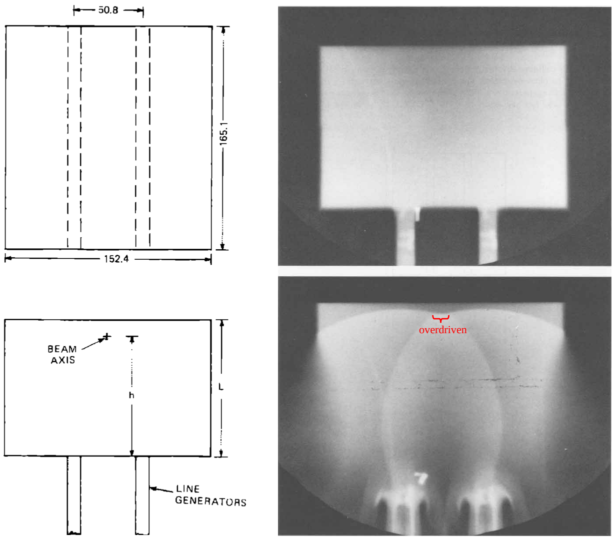

Figure 7.4: Illustrative example of overdriven detonation wave resulting from the collision of 2 diverging detonation waves in PBX 9404. Phermex radiograph of shot # 1037 [Mader, 1979]. Top is static and bottom dynamic. Red bracket indicates overdriven portion of detonation front. Below the detonation front are shock waves in the PBX products.

Locally overdriven detonation waves can also be generated by the collision of diverging detonation fronts initiated by nearby detonators. An illustrative example of this is shown in figure 7.4.

7.4 Experimental measurement of $D_n(k)$

For an unconfined rate stick, the axial detonation speed, D_z, and the shape of the detonation front, $z(r)$, can be measured. This data can be used to determine the curvature effect relation $D_n(\kappa)$ as follows.

The detonation front is a surface of revolution about the cylinder axis. The sum of the 2 principal components of the curvature tensor (radial and azimuthal directions) is given by

$$\kappa(r) = \frac{z''(r)}{\left[1 + z'(r)^2\right]^{3/2}} + \frac{z'(r)}{r\left[1 + z'(r)^2\right]^{1/2}} \tag{7.19}$$

where z' and z'' are the first and second derivatives, respectively. The derivatives can be calculated by first fitting the front shape to an analytic function [see Hill et al., 1998] and then taking the derivatives of the fitting function. The fit serves to smooth out the noise in the data, which is important for getting an accurate second derivative.

The normal detonation speed, D_n, is determined by the front shape, see figure 7.5

$$D_n(r) = cos\big(\theta(r)\big) \cdot D_z \ , \tag{7.20}$$

where $\tan(\theta) = \mathsf{d}z/\mathsf{d}r$. The 2 functions $\kappa(r)$ and $D_n(r)$ determine the function $D_n(\kappa)$ parametrically. Illustrative examples of $D_n(\kappa)$ are shown in figure 7.6 for PBX 9501, conventional HE with a fast hotspot burn rate, and for PBX 9502, insensitive HE with fast (hotspot) and slow (carbon clustering) burn rates.

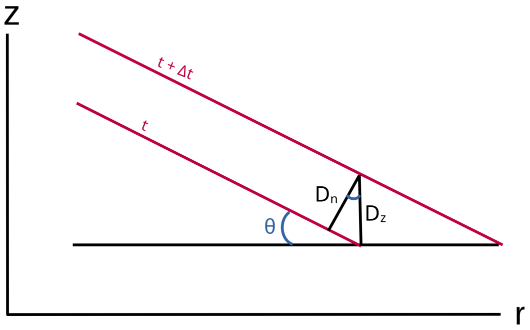

Figure 7.5: Sketch showing shock fronts (red) at times t and $t + \Delta t$ and detonation speeds D_n and D_z.

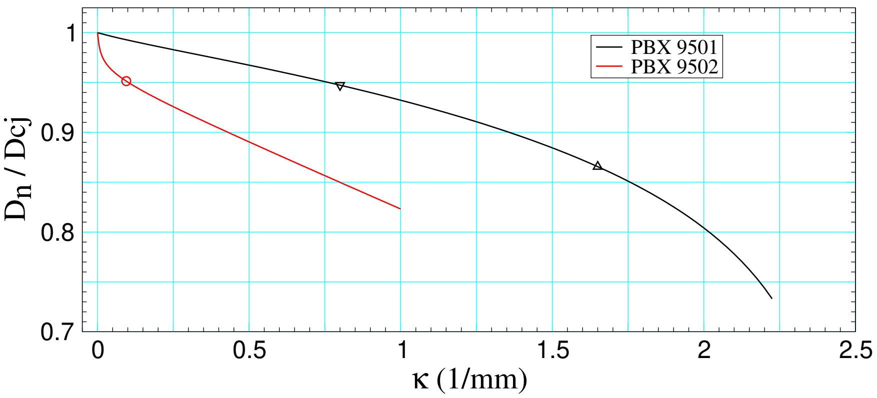

Figure 7.6: Normalized D_n for PBX 9501 Aslam [2007] and PBX 9502 Hill and Aslam [2010]. Black triangles are estimates of curvature on axis just above failure diameter. Red circle corresponds to curvature on axis for the standard 1 inch diameter cylinder test.

The slope of the curves, $\mathsf{d}D_n/\mathsf{d}\kappa$, depends strongly on the reaction-zone width up to the sonic point. For PBX 9501 the narrow reaction-zone width (less than 0.1 mm) gives rise to a relatively small curvature effect up to $\kappa = 0.75$/mm; *i.e.*, $1 - D_n/D_{CJ}$ less than about 5 percent. In contrast, for PBX 9502, the slope starts out as large and then decreases very rapidly too a moderate slope for $\kappa > 0.2$/mm. This is due to the sonic point shifting from the end of the slow burn rate to the end of the fast burn rate.

The failure diameter and issues with the sonic boundary condition are discussed in the next chapter.

CHAPTER 8

Failure diameter, corner turning/dead zones

The phenomena discussed in this chapter, failure diameter and corner turning which leads to dead zones, are inherently multi-dimensional and dynamical processes. Simulations are very helpful in understanding the physical mechanisms that underlie the phenomena. In particular, numerical experiments can provide data that is not accessible with currently available diagnostic techniques, such as a time sequence of 2-D pressure fields or measurements of the reaction progress variable. The trade-off of relying on HE simulations is that they depend on models for the EOS of partly burned HE and an effective burn rate, which may not fully describe the underlying physics. Consequently, we emphasize the qualitative features that are expected to be generally applicable.

To understand the failure diameter, it is helpful to first look at the effect of the sonic boundary condition on the rate stick experiments used to determine the curvature effect. In the next section we show that the sonic boundary condition leads to a boundary layer, which plays an important role in the failure to propagate a detonation wave for small diameter rate sticks.

8.1 Breakdown of DSD assumptions

In the previous chapter we saw that the $D_n(\kappa)$ curve can be derived from rate stick experiments. The curve should be a material property independent of geometry. Figure 8.1 compares the curves derived from experiments with PBX 9502 at 3 rate stick diameters. For $\kappa < 0.2\,\mathrm{mm}^{-1}$, the curves nearly coincide. For larger κ, the curves diverge. This implies that an assumption in the derivation of the curvature effect breaks down.

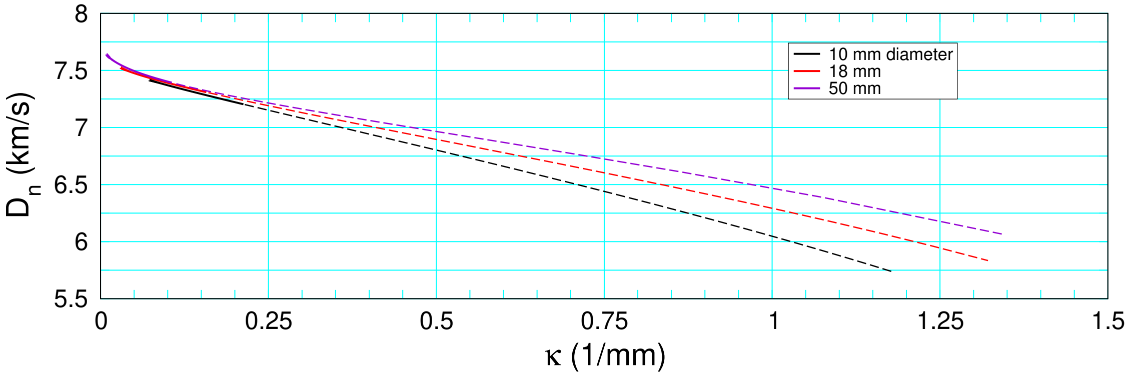

Figure 8.1: Comparison of $D_n(\kappa)$ curves for PBX 9502 at 25 C derived from rate sticks with 3 diameters (listed in the legend) [see fig 6, Hill et al., 1998]. Dashed portion of the $D_n(\kappa)$ curves are derived from data within 1 mm of the rate stick boundary.

Recall for cylindrical geometry that $\tilde{\kappa}(r)$, $\tilde{D_n}(r)$ are functions of r and $D_n(\kappa)$ is defined parametrically as $\big(\tilde{\kappa}(r), \tilde{D_n}(r)\big)$. We'll see in next subsection that the front region of large $\tilde{\kappa}$ is the dashed portion of the curves in figure 8.1, and corresponds to a relatively small interval of r adjacent to the HE boundary. This in turn causes a rapid variation in flow variables along the front and can be thought of as a boundary layer.

8.1.1 Boundary layer

Figure 8.2 shows the front shape, curvature and shock pressure as functions of the normalized radius for the 3 rate stick diameters. The front shape, $z(r)$, comes directly from the experiments of Hill et al. [1998]. The curvature, $\kappa(r)$, is derived from the front shape. The lead shock pressure, $P(r)$, is derived from $D_n(r)$, inferred from the front shape, and the point on the reactants shock locus with wave speed $D_n(r)$ from a fit to shock data; see figure 3.1.

A key point is that the lead shock pressure drops from about 40 GPa on the axis to the sonic point pressure on the shock polar of about 15 GPa at the boundary. Moreover, most of the pressure drop occurs in the last 1 mm adjacent to the boundary. Up to the last mm, $r < R - 1\,\text{mm}$, $\mathsf{d}\kappa/\mathsf{d}r$ and $\mathsf{d}P_s/\mathsf{d}r$ are small. Consequently, the last mm has the appearance of a boundary layer. As previously noted, the $D_n(\kappa)$ curves constructed from $D_n(r)$ and $\kappa(r)$ differ for r in the boundary layer.

The large transverse pressure derivative in the boundary layer would give rise to flow in the reaction zone transverse to the shock front. This violates the curvature effect assumption that the quasi-steady reaction-zone ODEs are for the direction normal to the front, see [Bdzil and Stewart, 1989, eq 24c]. Hence, the transverse velocity derivatives in the boundary layer cannot be neglected.

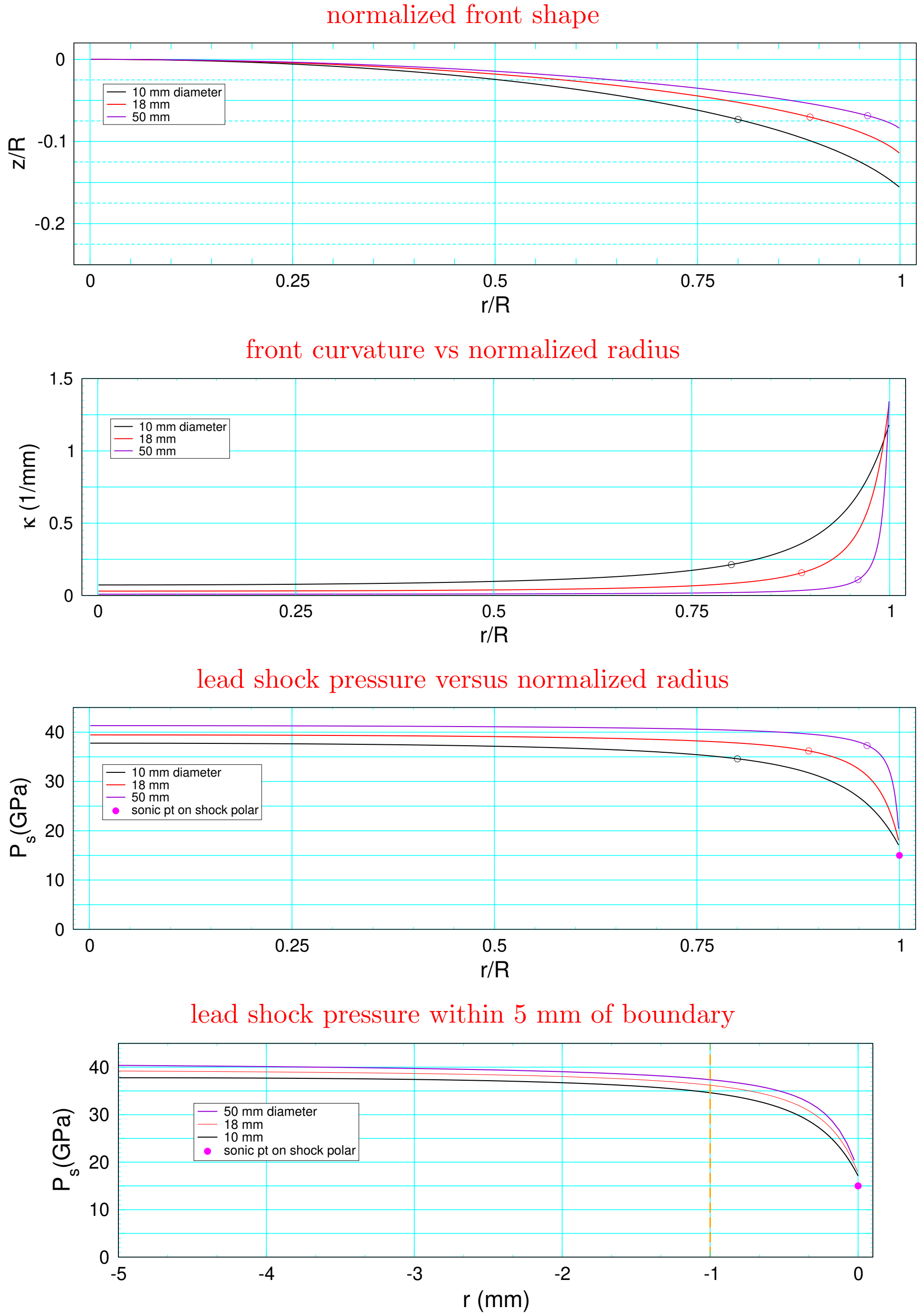

Figure 8.2: Front height and radius (z, r, respectively) are scaled by the rate stick radius R. Top plot for front shape has 1:1 aspect ratio. Open circles denote points 1 mm from the right boundary in the scaled radius plots. For the bottom plot, the shock pressure is shown in a 5 mm neighborhood of the boundary, with the radius shifted to be relative to the right boundary. Dashed orange line denotes point 1 mm from boundary.

8.1.2 Transverse energy flux

Further insight comes from looking at the sonic locus and streamlines near the boundary and the transverse energy flux behind the lead shock as shown in figure 8.3. At the boundary, the sonic locus coincides with the shock front. Consequently, in the boundary layer, the reaction zone up to the sonic locus and the shock pressure are both decreasing. In the neighborhood of the boundary, the reaction energy is not sufficient to support the lead shock. Instead, the transverse energy flux from the interior supports the shock.

The equation for conservation of energy can be expressed as

$$\frac{\partial}{\partial t}\Big[\rho\, E\Big] = -\nabla\cdot\Big[\rho\,\vec{u}\big(E + P\,V\big)\Big]\ , \tag{8.1}$$

where $E = e + \frac{1}{2}|\vec{u}|^2$ is the total specific energy. The radial component of the energy flux is $\text{flux}_r = \rho\, u_r \cdot (E + P\,V)$ where $u_r = \hat{r}\cdot\vec{u}$ is the radial component of the particle velocity and the contribution to the left hand side, *i.e.*, radial energy flow, is $-r^{-1}\partial_r(r\cdot\text{flux}_r)$. The radial energy flow along the shock front is shown in figure 8.3. The peak negative energy flow occurs near the start of the boundary layer; radius of approximately 4 mm. The positive energy flow supports the shock front in the last 0.5 mm adjacent to the boundary.

If the rate stick diameter is too small, the peak negative energy flow is too large to sustain a sufficiently high lead shock pressure. This lowers the reaction rate, which exacerbates the need to support the lead shock in the boundary layer. Simulations in the next section show that this leads to a failure wave propagating from the boundary to the axis. Thus, the failure diameter is determined by the transverse energy flow and not the $D_n(\kappa)$ relation of the curvature effect.

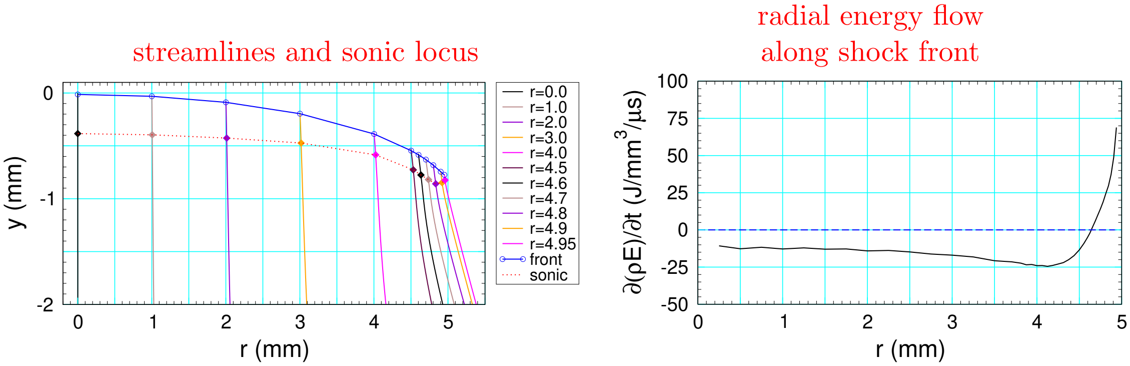

Figure 8.3: For 10 mm diameter PBX 9502 rate stick: Left plot shows shock front (blue line), sonic locus (dotted red line) and stream lines in rest frame of shock front. Right plot shows the transverse energy flow behind the shock front.

Extrapolating the $D_n(\kappa)$ relation to apply DSD for an unconfined rate stick, *i.e.*, diameter effect, is an approximation. Key questions are how accurately the effect of the boundary layer is captured with a boundary angle, and the sensitivity of the axial detonation speed to the boundary angle for the $D_n(\kappa)$ relations derive from different diameter rate sticks as seen in figure 8.1.

8.2 Failure diameter simulations

Unconfined PBX 9502 simulations were performed for rate sticks with diameters slightly higher (10 mm) and slightly lower (8 mm) than the measured failure diameter [Menikoff, 2017a]. The setup is shown in figure 8.4 A. A detonation wave in a large diameter PBX 9502 cylinder is used to initiate a detonation wave in a narrower PBX 9502 test cylinder. This results in a slightly overdriven initial detonation in the test cylinder (both larger detonation pressure and smaller front curvature) and should minimize the run distance needed to reach either a steady detonation or for failure to occur. In addition, a short PMMA collar around the start of the test cylinder was an attempt (partly successful) to block jetting of detonation products from the larger cylinder into the air surrounding the test cylinder.

A comparison of the density, pressure and advected volume fraction of the products for the 2 cases is shown in figure 8.4 B. The plots of the 10 mm diameter case shows a steady curved detonation wave with the front near end of test cylinder (5 diameters run distance). The boundary layer is seen as a lag in the fully burned volume products (indicating the end of the hotspot reaction) relative to the lead shock front in the pressure and density plots. This implies a much lower hotspot burn rate in the boundary layer.

In contrast, the plots of the pressure and density of the 8 mm diameter case shows that the detonation front has shrunk to less than half the cylinder radius after propagating only 2.5 diameters. Moreover, the plot of the volume fraction of the burned products, which is advected with the flow, shows that the detonation wave failure started at the HE boundary and propagates radially inward. Furthermore, after a few more mm of run the detonation reduces to a weak shock in the neighborhood of the axis, which then decays since it is unsupported.

The failure diameter is for the same geometry and boundary condition as for the diameter effect; namely, an unconfined cylindrical rate stick. Failure thickness is the analogue of failure diameter for a 3-D HE slab with a rectangular cross section. In general,

$$\text{(failure thickness)} < \text{(failure diameter)} \tag{8.2}$$

due to the smaller front curvature for a detonation wave when the slab thickness is the same as the cylinder diameter.

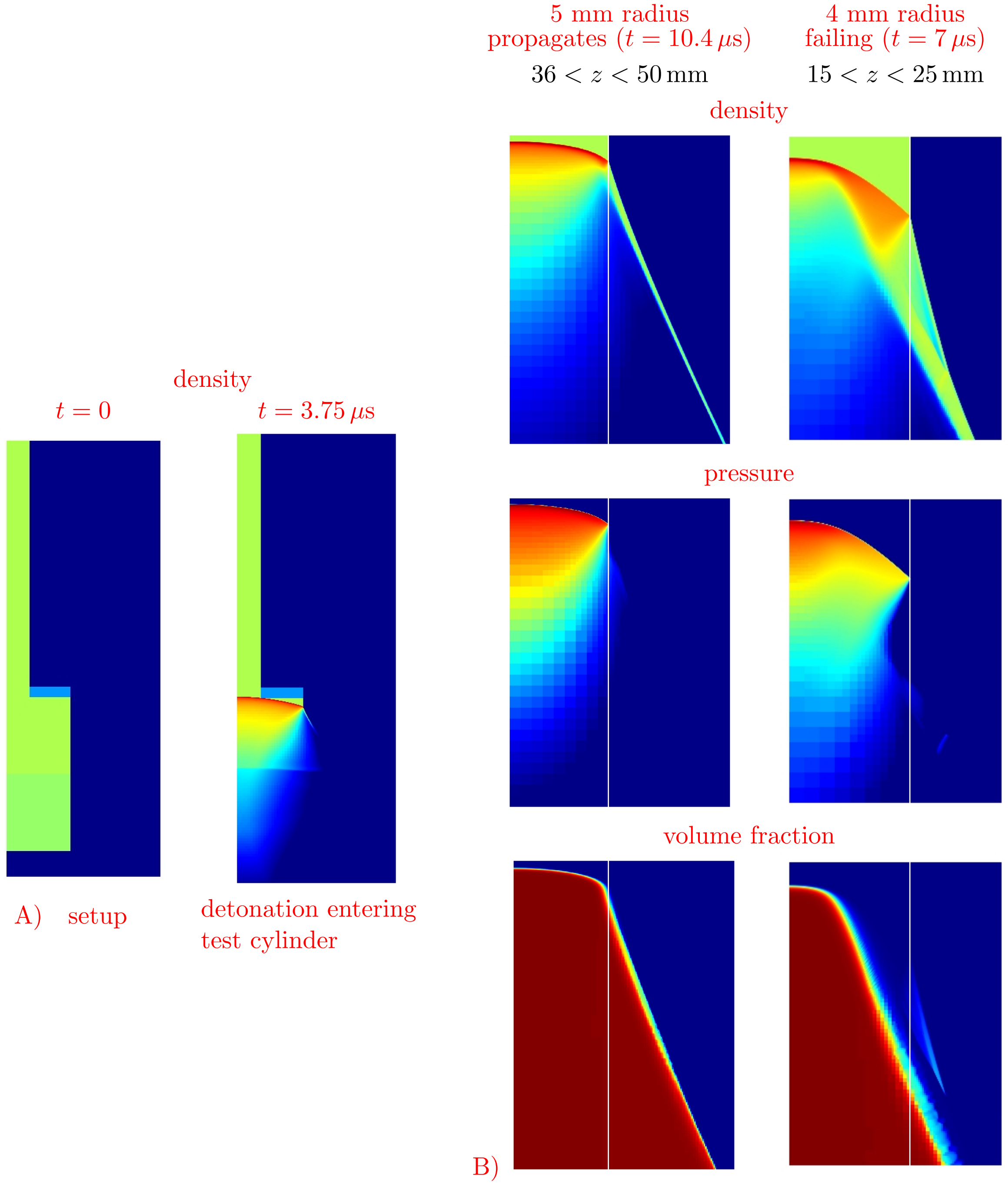

Figure 8.4: PBX 9502 rate stick simulations with diameters just above and just below the failure diameter. A) shows setup and detonation wave at the start of the narrower HE test cylinder. Test cylinder is 5 diameters long. Origin (z=0) shifted to start of test cylinder. B) shows comparison of density, pressure and volume fraction of the products when detonation wave has propagated partly up the test cylinder. White guide lines denote the initial radius of HE test cylinders. For more details see [Menikoff, 2017a].

Failure to propagate a detonation wave also depends on confinement. Stronger confinement (such as a metal instead of air) would have a boundary angle (angle between shock front and interface) closer to 90 degrees, a smaller curvature effect, and a smaller failure diameter. However there is an important caveat. Namely, small gaps, on the order of the reaction-zone width, would decrease the effective confinement. An example, discussed in a later section, is the assembly tolerances for the cylinder test.

8.2.1 Mesoscale structure within failure diameter

Figure 7.1 indicates the failure diameter of PBX 9501 is less than 1.6 mm. Within that small diameter, as can be seen in the micrograph shown in figure 8.5, there is a fairly large number of grains. However, there are regions with a few large grains and regions with more than the average binder. Near the boundary, one can expect statistical variations to give rise to larger than normal fluctuations in the reaction-zone width. Very likely some fluctuations in the neighborhood of the boundary can be large enough to cause localized failures, which subsequently reignite due to adjacent detonation wave. In general, one can expect these fluctuations to have a larger effect near an ignition threshold, such as the failure diameter. Possibly the change in behavior (large slope) of the diameter effect curve near failure, as seen in figure 7.1, is due to the fluctuations.

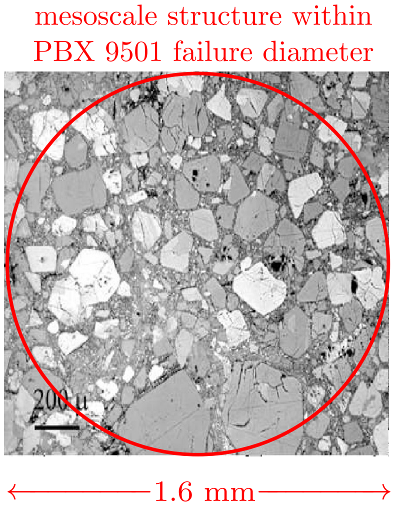

Figure 8.5: Polarized light micrograph for PBX 9501, Skidmore et al. [1998, fig 4]. Diameter of red circle corresponds to failure diameter.

8.3 Corner turning & dead zone

Corner turning occurs when a detonation wave diffracts around a corner. This leads to a divergent flow that lowers the lead shock pressure as it turns the corner. This results in a region that is shock desensitized. The desensitized region can have a very low burn rate and only a small amount of burning occurs in the time it takes the detonation wave to build up and propagate around the corner. The region of low burning is known as a dead zone.

8.3.1 Experiment

An illustrative example of corner turning with a dead zone is shown by the sequence of Phermex radiographs in figure 8.6. Since Phermex only gives 1 dynamic radiograph per shot, 3 shots with different delay times for the radiograph relative to the detonators are used to show the time evolution of a detonation wave in PBX 9502 as it turns a corner.

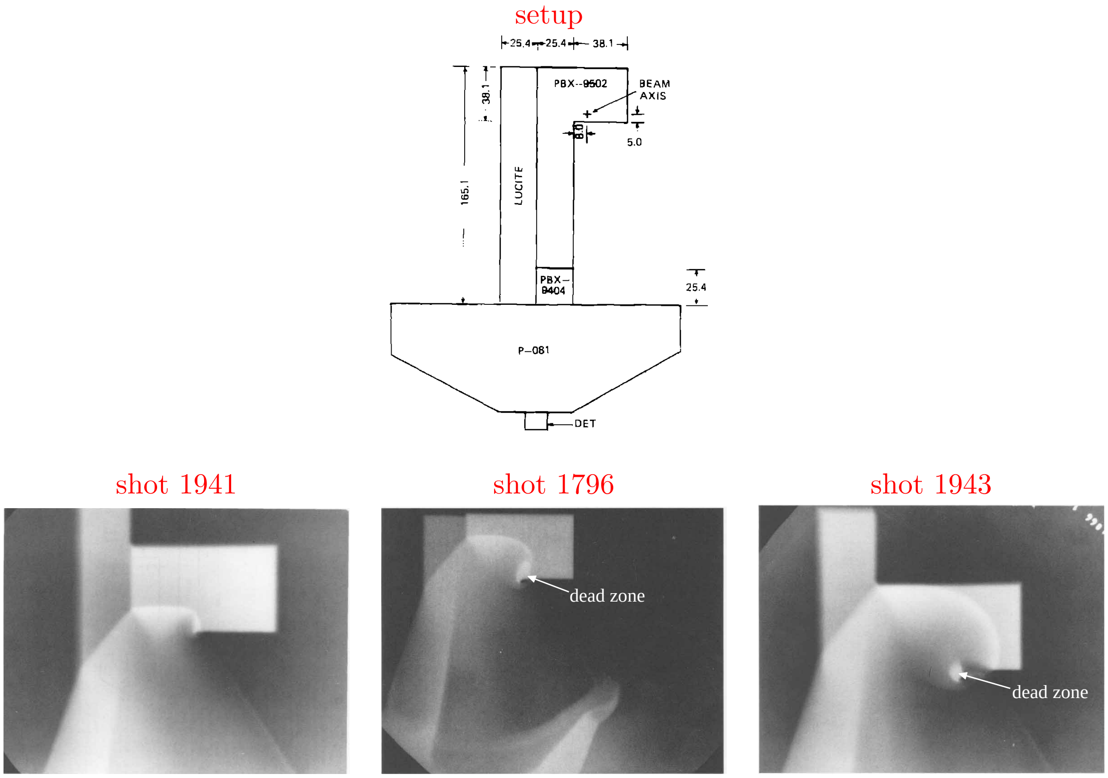

Figure 8.6: Phermex radiographs for shots # 1796, 1941 and 1943 [Mader, 1979] showing corner turning of a detonation wave in PBX 9502.

The radiographs are like photograph 'negatives'. The brighter regions have a higher density. The bright curves in the wider HE slab at the top of the radiographs correspond to the shock/detonation front. The bright spot behind the detonation front in shot 1943 is a dead zone. Its density is high compared to the surrounding product which have expanded due to their high burn temperature.

8.3.2 Simulation

The initial configuration for a simulation similar to the Phermex experiment is shown in figure 8.7. A macroscopic hotspot is used to initiate a detonation wave at the bottom of the narrow PBX 9502 cylinder. The detonation wave propagates up the narrow cylinder into a wider cylinder of PBX 9502. This is a simplification of a detonator/booster/main charge system in which the same HE is used for the 3 parts. Physically, the hotspot used to initiate the system may correspond to an exploding bridge wire.

Plots of density, pressure and burn fraction at 3 selected times are shown in figure 8.8. The main features of the evolution during the corner turning are as follows:

Fig 8.8.A shows the start of the corner turning. The detonation wave continues to propagate upward, and a weak shock is propagating laterally parallel to the bottom HE interface. Since the burn fraction is advected, it shows up below the bottom interface due to the expansion of the detonation products from the narrow cylinder.

Fig 8.8.B shows shows that the detonation wave is curling around the lateral shock. The burn fraction plot shows there is little burning behind the weak lateral shock (shown in density and pressure plots) due to shock desensitization.

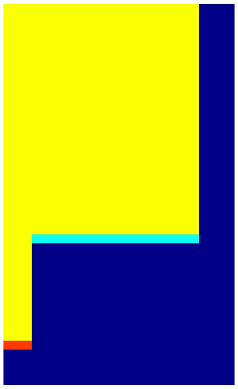

Figure 8.7: Density plot at $t = 0$ showing the initial configuration for a corner turning simulation. Yellow is PBX 9502, red is macroscopic hotspot that initiates the detonation wave, turquoise is PMMA backing, and blue is air. Left boundary is cylindrical axis.

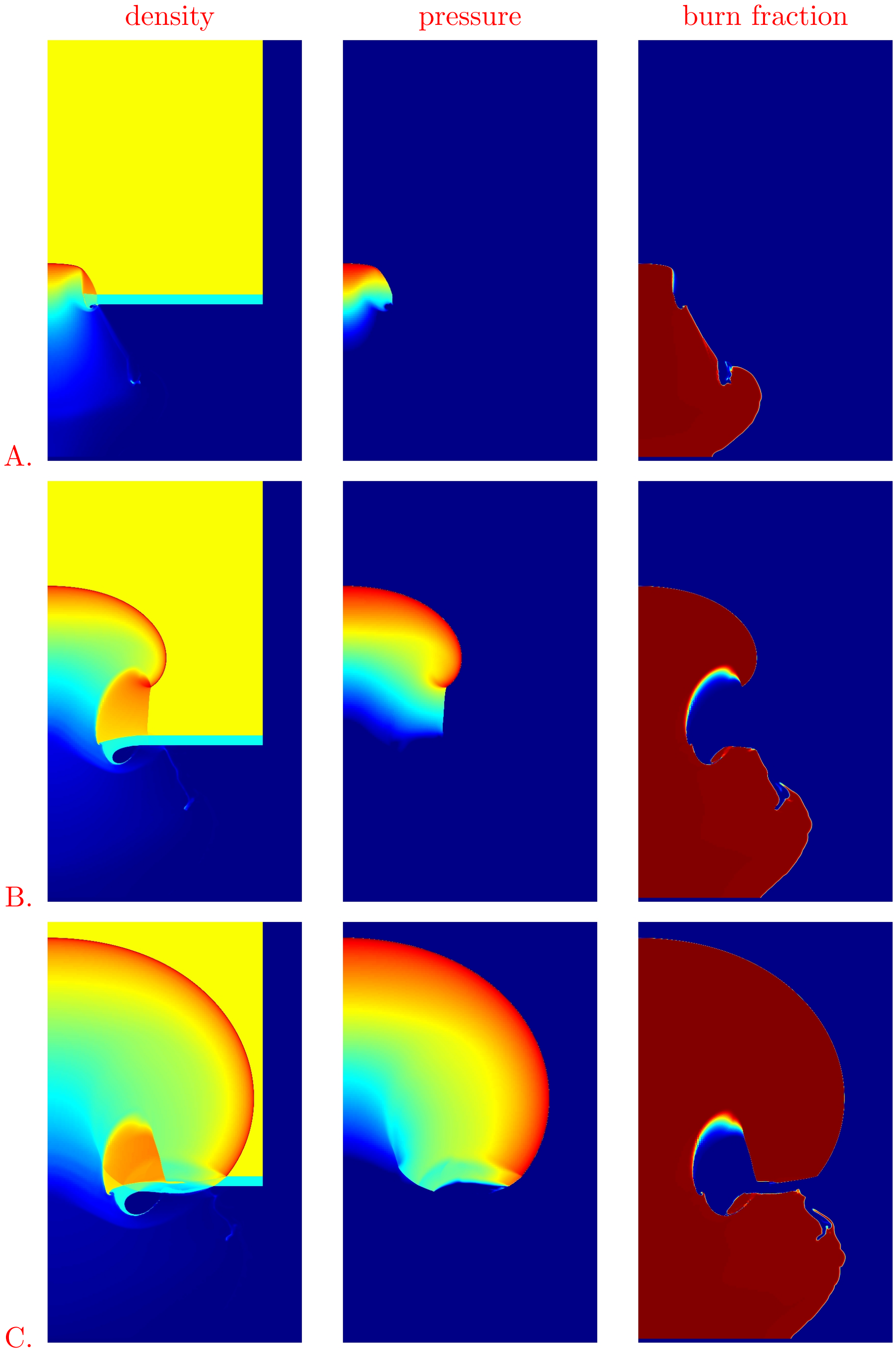

Figure 8.8: Time sequence of 2-D plots of density, pressure and advected burn fraction as detonation wave diffracts around a corner. At the last time, the dead zone is high density region behind detonation front that has not burned.

Fig 8.8.C shows the detonation wave has gotten ahead of the lateral shock, leaving behind a dead zone. Due to the boundary condition with the inert material, the detonation speed D_n at the boundary is less than the speed D_n along the cylindrical axis.

We note that corner turning involves the three physical effects for ignition: pressure gradient behind lead shock, reaction source term and curvature source term for diverging detonation wave.

We also note that neither programmed burn nor DSD are intended to be used for either ignition or the formation of dead zones. A reactive burn model is needed to simulate corner turning. Though with a burn rate sensitive to pressure, simulations may get qualitative features of dead zones without explicitly modelling shock desensitization.

Part IV

HE model calibration

CHAPTER 9

EOS model calibration

A reactive burn HE model consists of an EOS for the reactants, an EOS for the products and a burn rate. We note that the EOS models for both the reactants and products are largely independent of the initial HE state. In contrast, for most HE models, the calibration of the burn rate to shock initiation data and curvature effect data are for a specific initial density and initial temperature.

The pressing density of a PBX can be accounted for by using a reactants EOS at the theoretical maximum data (TMD) and a porosity model with initial porosity $= 1 - \rho_0/\rho_{TMD}$, where ρ_0 is the pressing density. For shock initiation, the initial shock pressure is typically greater than a few GPa, while the crush-up pressure is only a few tenths of GPa. Consequently, the porosity is compressed out by the initial shock and a crude porosity model can be used. We note that the initial density (and hence initial porosity) is affected by the initial temperature due to thermal expansion; see for example [Skidmore et al., 2003]. Also, it is important that the reactants EOS be consistent with the initial shock pressure for SDT experiment data; *i.e.*, the impedance match shown in figure 5.3.

The HE products are expected to be in thermodynamic equilibrium. Consequently, the products EOS should depend on the equilibrium concentrations of the products species and not on the initial HE state. It is important that the energy origins of the reactants EOS and products EOS be consistent with chemical energy release; see section 2.2.

Moreover, the products EOS can be calibrated to the CJ state for one initial reactants state (density and temperature). For other initial reactants states, the CJ state follows from the Hugoniot equation (3.10). Linearizing the Hugoniot equation about the CJ state determines the detonation speed for other initial reactants states; see Eq. (3.16). Whether a homogenized products EOS is necessary to account for reaction-zone fluctuations from local variations in the heterogeneities, see sections 3.3 and 4.3, is an open question.

Most analytic models for a complete thermodynamically consistent reactants or products EOS use a Mie-Grüneisen form [see for example, Menikoff, 2016]

$$P(V,e) = P_{ref}(V) + \tfrac{\Gamma(V)}{V}\big[e - e_{ref}(V)\big] \tag{9.1a}$$

with an isentrope for the reference curve. From thermodynamic identities,

$$e_{ref}(V) = e_0 - \int_{V_{ref}}^{V} P_{ref}(V')\, \mathsf{d}V' \tag{9.1b}$$

$$T_{ref}(V) = T_0 \exp\Big[-\int_{V_0}^{V} \tfrac{\Gamma(V')}{V'}\, \mathsf{d}V'\Big] \tag{9.1c}$$

where $e_0 = e_{ref}(V_0)$ and $T_0 = T_{ref}(V_0)$. There are many fitting forms in the literature that can be used for the reference isentrope $P_{ref}(V)$, such as JWL, WSD, Birch-Murnaghan, Keane, Vinet, *etc.*

For simplicity, the specific heat at constant volume is typically taken to be constant. Though not correct, it is used in conjunction with empirical burn models for which the burn rate depends only on the pressure. Moreover, the effective temperature (homogenized not physical) only enters into the P-T equilibrium mixture EOS. In this case, the temperature is given by

$$T(V,e) = T_{ref}(V) + \big[e - e_{ref}(V)\big]/C_V\ . \tag{9.2}$$

Calibrating an EOS model requires determining values for fitting parameter to get the best match with selected experimental data. Both shock wave data and rarefaction wave data are used for calibrating EOS models. For a rarefaction wave, experiments can measure with PDV probes the Lagrangian time history of the particle velocity at an interface with a window. In contrast to shock wave data, a hydro simulation corresponding to a rarefaction wave experiment is needed to determine the thermodynamic state variables (V, e, P) for points on the rarefaction locus. Consequently, hydro simulations are needed to calibrate an EOS model to rarefaction wave data. Velocity measurements for neither a shock nor a rarefaction yield data on the temperature.

We note that model EOS may have a limited domain. This can be an issue for solid EOS that are developed for compression. Typically, at low pressure and expansion, $V > V_0$, the isothermal bulk modulus can go negative and the EOS becomes thermodynamically unstable. When this occurs for the reactants, the partly burned P-T equilibrium mixture EOS either fails to exist or is not unique. In a simulation, this can occur when a detonation wave impacts a free surface (or low density gas such as air) and the hot mixture in the reaction zone expands to a low pressure.

Instructive examples that describe the EOS calibration procedure in some detail can be found in [Wescott et al., 2005] for PBX 9502 and [Aslam et al., 2020] for PBX 9501. Next we go over the types of experimental data that can be used (when available for PBX of interest) for calibrating reactants EOS and products the EOS.

9.1 Reactants EOS data

For the reactants, shock data is available from SDT experiments with embedded magnetic gauges; see section 5.1.3. Shock data points are limited in pressure due to reaction affecting the measurement of the particle velocity. Though not typically done, higher pressure shock data points can be measured with 'Front Surface Impact Experiments' in which a projectile with the PBX impacts a window with a VISAR probe to measure the interface velocity before the reaction becomes significant; [see figs 2 and 4, Sheffield et al., 2004]. (This technique has also been called reverse impact experiments.) In principle, higher pressures with minimal reaction can be achieved by taking advantage of shock desensitization; for example by utilizing double shock experiments as shown in section 5.3.1.

Without high pressure data, the reactants' EOS is an extrapolation that depends on the fitting form used for the model EOS. As previously noted, the reactants' shock locus and the products' detonation locus are not expected to cross. This places a constraint on the reactants' EOS at high pressure.

High pressures without reaction can also be obtained with isothermal compression experiments using a diamond anvil cell and powder diffraction; see for example [Yoo and Cynn, 1999]. However, these experiments only give the compression isotherm $P(V)$ and not $e(V)$. Consequently, isothermal compression data is not used in the calibration of the reactants EOS.

We note that up to the CJ pressure, the entropy change across a shock is relatively small. Consequently, in the (V, P)-plane the principal isentrope and principal shock locus are close. With only shock data points on the principal shock loci, the EOS calibration is relatively insensitive to Γ. That is, if Γ is changed then the parameters for the reference isentrope can be changed to compensate and still fit shock data points within their uncertainty. Consequently, for an EOS calibration, the parameter Γ can have a large uncertainty. For hydro simulations using a Mie-Grüneisen EOS, the uncertainty in Γ only makes a significant difference when the flow is sufficiently far from the reference isentrope. In principle, $\Gamma(V)$ can be determined for a PBX from the measured shock loci at 2 different pressing densities.

For a molecular solid, such as HE grains in a PBX, the specific heat is due to molecular and lattice vibrations, which can be collectively referred to as the phonon spectrum; see for example, [Menikoff, 2014b]. We note that the phonon spectrum can be determined from Raman spectroscopy and infrared absorption experiments or computationally from density functional theory(DFT). At higher temperature, more phonon modes are excited and the specific heat increases until it saturates at the 'classical limit', *i.e.*, the value from the law of Dulong-Petit. As an illustrative example, for the HMX based PBX 9501, the specific heat increases by a factor of about 2 between room temperature and the VN state temperature. For temperature based burn rates, the assumption of constant specific heat in Eq. (9.2) is not adequate. There are semi-analytic EOS which extend the Mie-Grüneisen EOS to better account for the temperature dependence; see for example [Menikoff, 2009]. Models with better thermal properties are more complicated and generally not used for HE models with burn rates dominated by pressure. We note that the calibration of the Mie-Grüneisen pressure, Eq. (9.1a), does not depend on the thermal part of the EOS.

We also note that molecular dynamics (MD) calculations can provide data for calibrating material properties, especially in the regime of high pressure and high temperature for which experimental data are not available; see for example [Bedrov et al., 2000], [Nguyen et al., 2024], [Cawkwell et al., 2008], [Kroonblawd et al., 2024].

9.2 Products EOS data

For applications, the CJ release isentrope is important. Frequently, 'Cylinder Test' data [Kury et al., 1965, Lee et al., 1968] are used to calibrate the release isentrope for $P < P_{CJ}$. Then a Mie-Grüneisen form of EOS, Eq. (9.1), can be constructed for the products with the CJ release isentrope as the reference curve. Alternatively, 2 variations of the cylinder test, the 'Sandwich Test' [Hill, 2001] and the 'Disc Acceleration Experiment' (DAX) [Lorenz et al., 2015], can be used for release isentrope data. The next subsection describes the cylinder test in more detail.

The Mie-Grüneisen form can be extended to give the temperature. However, there is little temperature data to calibrate the thermal component of an EOS model. Typically, the products temperature enters a reactive HE model only through the mixture EOS for partly burned HE, see section 2.1, and is accounted for by the calibration of the empirical burn rate.

Points on the overdriven planar detonation locus provide EOS data at higher pressure, $P > P_{CJ}$. The Grüneisen Γ is needed to extrapolate (in e for fixed V) the CJ release isentrope to the detonation locus. Also, measuring the particle velocity for the release isentrope from a point on the overdriven detonation locus [see for example, Hixson et al., 2000] provides data for calibrating the products EOS at $P < P_{CJ}$. Comparing data points at the same V from 2 release isentropes can be used to determine the Grüneisen coefficient from the thermodynamic relation $\Gamma = V(\partial_e P)_V$. However, due to limited precision of the release wave data points and truncation errors for finite difference evaluation of Γ, there can be large uncertainty in Γ. Using a fitting form to smooth the data may circumvent the limited precision and improve the accuracy.

The products EOS determines the CJ state. The detonation speed and pressure can be inferred from experimental data in several ways. This can be used as either a consistency check on the calibrated EOS or the values of D_{CJ} and P_{CJ} can be used as constraints to fine tune the EOS. This is further discussed in a later subsection on the CJ state.

Alternatively, thermochemical codes can be used to generate a products EOS; see for example [Fried et al., 2002, Ticknor et al., 2020] and references therein. Thermochemical codes calculate the equilibrium composition of products species by minimizing the Gibbs free energy (including entropy of mixing for gaseous product species) and then constructs a mixture EOS based on P-T equilibrium of the product species.

Since the EOS generated by a thermochemical code is based on a thermodynamic potential, Gibbs free energy $G(P,T)$, they provide a thermodynamically consistent complete EOS. The inversion of independent variables from (P,T) to (V,e) is straight-forward. Hence, the thermochemical EOS provides both $P(V,e)$ and $T(V,e)$. Moreover, the thermochemical EOS does not necessarily have the constraints of the Mie-Grüneisen form of EOS. However, a thermochemical EOS may need to be fine-tuned to improve the agreement with experimental data; particularly, the CJ detonation speed and the release isentrope.

For efficient EOS evaluation in a hydro code, typically the thermochemical products EOS is either represented in a tabular form (such as a SESAME EOS table) or fit to a simple analytic EOS that is usually of the Mie-Grüneisen form.

9.2.1 Cylinder test experiment

The cylinder test consists of a cylinder of PBX surrounded by a thin walled copper tube. The PBX is detonated at one end and a detonation wave propagates up the cylinder causing the wall to expand outward. After a steady state is reached, the detonation speed is measured with timing pins, and the wall velocity with either PDV probes or a streak camera, as shown in figure 9.1 . The wall velocity data is used to calibrate the products release isentrope, which is then used as the reference curve for a Mie-Grüneisen form of EOS.

For the standard configuration, see [Lee et al., 1968, fig 4] and [Catanach et al., 1999], the PBX diameter is 1 inch, the wall thickness is 0.1 inch and the length of the cylinder is 10 to 12 inches. The PBX is machined in 2 inch long cylindrical pellets, which are then coated with grease or mineral oil and inserted into the copper tube. The pellets allow for an interference fit with tight tolerances on the dimensions. The tolerances are such that the mass/length of the PBX and the copper tube are constants to within 0.1 percent. This minimizes the uncertainty in the data. In addition, the copper tube is heat treated to ‘dead soft’ in order to maximize its ductility. This allows the wall to expand further radially before fracturing.

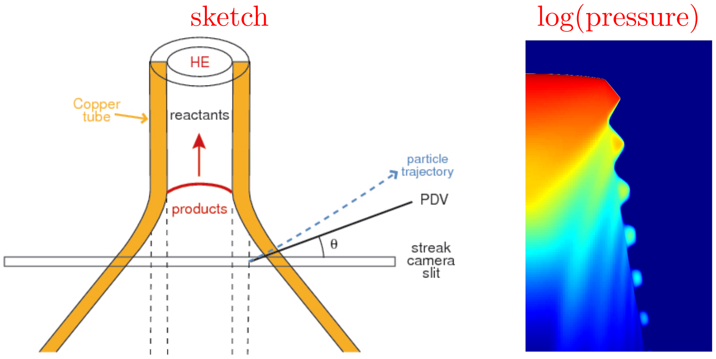

Figure 9.1: Sketch of cylinder test on left with either streak camera or PDV probe to measure 'wall velocity'. Right is 2-D plot of $\log(P)$, from a simulation, showing detonation front and ringing in the copper tube wall.

Old experiments used a streak camera to measure the wall radius along a fixed diameter, $r(t)$, and hence the wall velocity, $u_w(t) = \mathsf{d}r/\mathsf{d}t$. Newer experiments use PDV probes to measure the component of the wall velocity directed along the fiber optic probe. Multiple probes provide a consistency check that the detonation wave has achieved a steady state (constant detonation speed and wall velocity independent of length of run), and that the flow is axial symmetric (wall velocity independent of azimuthal angle of the probe). Alternatively, the redundant diagnostics can be used to estimate the uncertainty in the velocity data.

The measured 'wall velocity' for the two diagnostics are each phase velocities, and not a Lagrangian particle velocity of a point on the wall. The phase velocities are slightly different and their values can differ by a couple of percent. For steady state, the two phase velocities can be related; see for example, [Menikoff et al., 2013]. To calibrate the release isentrope or compare with different experiments, it is important that the matching phase velocities be used.

9.2.2 Cylinder test uncertainty

Illustrative examples of the measured wall velocity are shown in figure 9.2. The oscillations in the velocity are due to ringing of the wall. That is, compressive/rarefaction waves reflecting off the wall interfaces as seen in the pressure plot in figure 9.1. The frequency of the ringing depends on the wall thickness and the longitudinal wave speed, which depends on the shear modulus as well as the EOS of the copper. In addition, the decrease in the wall velocity upon wave reflection from the free surface of the wall implies that the wall goes into tension. Consequently, simulations of the cylinder test require a strength model for the copper tube. We also note that by measuring the velocity directly, the PDV data is more accurate for the ringing than the streak camera data.

Since the first ring or velocity drop occurs over a time much greater than the reaction time, the wall velocity of a simulation is insensitive to the burn rate, and a programmed burn model is often used. The flip side is that the wall velocity does not give detailed information for the products release wave pressure in the range between P_{CJ} and the pressure at the first ring. That is, the wall velocity in this regime is dependent on the strength model of the copper. For PBX 9501, this is roughly the pressure range $20 < P < 35\,\mathrm{GPa}$.

PBX 9502 displays an anomalous structure of the velocity at the first ring. It is likely due to spall from the interaction between two rarefaction waves; outgoing rarefaction from the impedance match with the detonation wave reaction-zone profile, and incoming rarefaction from reflection of first copper shock off the free surface. After the first ring any gap from spall would close up due to the PBX pressure accelerating the wall outward.

As the wall expands, the pressure in the copper tube drops. Moreover, the heating of the copper wall is small. Consequently, for large expansion, the wall thickness is proportional to 1/radius. At some point the thinning of the wall causes it to fracture, which limits the time domain for useful data. For PBX 9501, $15\,\mu$s after the shock arrival, the wall expansion is $R/R_0 \approx 3$. This corresponds to an expansion ratio of $V/V_0 \approx 7$ and pressure of a few tenths of GPa. This expansion gives information about the useful energy that can be extracted from PBX 9501. The fact that the wall is still accelerating outward, implies that there is chemical energy left behind.

In summary, the wall velocity provides data for calibrating the products EOS along the CJ release isentrope to an expansion of about 7. Figure 9.2 shows that the PDV wall velocity for repeated PBX 9501 experiments agrees to within 1 percent, and for PBX 9502 to about 2 percent. We note that the calibration simulations require an EOS and strength model for copper. The calibrated isentrope would be more accurate with additional data on the CJ pressure and the Grüneisen coefficient.

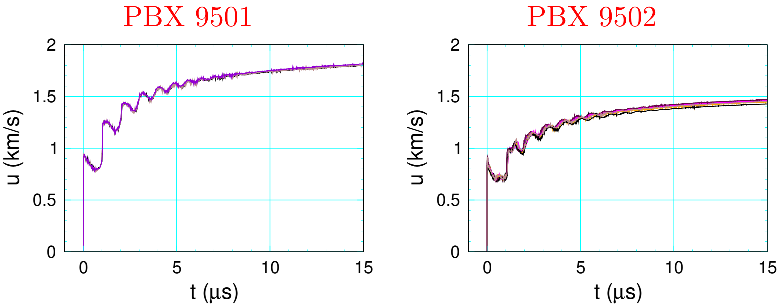

Figure 9.2: Wall velocity plots of PDV data for PBX 9501 [Pemberton et al., 2011b] and PBX 9502 [Pemberton et al., 2011a]. PBX 9501 plot shows 3 probes on duplicate shots. PBX 9502 plot shows 8 probes on the same shot at different azimuthal angles and axial positions.

9.3 CJ state

The same techniques used to determine a shock state can be applied to a detonation wave. However, there are 2 complications. First, the shock jump conditions only apply to planar detonation waves. Second, the state behind an underdriven detonation wave is not constant since the reaction-zone profile is followed by a rarefaction wave. For the CJ state, the question arises as to where the reaction zone ends and the rarefaction begins. In principle, the particle velocity profile has a sharp kink at the CJ point, see figure 4.2. However, experiments show that the kink is smoothed out as seen in the measured time histories of the ZND profile discussed in section 4.3.2 . From the jump conditions, the shock pressure is given by $P_s = \rho_0 u_p u_s$, and the uncertainty in u_p at the end of the reaction zone can give several percent uncertainty in the detonation pressure.

The following subsections discuss techniques that have been used to determine the CJ detonation speed and the CJ pressure.

9.3.1 CJ detonation speed

There are two techniques for measuring the CJ detonation speed. First, as discussed in section 7.1, the diameter effect can be extrapolated to the planar limit using Eq. (7.1). The rate stick detonation speed data needs to extend to large enough diameter that the asymptotic limit applies. Data usually extends to a 2 inch diameter rate stick.

Figure 9.3 show a notable example where 2 inch diameter data is not in the asymptotic limit. Extrapolating from the largest 2 diameters yields the following:
9.3.A extrapolating 0.5 to 2 inch diameter ⇒ $D_{CJ} = 7.70\,\text{km/s}$
9.3.B extrapolating 2 and 4 inch diameter ⇒ $D_{CJ} = 7.78\,\text{km/s}$
The difference in D_{CJ} is 1 percent. Possibly this is due to the slow carbon clustering reaction of TATB.

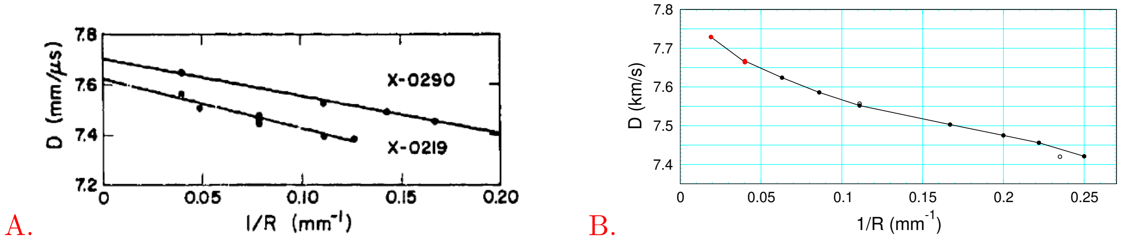

Figure 9.3: Diameter effect data for PBX 9502. A. plot from [Campbell and Engelke, 1976] fig 5a; X-0290 is development explosive renamed PBX 9502. B. plot uses data in [Campbell, 1984] table 2.

The uncertainty in the rate stick detonation speed measurement is a few tenths of a percent. This is much better than would be expected from variations in the reaction zone heterogeneities (see section 3.3) and the ZND profile measurements (see section 4.3.2). A likely explanation is that the timing pins for the rate stick experiments are several cm apart. The detonation speed from a least squared fit to the timing pins effectively filters out short wavelength fluctuations. That is say, on average the detonation speed is nearly constant, but the instantaneous detonation speed would have variations with a wavelength on the scale of the reaction-zone width.

The second technique for measuring the CJ detonation speed is to use a flyer plate with a hi/low acoustic impedance, driven by a plane wave lens, to promptly initiate a planar detonation wave; see short shock loading conditions in section 5.3. Then after a sufficient length of run to reach a steady underdriven detonation, the CJ detonation speed can be measured with timing pins. The difficulty is maintaining the planarity of the detonation wave over a long enough distance of run for an accurate measurement of the detonation speed. Consequently, this technique has not been used.

9.3.2 CJ pressure

Techniques to give higher accuracy of the CJ pressure than from the direct measurement of the ZND profile (±1 to 2 percent) involve extrapolating either up from the release isentrope or down from the overdriven detonation locus. The extrapolations require multiple experiments to determine the CJ pressure.

Extrapolating release wave

The first technique, developed by Duff and Houston [1955] and Deal [1957], is aimed at conventional high explosives with a thin reaction-zone width. The experiments utilize a large diameter cylinder of PBX. The PBX is initiated with a plane wave lens on one end. The other end has an aluminum plate. The free surface velocity of the plate is measured for a series of experiment which vary the length of the aluminum plate. We note that each experiment is similar to a ZND profile experiment with the window replaced by an aluminum plate and the PDV probes replaced by the free surface velocity measurement. Though primitive by today's standard, this technique was the state of the art when developed in 1955.

The idea is that the detonation wave drives a shock into the Al, which then decays with fast and slow time constants. The fast decay is due to the unsupported steep gradient from the impedance match with the reaction-zone profile. The second slower decay is from the impedance match with the release wave. When the plate thickness is much larger than the reaction-zone width, effectively the reaction zone can be neglected and the detonation wave treated as a shock-like discontinuity to the CJ state.

When the free surface velocity is extrapolated to zero plate thickness, the release wave can be neglected. With a previously determined EOS for the Al, two impedance matches are used to determine the CJ pressure. First, the free surface velocity determines the strength of the Al shock driven by the detonation wave. Second, the impedance match of the detonation wave into the Al, with specified shock strength, determines the CJ pressure; see [Deal, 1957] fig 3 and Eq 3. The reported error bar in P_{CJ} is about 1 percent, ibid table II.

A natural question is why the extrapolation of the free surface velocity is more accurate than picking the CJ particle velocity from a ZND profile measurement. We note that shock waves are very stable. Very likely, as the aluminum shock propagates, it smooths out short wavelength variations imprinted from the impedance match with the detonation wave. It also maybe related to the large diameter cylinders enabling the detonation wave to have a larger distance of run before the measurement.

Fitting overdriven locus

Another technique for determining the CJ state is to extrapolate overdriven detonation locus down to the minimum detonation speed. This takes advantage of the fact that overdriven detonation waves are shock-like. For simple impact experiments, the particle velocity is constant behind the reaction zone and not subject to ambiguity from a rarefaction behind the underdriven detonation wave.

The idea is to determine the particle velocity u_{CJ} by calibrating a fitting function for the detonation speed, $D(u)$, to detonation locus data points and subject to the constraint for the sonic condition that D_{CJ} is the minimum detonation speed. Hence, $\mathsf{d}D/\mathsf{d}u = 0$ at $u = u_{CJ}$. Then from the shock jump conditions the CJ pressure is $P_{CJ} = \rho_0 u_{CJ} D_{CJ}$.

As an illustrative example, figure 9.4 shows data points for the PBX 9502 detonation locus. We note that there is a scatter in the data and that the lowest data points have a detonation speed less than D_{CJ}, based on extrapolating rate stick data; see subsection 9.3.1 . This is due in part to uncertainty in the measurements (see error bars for red data points), and to measuring the detonation speed before the detonation wave reached steady state, as fig 2 in [Gustavsen et al., 2014] shows the reaction-zone width increasing with run distance.

For a CHE, a detonation wave when initiated with a shock at the CJ pressure is expected to promptly reach steady state. In contrast, PBX 9502 has a slow reaction due to carbon clustering and takes longer to reach steady state.

Since the detonation locus and the CJ release isentrope join up with continuous derivative, $\mathsf{d}P/\mathsf{d}V$, a more accurate value of P_{CJ} is expected from calibrating a model EOS to data from both the overdriven detonation locus and a 1-D release isentrope from an overdriven detonation state; see for example [Tang et al., 1998].

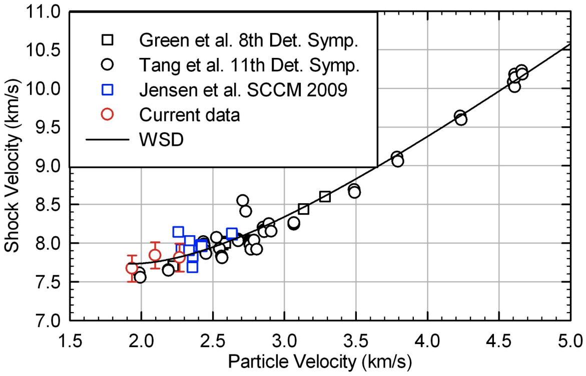

Figure 9.4: Overdriven detonation locus for PBX 9502 from Gustavsen et al. [2014, fig 4]. Black curve is detonation locus from products EOS of Wescott et al. [2005, §IIB].

CHAPTER 10

Rate model calibration

As previously noted, the burn rate for reactive burn models is empirical. Here we discuss general issues with calibrating the burn rate.

Calibrating a burn rate involves several steps:

1. Choosing a functional form for the burn rate.
   The burn rate accounts for the effect of inhomogeneities in a PBX (variations in grain size, pore size and binder thickness) on the hotspot burning. Heuristics such as the ignition & growth concept of hotspots (discussed in chapter 6) are often used to motivate the functional form (fitting parameters and model dependent state variables such as one or more reaction progress variables). Due to the heuristic motivation, the functional form is partly subjective.

   Typically, calibration data is from simple experiments aimed at a single phenomena. An example is a 1-D shock-to-detonation transition experiment. There are applications that combine detonation phenomena, such as a detonator/booster system for which corner turning, a diverging detonation wave and a pressure gradient behind the detonation front all occur. To the extent that the evolution of the hotspot distribution in the more complicated case is similar to that in the calibration experiments, one can expect the burn rate model to work well. In other words, the functional form for the burn rate is important for extending the range of applicability beyond that of the experiments used to calibrate the burn rate.

   We note that an HE model is often associated with the functional form for the burn rate model. This is somewhat misleading. While in principle any EOS model can be used with any burn rate model, changing the EOS model requires the rate model calibration; the two are linked and can not be used independently. Moreover, if simulations for two HE models differ, the difference can be due to either different rate models or different EOS models, or a combination of the two.

2. Choosing data for the physical phenomena to be fitted.
   The important phenomena are shock initiation discussed in chapter 5, propagation of curved detonation waves discuss in chapter 7, and failure diameter and corner turning discussed in chapter 8. The choice of experimental data for these phenomena to use in the rate model calibration is subjective. One should also be cognizant of the lot variability.

3. Choosing a metric for goodness of fit for comparing experimental to simulated data.
   One needs both a metric for each type of data, and a metric or weights to combine all the data used for the fit. These metrics are partly subjective.

4. Iteration scheme to find parameters that minimize the metric.
   Depending on the fitting form, the fit may be highly non-linear. In addition, if the data is insufficient in some regions of parameter space, there can be correlated changes in fitting parameters that have a small effect on the metric. This can lead to issues with the convergence of the iteration scheme. There also is the issue of finding a global versus a local minimum of the metric.

Since the burn rate is empirical, uncertainties in the calibration data will limit the accuracy of any HE model. There are several types of uncertainty. First, there is the scatter in the data as exemplified by the PBX 9502 Pop plot shown in figure 5.6, and the PBX 9502 overdriven detonation locus shown in figure 9.4. Second, there are systematic differences in the data due to the variation of heterogeneities as exemplified by the lot dependence of the cold PBX 9502 Pop plot as shown in figure 5.11. Third, there is a high sensitivity of detonation data to small changes in initial density as exemplified by the PBX 9501 Pop plot shown in figure 5.13.

The differences in data from the second and third cases can be accounted for by calibrating the burn rate for specified initial conditions. In effect, this would treat a PBX for each lot and each initial density as a distinct explosive. Considering the data needed to calibrate a burn rate, this would be very expensive. There is some work in ‘mesoscale informed modeling’ that aims at predicting the change in the burn rate parameters with the initial state of a PBX.

There is also an issue with numerical resolution for the simulations used to evaluate the metric for fitting experimental data. An example is the curvature effect for the cylinder test; the variation of the detonation speed with the cell size as shown in figure 7.2. An accurate numerical detonation speed for a curved detonation front requires a fine resolution when the physical reaction-zone width is small. This raises an important issue for the calibration simulations. Is it necessary to have a fully converged solution for evaluating the metric when the required resolution is not feasible for the intended model applications? Or is it better for the calibration to use the same resolution as will be used for simulations of an application?

Bibliography

J. Akhavan. *The Chemistry of Explosives*. Royal Society of Chemistry, 2004. URL `https://pubs.rsc.org/en/content/ebook/978-1-83916-446-0`.

T. Aslam, R. Gustavsen, N. Whitworth, R. Menikoff, C. Tarver, C. Handley, and B. Bartram. Shock, release and reshock of PBX 9502: Experiments and modeling. In *AIP Conference Proceedings*, volume 1979:100001, 2018. URL `https://doi.org/10.1063/1.5044873`.

T. D. Aslam. Detonation shock dynamics calibration of PBX 9501. In *Shock Compression of Condensed Matter – 2007*, pages 813–816, 2007. URL `https://doi.org/10.1063/1.2833248`.

T. D. Aslam, J. B. Bdzil, and D. S. Stewart. Level set methods applied to modeling detonation shock dynamics. *Journal of Computational Physics*, 126:390–409, 1996. URL `https://doi.org/10.1006/jcph.1996.0145`.

T. D. Aslam, R. L. Gustavsen, N. J. Sanchez, and B. D. Bartram. Double shock experiments and modeling in PBX 9502. Technical Report LA-UR-11-03754, Los Alamos National Lab., 2011. URL `https://www.osti.gov/servlets/purl/1078411`. Slides of presentation at 17^{th} APS-SCCM Conference.

T. D. Aslam, M. A. Price, C. Ticknor, J. D. Coe, J. A. Leiding, and M. A. Zonker. AWSD calibration for the HMX based explosive PBX 9501. In *AIP conference proceedings*, 2020. URL `https://doi.org/10.1063/12.0000891`.

L. M. Barker. The development of the VISAR, and its use in shock compression science. In *AIP conference proceedings*, volume 505, pages 11–17, 2000. URL `https://doi.org/10.1063/1.1303413`.

J. B. Bdzil. Fluid Mechanics of an Obliquely Mounted MIV Gauge. Technical report, Los Alamos National Lab., March 2018. URL `https://doi.org/10.2172/1429987`. LA-UR-18-22397.

J. B. Bdzil and W. C. Davis. Time-dependent detonation. Technical Report LA-5926-MS, Los Alamos National Lab., 1975. URL `https://doi.org/10.2172/5001642`.

J. B. Bdzil and D. S. Stewart. Modeling two-dimensional detonations with detonation shock dynamics. *Physics of Fluids A*, 1:1261–1267, 1989. URL `https://doi.org/10.1063/1.857349`.

J. B. Bdzil and D. S. Stewart. The dynamics of detonation in explosive systems. *Annual Rev. Fluid Mech.*, 39:263–292, 2007. URL `https://doi.org/10.1146/annurev.fluid.38.050304.092049`.

Dmitry Bedrov, Grant D. Smith, and Thomas D. Sewell. Temperature-dependent shear viscosity coefficient of octahydro-1,3,5,7-tetranitro-1,3,5,7-tetrazocine (hmx): A molecular dynamics simulation study. *J. Chem. Phys.*, 112:7203–7208, 2000. URL `https://doi.org/10.1063/1.481285`.

F. P. Bowden and Y. D. Yuffee. *Initiation and growth of explosions in liquids and solids*. Cambridge University Press, 1952.

A. W. Campbell. Diameter effect and failure diameter of a TATB based explosive. *Propellants, Explosives, Pyrotechnics*, 9:183–187, 1984. URL `http://dx.doi.org/10.1002/prep.19840090602`.

A. W. Campbell and R. Engelke. The diameter effect in high-density heterogeneous explosives. In *Proceeding of the Sixth International Symposium on Detonation*, pages 642–652, 1976.

A. W. Campbell and J. R. Travis. The shock desensitization of PBX-9404 and composition B-3. In *Eighth Symposium (International) on Detonation*, pages 1057–1068, 1986.

A. W. Campbell, W. C. Davis, J. B. Ramsay, and J. R. Travis. Shock initiation of solid explosives. *Phys. Fluids*, 4:511–521, 1961a. URL `https://doi.org/10.1063/1.1706354`.

A. W. Campbell, W. C. Davis, and J. R. Travis. Shock initiation of detonation in liquid explosives. *Physics of Fluids*, 4:498–510, 1961b. URL `https://doi.org/10.1063/1.1706353`.

R. Catanach, L. Hill, H. Harry, E. Aragon, and D. Murk. Cylinder test specification. Technical Report LA-13643-MS, Los Alamos National Lab., 1999.

M. J. Cawkwell, T. D. Sewell, L. Z., and D. L. Thompson. Shock-induced shear bands in an energetic molecular crystal: Application of shock-front absorbing boundary conditions to molecular dynamics simulations. *Phys. Rev. B*, 78:014107, 2008. URL `https://doi.org/10.1103/PhysRevB.78.014107`.

P. W. Cooper. *Explosives Engineering*. Wiley-VCH, 1996. URL `https://www.wiley.com/en-us/Explosives+Engineering-p-9781119537175`.

J. C. Dallman and J. Wackerle. Temperature-dependent shock initiation of TATB-based high explosive. In *Tenth Symposium (International) on Detonation*, pages 130–138, 1993.

D.M. Dattelbaum, S.A. Sheffield, D.B. Stahl, A.M. Dattelbaum, W. Trott, and R. Engelke. Influence of hot spot features on the initiation characteristics of heterogeneous nitromethane. In *Proceeding of the Fourteenth International Symposium on Detonation*, pages 611–620, 2010.

W. C. Davis. Shock waves; rarefaction waves; equations of state. In W. P. Walters J. A. Zukas, editor, *Explosive Effects and Applications*, chapter 3. Springer-Verlag, 1998.

W. C. Davis, B. G. Craig, and J. B. Ramsay. Failure of the Chapman-Jouguet theory for liquid and solid explosives. *Physics of Fluids*, 10:2169–2182, 1965. URL `https://doi.org/10.1063/1.1761177`.

W. E. Deal. Measurement of the Chapman-Jouguet pressure for explosives. *J. Chem. Phys.*, 27:796–800, 1957. URL `https://doi.org/10.1063/1.1743831`.

J. J. Dick, C. A. Forest, J. B. Ramsay, and W. L. Seitz. The Hugoniot and shock sensitivity of a plastic-bonded TATB explosive PBX 9502. *J. Appl. Phys*, 63:4881–4888, 1988. URL `https://doi.org/10.1063/1.340428`.

J. J. Dick, A. R. Martinez, and R. S. Hixson. Plane impact response of PBX 9501 and its components below 2 GPa. Technical report, Los Alamos National Lab., April 1998. LA-13426-MS, `https://www.osti.gov/servlets/purl/334337`.

D. H. Dolan. Extreme measurements with photonic doppler velocimetry (pdv). *Rev. Sci. Instrum.*, 91:051501, 2020. URL `https://doi.org/10.1063/5.0004363`.

R. E. Duff and E. Houston. Measurement of the Chapman-Jouguet pressure and reaction zone length in a detonating high explosive. *J. Chem. Phys.*, 23:1268–1273, 1955. URL `https://doi.org/10.1063/1.1742255`.

W. Fickett and W. C. Davis. *Detonation*. Univ. of Calif. Press, 1979.

E. G. Francois, J. S. Morris, and M. Lieber. Three dimensional hemispherical test development to evaluate detonation wave breakout. *Journal of Physics: Conference Series*, 500:142015, 2014. URL `https://doi.org/10.1088/1742-6596/500/14/142015`.

L. E. Fried, W. M. Howard, and P. C. Souers. Exp6: A new equation of state library for high pressure thermochemistry. In *Twelve (International) Symposium on Detonation*, pages 567–575, 2002.

Y. Gao, J. H.S. Lee, and H.D. Ng. Velocity fluctuation near the detonation limits. *Combustion and Flame*, 161:2982–2990, 2014. URL `https://doi.org/10.1016/j.combustflame.2014.04.020`.

T. R. Gibbs and A. Popolato, editors. *LASL Explosive Property Data*. Univ. of Calif. Press, 1980.

J. H. Goforth, E. V. Baca, M. E. Briggs, F. L. Cochran, T. A. Gianakon, B. B. Glover, D. H. Herrera, R. L. Holmes, J. L. Johnson, E. C. Martinez, R. K. Meyer, H. Oona, D. L. Peterson, P. J. Rae, C. L. Rousculp, and R. G. Watt. Improvements in ranchero magnetic flux compression generators. In *2015 IEEE Pulsed Power Conference (PPC)*, pages 1–5, 2015. doi: 10.1109/PPC.2015.7296900.

R. L. Gustavsen, S. A. Sheffield, and R. R. Alcon. Progress in measuring detonation wave profiles in PBX 9501. In *Eleventh (International) Symposium on Detonation*, pages 821–827, 1998.

R. L. Gustavsen, S. A. Sheffield, R. R. Alcon, and L. G. Hill. Shock initiation of new and aged PBX 9501 measured with embedded electromagnetic particle velocity gauges. Technical Report LA-13634-MS, Los Alamos National Lab., 1999. URL `http://dx.doi.org/10.2172/10722`.

R. L. Gustavsen, S. A. Sheffield, and R. R. Alcon. In-situ magnetic gauging technique used at LANL – method and shock information obtained. In *Shock Compression of Condensed Matter – 1999*, pages 1043–1048, 2000. URL `https://doi.org/10.1063/1.1303646`.

R. L. Gustavsen, R. J. Gehr, W. L. Seitz, S. A. Sheffield, R. R. Alcon, D. L. Robbins, and B. A. Barker. Shock initiation of the TATB-based explosive PBX 9502 cooled to -55 C. In *Thirteenth (International) Symposium on Detonation*, pages 970–979, 2005.

R. L. Gustavsen, S. A. Sheffield, and R. R. Alcon. Measurements of shock initiation in the tri-amino-tri-nitro-benzene based explosive PBX 9502: Wave forms from embedded gauges and comparison of four different material lots. *J. Appl. Phys.*, 99:114907, 2006. URL `http://dx.doi.org/10.1063/1.2195191`.

R. L. Gustavsen, B. D. Bartram, and N. J. Sanchez. Detonation wave profiles measured in plastic bonded explosives using 1550 nm photon doppler velocimetry. In *AIP Conference Proceedings*, volume 1195, pages 253–256, 2009. URL `https://doi.org/10.1063/1.3295117`.

R. L. Gustavsen, R. J. Gehr, S. M. Bucholtz, R. R. Alcon, and B. D. Bartram. Shock initiation of triaminotrinitrobenzene base explosive PBX 9502 cooled to -55 C. *J. Appl. Phys.*, 112, 2012. URL `https://doi.org/10.1063/1.4757599`.

R. L. Gustavsen, T. D. Aslam, B. D. Bartram, and B. C. Hollowell. Plate impact experiments on the TATB based explosive PBX 9502 at pressures near the Chapman-Jouguet state. *Journal of Physics: Conference Series 500*, art. 052015, 2014. URL `http://dx.doi.org/10.1088/1742-6596/500/5/052015`.

R. L. Gustavsen, D. M. Dattelbaum, E. B. Watkins, M. A. Firestone, D. W. Podlesak, B. J. Jensen, B. S. Ringstrand, R. C. Huber, J. T. Mang, C. E. Johnson, K. A. Velizhanin, T. M. Willey, D. W. Hansen, C. M. May, R. L. Hodgin, M. Bagge-Hansen, A. W. van Buuren, L. M. Lauderbach, A. C. Jones, T. J. Graber, N. Sinclair, S. Seifert, and T. Gog. Time resolved small angle x-ray scattering experiments performed on detonating explosives at the advanced photon source: Calculation of the time and distance between the detonation front and the x-ray beam. *J. Appl. Phys.*, 121, 105902, 2017a. URL `http://dx.doi.org/10.1063/5.0077906`.

R. L. Gustavsen, R. J. Gehr, S. M. Bucholtz, A. H. Pacheco, and B. D. Bartram. Shock initiation of the TATB-based explosive PBX 9502 heated to 76 C. In *AIP Conference Proceedings 1793, 030017*, 2017b. URL `https://doi.org/10.1063/1.4971475`.

R. L. Gustavsen, T. D. Aslam, and B. D. Bartram. Multi-shock experiments on the TATB based explosive PBX 9502 and the HMX based explosive PBX 9501. In *Sixteenth (International) Symposium on Detonation*, 2018a. LA-UR-18-25564.

R. L. Gustavsen, B. D. Bartram, L. L. Gibson, A. H. Pacheco, J. D. Jones, and A. B. Goodbody. Shock initiation of the TATB-based explosive PBX 9502 heated to 130 C. In *AIP Conference Proceedings 1979, 100015*, 2018b. URL `https://doi.org/10.1063/1.5044887`.

C. A. Handley, P. J. Rae, M. S. Jakulewicz, and R. Menikoff. Experiments and modelling of detonation extinction. Technical Report LA-UR-19-23607, Los Alamos National Lab., 2019. URL `http://permalink.lanl.gov/object/tr?what=info:lanl-repo/lareport/LA-UR-19-23607`. Europyro 2019 conference.

A. J. Heim, N. Grønbech-Jensen, E. M. Kober, and T. C. Germann. Molecular dynamics simulations of detonation instability. *Phys Rev E Stat Nonlin Soft Matter Phys*, 78:046710, 2008. URL `https://doi.org/10.1103/PhysRevE.78.046710`.

L. F. Henderson and R. Menikoff. Triple-shock entropy theorem and its consequences. *J. Fluid Mech.*, 366:179–210, 1998. URL `https://doi.org/10.1017/S0022112098001244`.

B. F. Henson, B. W. Asay, L. B. Smilowitz, and P. M. Dickson. Ignition chemistry in HMX from thermal explosion to detonation. In *Shock Compression of Condensed Matter – 2001*, pages 1069–1072, 2002. URL `https://doi.org/10.1063/1.1483723`.

L. G. Hill. Development of the LANL sandwich test. In *AIP Conference Proceedings*, volume 620, pages 149–152, 2001. URL `https://doi.org/10.1063/1.1483503`.

L. G. Hill and T. D. Aslam. Detonation shock dynamics calibration for PBX 9502 with temperature, density and material lot variations. In *Proceeding of the Fourteenth International Symposium on Detonation*, pages 779–788, 2010.

L. G. Hill, J. B. Bdzil, and T. D. Aslam. Front curvature rate stick measurements and detonation shock dynamics calibration for PBX 9502 over a wide temperature range. In *Proceeding of the Eleventh International Symposium on Detonation*, pages 1029–1037, 1998.

R. S. Hixson, M. S. Shaw, J. N. Fritz, J. N. Vorthman, and W. W. Anderson. Release isentropes of overdriven plastic-bonded explosive PBX 9501. *J. Appl. Phys.*, 88:6287–6293, 2000. URL `https://doi.org/10.1063/1.1323513`.

B. C. Hollowell, R. L. Gustavsen, and D. M. Dattelbaum. Shock initiation of TATB-based explosive PBX 9502 cooled to 77 Kelvin. *J. Phys. Conf. Series*, 500, 2014. URL `https://doi.org/10.1088/1742-6596/500/18/182014`.

A. K. Kapila, R. Menikoff, J. B. Bdzil, S. F. Son, and D. S. Stewart. Two-phase modeling of deflagration-to-detonation transition in granular materials: Reduced equations. *Physics of Fluids*, 13:3002–3024, 2001. URL `https://doi.org/10.1063/1.1398042`.

M. P. Kroonblawd, P. Lafourcade, L. E. Fried, J-B. Maillet, and T. Sewell. New nonreactive force field for accurate molecular dynamics simulations of TATB at extreme conditions. *Journal of Chemical & Engineering Data*, 69:1526–1545, 2024. URL `https://doi.org/10.1021/acs.jced.3c0`.

J. W. Kury, E. L. Lee, H. C. Hornig, J. L. McDonnel, D. L. Ornellas, M. Finger, F. M. Strange, and M. L. Wilkins. Metal acceleration by chemical explosives. In *Forth Symposium (International) on Detonation*, pages 3–13, 1965.

E. L. Lee and C. M. Tarver. Phenomenological model of shock initiation in heterogeneous explosives. *Phys. Fluids*, 23:2362–272, 1980. URL `https://doi.org/10.1063/1.862940`.

E. L. Lee, H. C. Hornig, and J. W. Kury. Adiabatic Expansion Of High Explosive Detonation Products. Technical Report UCRL-50422, Lawrence Livermore National Lab., 1968. URL `https://doi.org/10.2172/4783904`.

K. T. Lorenz, E. L. Lee, and R. Chambers. A simple and rapid evaluation of explosive performance – the disc acceleration experiment. *Propellants Explosives Pyrotechnics*, 40: 95–108, 2015. URL `http://dx.doi.org/10.1002/prep.201400081`.

C. L. Mader, editor. *LASL Phermex Data*, volume III. Univ. of Calif. Press, 1979.

J. T. Mang, R. P. Hjelm, and E. G. Francois. Measurement of porosity in a composite high explosive as a function of pressing conditions by ultra-small-angle neutron scattering with contrast variations. *Propellants, Explosives, Pyrotechnics*, 35:7–14, 2010. URL `https://doi.org/10.1002/prep.200900026`.

S. P. Marsh, editor. *LASL Shock Hugoniot Data*. Univ. of Calif. Press, 1980.

R. R. McGuire and C. M. Tarver. Chemical decomposition model for the thermal explosion of confined HMX, RDX and TNT explosives. In *Proceeding of the Seventh International Symposium on Detonation*, pages 56–64, 1981.

R. Menikoff. Complete EOS for PBX 9502. Technical Report LA-UR-09-06529, Los Alamos National Lab., 2009. URL `http://www.osti.gov/scitech/servlets/purl/1043481/`.

R. Menikoff. Deflagration wave profiles. Technical Report LA-UR-12-20353, Los Alamos National Lab., 2012. `http://dx.doi.org/10.2172/1038128`.

R. Menikoff. Effect of resolution on a propagating detonation wave. Technical Report LA-UR-14-25140, Los Alamos National Laboratory, 2014a. URL `http://dx.doi.org/10.2172/1136940`.

R. Menikoff. Molecular solid EOS based on quasi-harmonic oscillator approximation for photons. Technical Report LA-UR-14-26858, Los Alamos National Lab., 2014b. URL `https://doi.org/10.2172/1159050`.

R. Menikoff. Complete Mie-Grüneisen Equation of State. Technical Report LA-UR-16-21706, Los Alamos National Lab., 2016. URL `https://doi.org/10.2172/1241653`.

R. Menikoff. Failure diameter of PBX 9502: Simulations with the SURFplus model. Technical Report LA-UR-17-25300, Los Alamos National Lab., 2017a. URL `https://www.osti.gov/scitech/servlets/purl/1369155`.

R. Menikoff. SURFplus model calibration for PBX 9502. Technical Report LA-UR-17-31015, Los Alamos National Lab., 2017b. URL `https://doi.org/10.2172/1412839`.

R. Menikoff. SURF model calibration for PBX 9501. Unpublished writeup, August 2018a.

R. Menikoff. Review of PBX 9502 Pop plot data. Technical Report LA-UR-18-31380, Los Alamos National Lab., 2018b. URL `https://doi.org/10.2172/1485358`.

R. Menikoff. Approach of a planar detonation to a steady CJ detonation wave. Technical Report LA-UR-19-28220-rev1, Los Alamos National Lab., 2019a. URL `https://doi.org/10.2172/1558021`.

R. Menikoff. SURF model resolution in xRage code. Technical Report LA-UR-19-31881, Los Alamos National Lab., 2019b. URL `https://doi.org/10.2172/1575763`.

R. Menikoff. Effect of heterogeneities on the reaction-zone profile of a propagating detonation wave. Technical Report LA-UR-20-24842, Los Alamos National Lab., 2020. URL `https://doi.org/10.2172/1643894`.

R. Menikoff. Re-calibration of PBX 9501 SURF model. Technical Report LA-UR-21-27882, Los Alamos National Lab., 2021a. URL `https://doi.org/10.2172/1812634`.

R. Menikoff. xRage simulations of magnetic velocity gauges used in gas gun shock initiation experiments. Technical Report LA-UR-21-21769, Los Alamos National Lab., 2021b. URL `https://doi.org/10.2172/1766987`.

R. Menikoff. Detonation wave profile. Technical Report LA-UR-22-29247, Los Alamos National Lab., 2022a. URL `https://doi.org/10.2172/1885738`.

R. Menikoff. Reactive flow characteristics. Technical Report LA-UR-22-32479, Los Alamos National Lab., 2022b. URL `https://www.osti.gov/servlets/purl/1902075`.

R. Menikoff and E. M. Kober. Compaction waves in granular HMX. Technical Report LA-13546-MS, Los Alamos National Lab., 1999.

R. Menikoff and E. M. Kober. Compaction waves in granular HMX. In *AIP conference proceedings*, volume 505, pages 397–400. American Institute of Physics, 2000a.

R. Menikoff and E. M. Kober. Equation of state and Hugoniot locus for porous materials: P–α model revisited. In *AIP conference proceedings*, volume 505, pages 129–132. American Institute of Physics, 2000b.

R. Menikoff and B. Plohr. Riemann problem for fluid flow of real materials. *Revs. Mod. Phys.*, 61:75–130, 1989. URL `https://doi.org/10.1103/RevModPhys.61.75`.

R. Menikoff and M. S. Shaw. The SURF model and the curvature effect for PBX 9502. *Combustion Theory and Modelling*, 16:1140–1169, 2012. URL `http://dx.doi.org/10.1080/13647830.2012.713994`.

R. Menikoff, C. A. Scovel, and M. S. Shaw. Cylinder test wall velocity: Experimental and simulated data. Technical Report LA-UR-13-23630, Los Alamos National Lab., 2013. URL `http://www.osti.gov/scitech/servlets/purl/1079963/`.

A. Nassar, N. K. Rai, O. Sen, and H. S. Udaykumar. Modeling mesoscale energy localization in shocked HMX, Part I: machine-learned surrogate models for the effects of loading and void sizes. *Shock Waves*, 29:537–558, 2019. URL `https://doi.org/10.1007/s00193-018-0874-5`.

Y. T. Nguyen, C. Okafor, P. Zhao, O. Sen, . R. Picu, T. Sewell, and H. S. Udaykumar. Continuum models for meso-scale simulations of HMX (1,3,5,7-tetranitro-1,3,5,7-tetrazocane) guided by molecular dynamics: Pore collapse, shear bands, and hotspot temperature. *J. Appl. Phys.*, 136:114902, 2024. URL `https://doi.org/10.1063/5.0232413`.

B. Olinger. Compacting plastic-bonded explosive molding powders to dense solids. Technical Report LA-14173, Los Alamos National Lab., 2005. URL `https://doi.org/10.2172/883457`.

B. M. Patterson, L. Kuettner, K. Henderson, J. D. Yeager, and L. Hill. The wormholes within: A study of 1, 3, 5-triamino-2, 4, 6-trinitrobenzene crystal morphology by micro and nano-scale x-ray computed tomography and its effects upon the shock sensitivity of detonation. *Propellants, Explosives, Pyrotechnics*, 47:e202100340, 2022. URL `http://doi.org/10.1002/prep.202100340`.

H. Pei, W. Huang, X. Zhang, and X. Zheng. Measuring detonation wave profiles in plastic-bonded explosives using PDV. *AIP Advances*, 9:015306, 2019. URL `https://doi.org/10.1063/1.5057879`.

S. Pemberton, T. Sandoval, T. Herrera, and J. Echave. Test report for equation of state measurements of PBX 9502. Technical Report LA-UR-11-04998, Los Alamos National Lab., 2011a.

S. Pemberton, T. Sandoval, T. Herrera, J. Echave, and G. Maskaly. Test report for equation of state measurements of PBX 9501. Technical Report LA-UR-11-04999, Los Alamos National Lab., 2011b.

J. B. Ramsay and A. Popolato. Analysis of shock wave and initiation data for solid explosives. In *Fourth Symposium (International) on Detonation*, pages 233–538, 1965.

R. B. Schwarz, G. W. Brown, D. G. Thompson, W. Olinger B, J. Furmanski, and H. H. Cady. The effect of shear strain on texture in pressed plastic bonded explosives. *Propellants Explosives Pyrotechnics*, 380:685–694, 2013. URL `http://dx.doi.org/10.1002/prep.201200204`.

W. L. Seitz, H. L. Stacy, R. Engelke, P. K. Tang, and J. Wackerle. Detonation reaction-zone structure of PBX 9502. In *Proceeding of the Ninth International Symposium on Detonation*, pages 164–669, 1989.

M. S. Shaw and J. D. Johnson. Carbon clustering in detonations. *J. Appl. Phys.*, 62:2080–2085, 1987.

S. A. Sheffield, R. Engelke, and R. R. Alcon. In-situ study of the chemically driven flow fields in initiating homogeneous and heterogeneous nitromethane explosions. In *Proceeding of the Ninth International Symposium on Detonation*, pages 39–49, 1989.

S. A. Sheffield, R. L. Gustavsen, R. R. Alcon, D. L. Robbins, and D. B. Stahl. High pressure Hugoniot and reaction rate measurements in PBX 9501. In *AIP conference proceedings*, volume 706, pages 1033–1036, 2004. URL `https://doi.org/10.1063/1.1780414`.

Mark Short and James J. Quirk. High explosive detonation–confiner interactions. *Annual Rev. Fluid Mech.*, 50:215–242, 2018. URL `https://doi.org/10.1146/annurev-fluid-122316-045011`.

C. B. Skidmore, D. S. Phillips, P. M. Howe, J. T. Mang, and J. A. Romero. The evolution of microstructural changes in pressed HMX explosives. In *Eleventh (International) Symposium on Detonation*, pages 556–564, 1998.

C. B. Skidmore, T. A. Butler, and C. W. Sandoval. The elusive coefficient of thermal expansion in PBX 9502. Technical Report LA-14003, Los Alamos National Lab., 2003. URL `https://www.osti.gov/scitech/servlets/purl/809945`.

Arnaud Sollier, Philippe Hébert, and Roland Letremy. Chemical reaction zone measurements in pressed trinitrotoluene (TNT) and comparison with triaminotrinitrobenzene (TATB). *J. Appl. Phys.*, 131:055902, 2022. URL `https://doi.org/10.1063/5.0077906`.

J. Starkenberg. Modeling detonation propagation and failure using explosive initiation models in a conventional hydrocode. In *Twelfth Symposium (International) on Detonation*, pages 1001–1007, 2002.

D. S. Stewart and J. Yao. The normal detonation shock velocity–curvature relationship for materials with nonideal equation of state and multiple turning points. *Combustion and Flame*, 113:224–235, 1998. URL `https://doi.org/10.1016/S0010-2180(97)00170-3`.

D. S. Stewart, S. Yoo, and W. C. Davis. Equation of state for modeling the detonation reaction zone. In *Proceeding of the Twelfth International Symposium on Detonation*, pages 624–631, 1989.

O. T. Strand, D. R. Goosman, C. Martinez, and T. L. Whitworth. Compact system for high-speed velocimetry using heterodyne techniques. *Rev. Sci. Instrum.*, 77:083108, 2006. URL `https://https://doi.org/10.1063/1.2336749`.

P. K. Tang, W. W. Anderson, J. N. Fritz, R. S. Hixson, and J. E. Vorthman. A study of the overdriven behaviors of PBX 9501 and PBX 9502. In *Eleventh Symposium (International) on Detonation*, pages 1058–1064, 1998.

C. M. Tarver, S. K. Chidester, and A. L. Nichols. Critical conditions for impact- and shock-induced hot spots in solid explosives. *J. Phys. Chem.*, 100:5794–5799, 1996. URL `https://doi.org/10.1021/jp953123s`.

D. G. Thompson, G. W. Brown, B. Olinger, J. T. Mang, B. Patterson, R. DeLuca, and S. Hagelberg. The effects of TATB ratchet growth on PBX 9502. *Propellants Explosives Pyrotechnics*, 35:507–513, 2010. URL `http://doi.org/10.1002/prep.200900067`.

C. Ticknor, S. A. Andrews, and J. A. Leiding. Magpie: A new thermochemical code. *AIP Conference Proceedings*, 2272:030033, 2020. URL `https://doi.org/10.1063/12.0000785`.

K. S. Vandersall, C. M. Tarver, F. Garcia, and S. K. Chidester. On the low pressure shock initiation of octahydro-1,3,5,7-tetranito-1,3,5,7-tetrazocine based plastic bonded explosives. *J. Appl. Phys.*, 107:094906, 2010. URL `https://doi.org/10.1063/1.3407570`.

B. L. Wescott. Generalized pseudo-reaction zone model for non-ideal explosives. In *Shock Compression of Condensed Matter – 2007*, pages 433–436, 2007. URL `https://doi.org/10.1063/1.2833086`.

B. L. Wescott, D. S. Stewart, and W. C. Davis. Equation of state and reaction rate for condensed-phase explosives. *Journal of Applied Physics*, 98:053514, 2005. URL `https://doi.org/10.1063/1.2035310`.

G. B. Whitham. *Linear and Nonlinear Waves.* John Wiley & Sons, 1974.

M. L. Wilkins. The use of one-and two-dimensional hydrodynamic machine calculations in high explosive research. In *Fourth Symposium (International) on Detonation*, 1965.

J. Yao and D. S. Stewart. On the dynamics of multi-dimensional detonation. *Journal of Fluid Mechanics*, 309:225–275, 1996. URL `https://doi.org/10.1017/S0022112096001620`.

J. D. Yeager, L. A. Kuettnerand, A. L. Duque, L. G. Hill, and B. M. Patterson. Microcomputed x-ray tomographic imaging and image processing for microstructural characterization of explosives. *Materials*, 13:4517, 2020. URL `http://doi.org/10.3390/ma13204517`.

C.-S. Yoo and H. Cynn. Equation of state, phase transition, decomposition of β-HMX. *J. Chem. Phys.*, 111:10229–10235, 1999. URL `https://doi.org/10.1063/1.480341`.

J. M. Zaug, C. E. Young, G. T. Long, J. L. Maienschein, E. A. Glascoe, D. W. Hansen, J. F. Wardell, C. K. Black, and G. B. Sykora. Deflagration rates of secondary explosives under static MPa–GPa pressure. *AIP Conference Proceedings*, 1195:420–423, 2009. URL `https://doi.org/10.1063/1.3295162`.

Index

List of Figures